

University of Alabama
Bureau of Engineering Research
University, Alabama

STUDY OF THE STABILITY OF THE S-IC OPEN-LOOP
PROPELLANT-HYDRAULIC SYSTEM

Final Report
Contract NAS8-11341
July 26, 1964 - July 26, 1966

By

Dennis N. Osteen
Professor of Electrical Engineering
Project Director

and

William C. Stapleton, Jr.
Professor of Electrical Engineering
Research Associate

and

Erwin A. Reinhard
Assistant Professor of Electrical Engineering
Research Associate

FACILITY FORM 602

N66 37576

(ACCESSION NUMBER)

84

(THRU)

1

(PAGES)

Gir-78391

(CODE)

63

(CATEGORY)

August, 1966

Prepared for
George C. Marshall Space Flight Center
Huntsville, Alabama

GPO PRICE \$
CFSTI PRICE(S) \$

Hard copy (HC) 3.00

Microfiche (MF) .25

#653 July 66

TABLE OF CONTENTS

INTRODUCTION	1
FLEXIBLE COUPLINGS	2
ANALOG COMPUTER SIMULATION	8
ANALOG COMPUTER STUDY OF THE SC-I OPEN-LOOP PROPELLANT-HYDRAULIC SYSTEM	26
HIGH PRESSURE SURGE GENERATION	65
APPENDIX A	73
REFERENCES	80

LIST OF TABLES

Table 3.1 - Pressure Drop-Flow Rate Data for Lines . .	10
Table 3.2 - Filter Manifold Characteristics	10
Table 3.3 - Definition of Symbols Used in Simulation ..	14
Table 4.1 - System Response to Step Inputs	30

LIST OF FIGURES

Figure 2-1. Detailed Drawing of Bellows Configuration	5
Figure 2-2. a) Straight Wall Bellows b) Correction Factor For Certain Parameter Ratios c) Equation For Spring Constant d) Nomenclature And Nominal Values For Parameters Of System Bellows	6
Figure 3-1. Diagram for Squaring and Square Root Circuits . . .	11
Figure 3-2. Pressure Drop-Flow Rate Characteristic of Filter Manifold	12
Figure 3-3. Block Diagram of System	16
Figure 3-4. Simulation of Lines and Filter Manifold	17
Figure 3-5. Actuator Assembly	18
Figure 3-6. Simulation of Fluid Flow in Main Metering Valve . .	20
Figure 3-7. Simulation of Actuator Fluid Equations	21
Figure 3-8. Simulation of Actuator and Engine Position	23
Figure 3-9. Representation of Gimbal Friction	24
Figure 3-10. Simulation of Pressure Feedback Network	25
Figure 3-11. Simulation of Actuator Metering Spool Position Time Scaled 100 to 1	27
Figure 4-1. System Indices for Step Function Input Command Signal	28
Figure 4-2. System Response to Step Command of 0.5 Degree . . .	31
Figure 4-3. System Response to Step Command of 0.75 Degree . .	32
Figure 4-4. System Response to Step Command of 1.0 Degree . . .	33
Figure 4-5. System Response to Step Command of 1.25 Degrees. .	34
Figure 4-6. System Response to Step Command of 1.5 Degrees . .	35
Figure 4-7. System Response to Step Command of 1.75 Degrees . .	36
Figure 4-8. System Response to Step Command of 2.0 Degrees . .	37
Figure 4-9. System Response to Step Command of 2.25 Degrees . .	38
Figure 4-10. System Response to Step Command of 2.5 Degrees . .	39

Figure 4-11. System Response to Step Command of 2.75 Degrees . . .	40
Figure 4-12. System Response to Step Command of 3.00 Degrees . . .	41
Figure 4-13. System Dynamic Behavior to Step Command of 0.50 Degrees	42
Figure 4-14. System Dynamic Behavior to Step Command of 0.75 Degrees	43
Figure 4-15. System Dynamic Behavior to Step Command of 1.0 Degree	44
Figure 4-16. System Dynamic Behavior to Step Command of 1.25 Degrees	45
Figure 4-17. System Dynamic Behavior to Step Command of 1.5 Degrees	46
Figure 4-18. System Dynamic Behavior to Step Command of 1.75 Degrees	47
Figure 4-19. System Dynamic Behavior to Step Command of 2.0 Degrees	48
Figure 4-20. System Dynamic Behavior to Step Command of 2.25 Degrees	49
Figure 4-21. System Dynamic Behavior to Step Command of 2.5 Degrees	50
Figure 4-22. System Dynamic Behavior to Step Command of 2.75 Degrees	51
Figure 4-23. System Dynamic Behavior to Step Command of 3 Degrees	53
Figure 4-24. Strip Chart Recordings for Sinusoidal Input Command Signals	54
Figure 4-25. Sinusoidal Gain Characteristic - Input Command of 0.5 Degree Peak to Peak	55
Figure 4-26. Sinusoidal Phase Characteristic - Input Command 0.5 Degree Peak to Peak	56
Figure 4-27. Sinusoidal Gain Characteristic - Input Command 0.6 Degree Peak to Peak	57
Figure 4-28. Sinusoidal Phase Characteristic - Input Command 0.6 Degree Peak to Peak	58
Figure 4-29. Sinusoidal Gain Characteristic - Input Command 0.75 Degree Peak to Peak	59

Figure 4-30. Sinusoidal Phase Characteristic - Input Command 0.75 Degree Peak to Peak	60
Figure 4-31. Sinusoidal Gain Characteristic - Input Command 0.80 Degree Peak to Peak	61
Figure 4-32. Sinusoidal Phase Characteristic - Input Command 0.80 Degree Peak to Peak	62
Figure 4-33. Sinusoidal Gain Characteristic - Input Command 1.0 Degree Peak to Peak	63
Figure 4-34. Sinusoidal Phase Characteristic - Input Command 1.0 Degree Peak to Peak	64
Figure 5-1. Location of Equivalent Point Mass of the Engine with Respect to Three Cartesian Coordinate Systems . . .	66
Figure 5-2. Path Described by Equivalent Point Mass of Engine in x', y', z' Coordinate System	68
Figure 5-3. Path Described by Equivalent Point Mass in x', y', z' Coordinate System	68
Figure 5-4. Projected Path in x', y' Plane	69
Figure 5-5. Figure Used to Determine the Constant of Proportional k	70
Figure 6-1. Detail of Flapper Valve	74
Figure 6-2. Simulation of Nozzle Flow	78
Figure 6-3. Simulation of Metering Spool Position	79

University of Alabama
Bureau of Engineering Research
University, Alabama

STUDY OF THE STABILITY OF THE S-IC OPEN-LOOP
PROPELLANT-HYDRAULIC SYSTEM

By

Dennis N. Osteen
Professor of Electrical Engineering

and

William C. Stapleton Jr.
Professor of Electrical Engineering

and

Erwin A. Reinhard
Assistant Professor of Electrical Engineering

INTRODUCTION

This report is a summary of a study performed by the Bureau of Engineering Research, University of Alabama, under Contract NAS8-11341 with the George C. Marshall Space Flight Center. The project consisted of the investigation of the stability and performance of the S-CI open-loop propellant-hydraulic system.

This study can be broken down into four basic parts. The first part consisted of an investigation or study of the behavior of the flexible hose or coupling sections of the fluid lines. The second part undertaken was to derive a meaningful analog simulation for the system under study. A third part consisted of a stability and performance study utilizing the analog model. A fourth part consisted of a study to try to determine the cause of certain high pressure surges observed by NASA personnel. These surges occurred in one channel when certain command signals were applied to the other channels.

FLEXIBLE COUPLINGS

The study of the performance of the flexible couplings of the system was undertaken first because of the urgency felt due to certain failures experienced during static and life-cycling tests which were being performed by NASA personnel. This particular study was conducted in order to determine what theoretical and experimental work had been done that might prove to give some knowledge which would be fruitful to the solution of this problem.

The first meaningful information concerning bellows-like fluid lines seems to emanate from experimental work conducted in order to correlate pressure drop information in order to obtain a friction factor for use in the Darcy-Weirsbach Equation for frictional pressure loss at high flow rates.^{*1} This work was later extended to cover a greater variety of the convolution configurations.² Most of this work was confined to pressure drop information.

Bellows are corrugated cylinders which have a wall thickness that is relatively thin compared to the wall thickness of the duct in which it is used. This definition is given by C. M. Daniels in an article "Designing for Duct Flexibility with Bellows Joints".³ In this article Mr. Daniels makes several general observations on the use of bellows as well as on their capabilities and limitations. He classifies them according to their modes of flexibility such that the two types used in this system are known as External Gimbal type and the Braided Wire Restraint type. He cites buckling and fatigue as common causes of bellows failure with fatigue being the most prevalent cause. As a general rule, the line length of a relatively flexible, unsupported bellows should be less than the diameter of the ducting in order to prevent buckling. For

^{*} References are tabulated at the end of this report.

a relatively stiff bellows, the length may be longer than the diameter if the increased spring rate does not adversely affect the system performance. Mr. Daniels also states that longer lengths are practical for bellows with wire braid. The internal pressure at which a bellows becomes unstable and buckles is the critical buckling pressure. He points out the likelihood of failure due to vibrations caused by high-velocity compressible fluids. Another very important point he makes is that over stressing the bellows can impair the life of the bellows. This point will be discussed in more detail later in this report. Mr. Daniels presents fatigue data which indicates that the life of a bellows joint is directly proportional to fatal stress regardless of the configuration.

Several different analytical models for bellows have been reported in the literature.^{4,5,6} Techniques of production and fabrications have also been reported on in the literature.^{4,7,8} James D. Matheney in an article entitled "Bellows Spring Rate for Seven Typical Convolution Shapes"⁹ has attempted to combine these several theories into a single criterion for calculating the critical buckling pressure. The spring rate is strongly dependent on the bellows configuration and expressions are developed for the various configurations with the equations being stated to an accuracy to within 5 percent. On some commercial bellows samples that were evaluated in the laboratory, it was found that the material might vary in thickness from root to crest by 25 percent so that the accuracy of the equation was tolerable under such conditions. In private conversations with Dr. Matheney, he emphasized the excellent comparison between observed and calculated critical pressures in view of the widely different manufacturing processes that are employed in bellows construction. The bellows in this system are of the type shown

in Fig. 2-1. This is the straight wall type where the radius of the convolution wave form is equal to the quarter-pitch length. The pictorial description and nomenclature associated with such a bellows type is shown in Fig. 2-2. The spring constant is given by

$$R = 0.575 \frac{ah^3 Eq}{g^3 c} \frac{1}{k} \quad (2-1)$$

using the nominal values of the parameters for the system bellows as tabulated in Fig. 1-2, the above equation gives

$$R = \frac{5140}{c} \text{ lb/in} \quad (2-2)$$

where c is the active length of the bellows in inches. The equation is very sensitive to the thickness of the bellows wall since it appears to the third power. The critical pressure for an unguided but restrained single bellows is then given by

$$P_{cr} = \frac{2\pi R}{c} = \frac{2\pi \cdot 5140}{c^2} \text{ psi.} \quad (2-3)$$

For the system under study, the nominal high pressure in the fluid duct is given as 200 psig while the nominal pressure in the return duct is as 500 psig. Substituting Eq. (1-2) into Eq. (1-3) and solving for c gives

$$c = \frac{2\pi \cdot 5140}{P_{cr}}^{1/2} \text{ in.} \quad (2-4)$$

from which

$$c_{max} = 3.8 \text{ in. for the 2200 psig}$$

pressure and

$$c_{max} = 8.0 \text{ in. for the 500 psig pressure.}$$

The bellows in the flight supply duct given by specification number 60 B 83002-5 and the gimbal duct assemblies given by specification numbers 60 B 83002-1 and 60 B 8300-3 have an active bellows length of 1.25

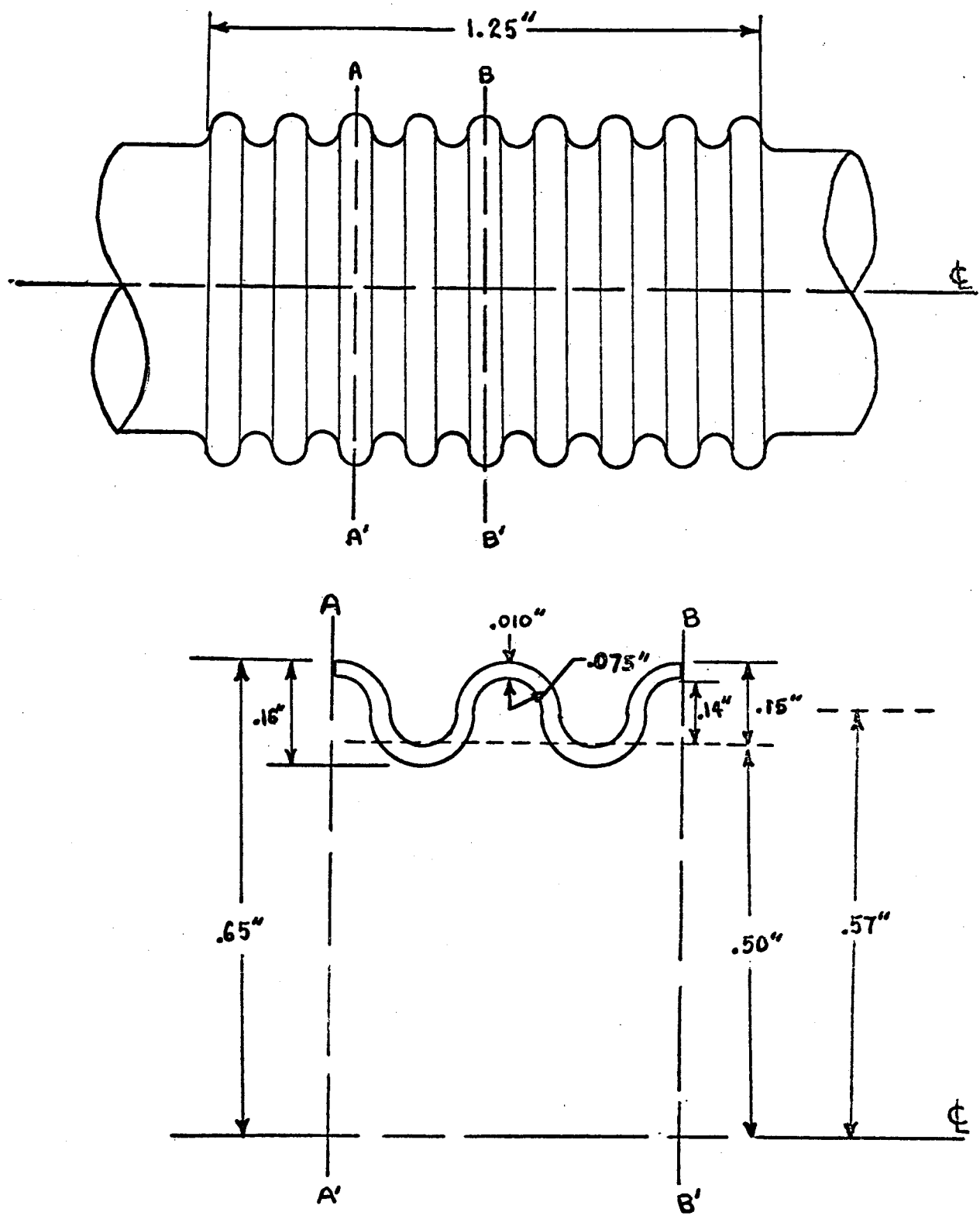
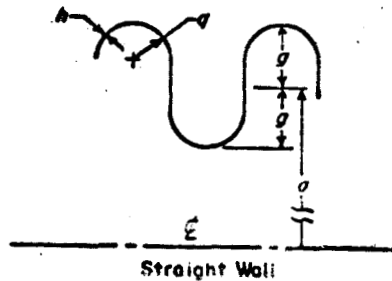
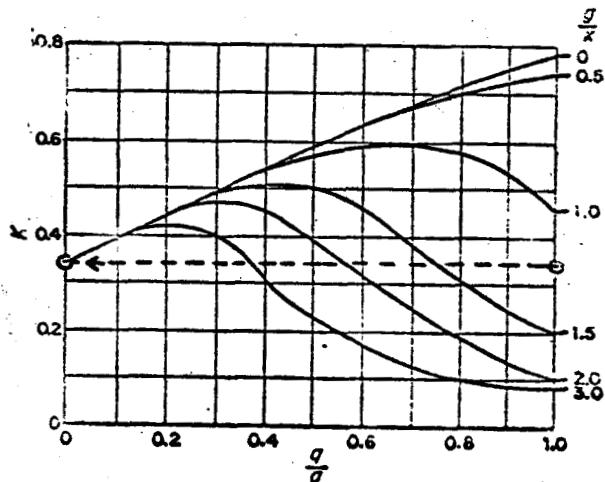


Fig. 2-1. Detailed Drawing of Bellows Configuration



(a)



(b)

$$R = 0.575 \frac{ah^3 E q}{g^3 c} \frac{1}{K}$$

(c)

NomenclatureSystem Bellows Parameter Values

a = Mean radius of bellows or toroid, in.	0.57 in.
b = Radius of convolution wave form, in.	0.075 in.
c = Active length of bellows, in.	
g = Height of convolution above mean radius, a , in.	0.075 in.
h = Thickness of bellows wall, in.	0.010 in.
q = Quarter-pitch length, in.	0.075 in.
x = Size factor = $(ah)^{1/2} / 1.286$	0.059
K = Correction factor	0.34
E = Modulus of elasticity, psi	30×10^6 psi
R = Spring rate, lb/in.	$\frac{5140}{c}$ lb/in.

(d)

Fig. 2-2. a) Straight Wall Bellows b) Correction Factor For Certain Parameter Ratios c) Equation For Spring Constant d) Nomenclature And Nominal Values For Parameters Of System Bellows.

inches with an overall length of 2.85 inches between the welded joints. It is not certain how the straight cylindrical end sections affect the critical pressure but it should be conservative in comparison to an overall bellows length of 2.85 inches. Thus buckling or squirming would not be a likely cause for failure in these high pressure bellows. Those flexible hoses or bellows indicated in the ground supply duct assembly on the S-IC Hydraulic System Schematic seem to be considerably longer than those indicated in the high pressure lines. The maximum length based on the nominal ground supply pressure should serve as a basis for checking the actual lengths of the flexible sections.

The flexible hose indicated in the return duct assemblies given by specification number 60 B 83004-1 are indicated as being from 6 to 8 inches and from 7 to 12 inches in length. A detailed drawing of the geometrical configuration is not in the investigators possession but assuming the same basic configuration as in the high pressure lines, it is obvious that nominal pressure may be very close to and may even exceed the critical pressure.

The three high pressure ducts according to specification number and 60 B 8002 are to withstand a proof pressure test of 4400 psig without leakage, damage or permanent deformation according to paragraph 3.3.6. Each unit is to be subjected to this test according to paragraph 4.3.1 of the same specification. Based on the 4400 psig proof pressure, the maximum active length for the bellows in the high pressure lines becomes 2.7 inches which is still greater by a factor of two than the actual bellows length but about equal to the length between the welded ends. The specification does not make clear how permanent deformation is to be determined.

High static pressure test of bellows sections tend to squeeze or compress the root of the bellows and at the same time tend to expand or balloon the crest of the bellows. Excessive test pressures can cause structural damage by these processes which could lead to later failure such as those which have occurred during the life-cycling test. How permanent deformation is to be determined following the high pressure test is not made clear by the 60 B 83002 specification. Based on this analysis and a liberal amount of judgement, the investigators submit the following recommendations:

1. The maximum lengths of all flexible hoses or bellows be evaluated in terms of the critical pressure leading to buckling or squirming and
2. The proof pressure test be re-examined with the goal of reducing this pressure to a pressure 10 to 20% percent above nominal operating pressure.

The latter recommendation could be easily evaluated with an experimental test program coupled with a statistical analysis.

ANALOG COMPUTER SIMULATION

The analog computer simulation for the S-IC open-loop propellant-hydraulic system as first derived for use in this study was first presented in the Summary Report of June, 1965.¹⁰ Subsequent modifications which were found necessary were presented in Quarterly Report No. 5.¹¹ The final corrected simulation which was used in this study is presented here.

It became apparent early in the study that a completely theoretical approach to the simulation of the fluid ducts would not be satisfactory for this study. The large number of bends and flexible couplings in the lines would cause such an approach to yield a simulation for more

complication than existing analog equipment would permit. Since the flows in the lines appeared to be turbulent, the flow rate was assumed to be proportional to the square root of the pressure drop. The constant of proportionality or flow coefficient was determined from experimental data which, in general, consisted of one point per line section. The experimental data and derived flow coefficients are given in Table 3-1. Since there was no data furnished for the line section connecting the checkout valve to the low pressure fuel duct, it was assumed that this line would be identical with the line connecting the high pressure fuel duct to the filter manifold.

The use of the squarelaw relationship for the pressure drop-flow rate characteristics required the use of more nonlinear equipment such as multipliers and function generators than was available at the University of Alabama Analog Laboratory. Consequently, a circuit was designed and constructed for use with an operational amplifier which would perform either a squaring or a square root function. This circuit, with the appropriate connection diagram is shown in Fig. 3-1. The error given by this circuit was found to be less than two percent over the operating range. It is believed that improvements in the accuracy could be made if necessary.

Sufficient data was available for the filter manifold to indicate that the pressure drop was not proportional to the square of the flow rate. This data is given in Table 3-2. The pressure drop-flow characteristic is shown in Fig. 3-2. A diode function generator was used in the simulation to provide the desired characteristic and the corresponding voltages used in setting up the function generator as given in Table 3-2. Biasing of the characteristic curve was used to study the effects

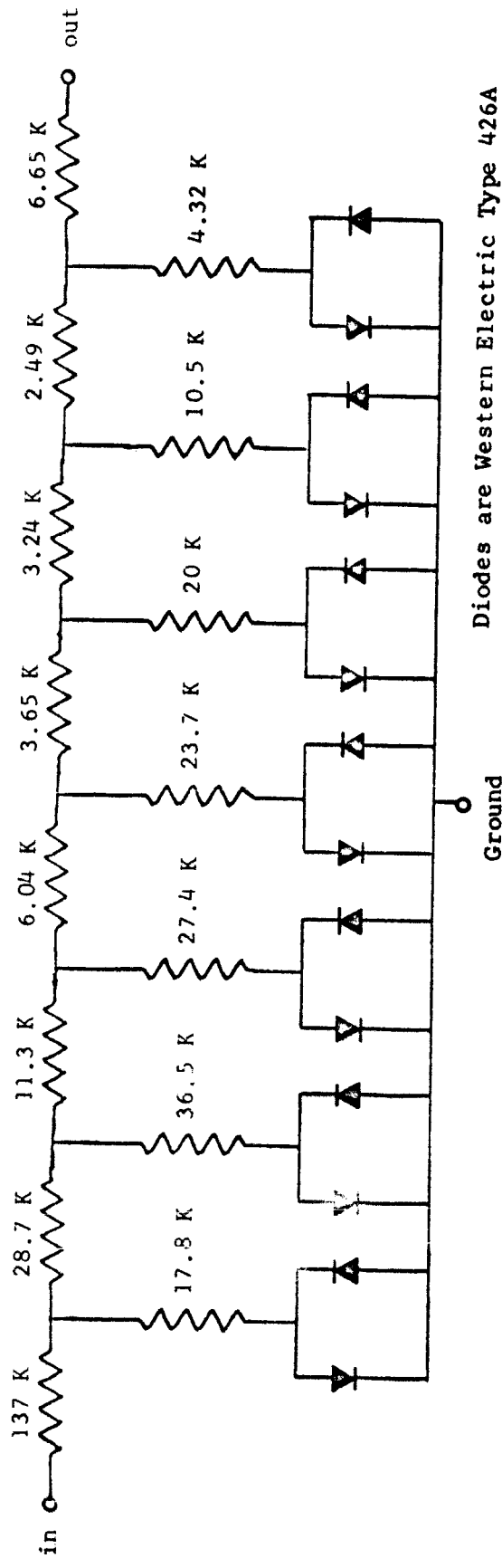
Table 3.1. Pressure Drop-Flow Rate Data For Lines

Line	Pressure Drop lb/in ²	Flow Rate gal/min	Flow Coefficient in ⁴ / lb-sec
High Pressure Fuel Duct to Filter Manifold	11.0	120	139.3
Filter Manifold to Pitch Actuator	26.3	83	62.3
Filter Manifold to Yaw Actuator	31.0	83	57.3
Pitch or Yaw Actuator to Checkout Valve	17.0	85	79.4

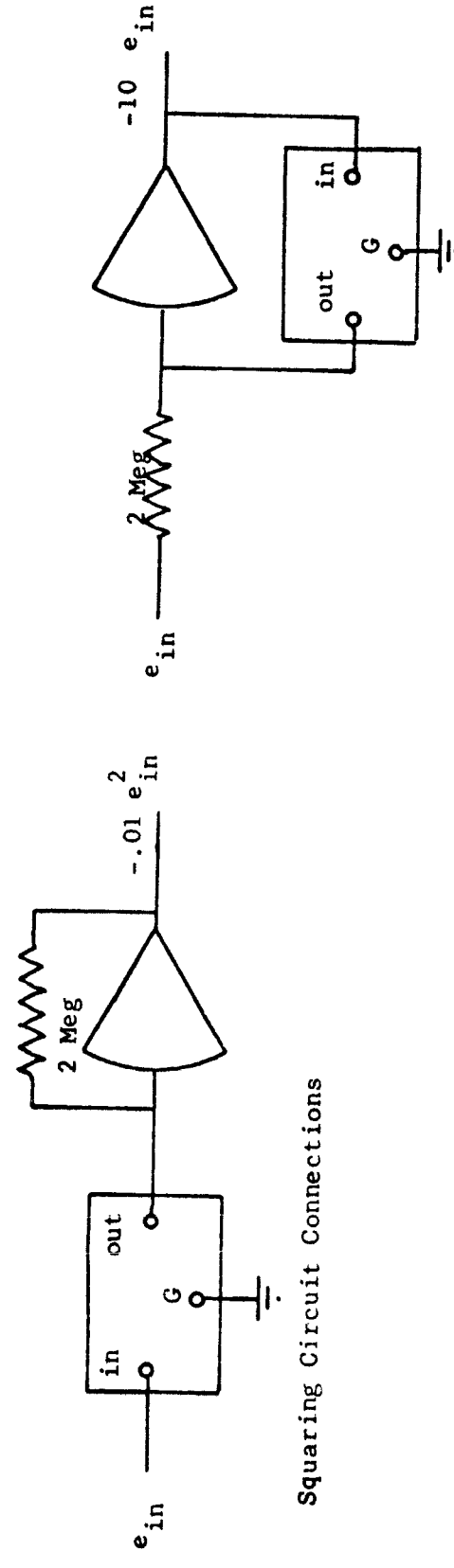
Table 3.2. Filter Manifold Characteristics

Pressure Drop		Flow Rate	
lb/in ²	volts	gal/min	volts
9.2	2.9	60	10
17.3	5.4	90	15
27.2	8.5	120	20
49.0	15.4	180	30
54.0	16.9	220	36.7

100 volts = 318.7 psi
 100 volts = 600 gpm
 = 2310 in³/sec



Diodes are Western Electric Type 426A
Ground



Square Root Circuit Connections

Square Root Circuit Connections

Fig. 3-1. Diagram for Squaring and Square Root Circuits.

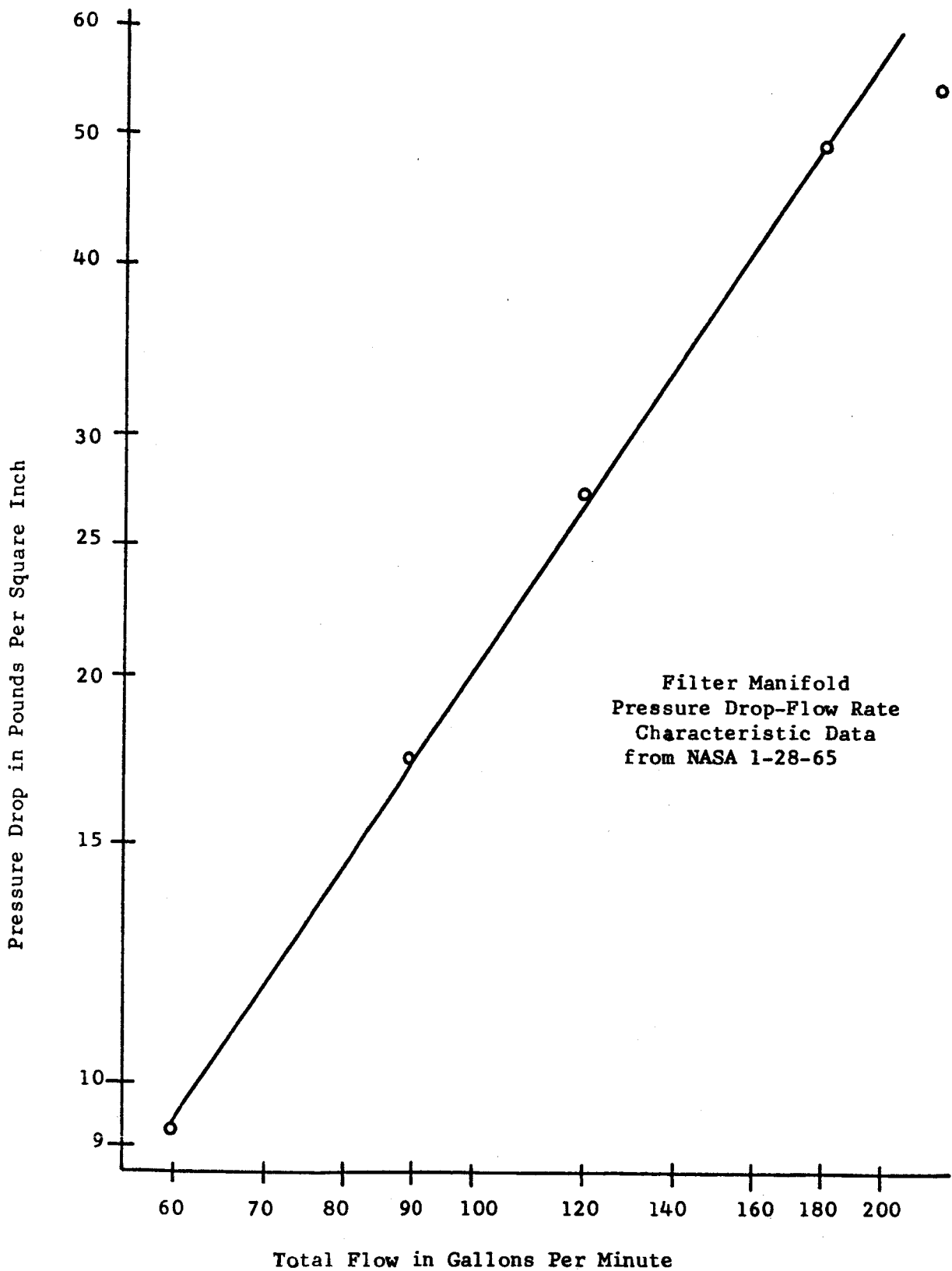


Fig. 3.2. Pressure Drop-Flow Rate Characteristic of Filter Manifold

of filter clogging.

A simplified block diagram of the system is shown in Fig. 3-3. Definitions of the symbols used in the simulation are presented in Table 3-3. This diagram does not include the gas generator, the turbo pump or RP-1 tank.

The equations describing the pressure drop-flow rate relationship of each of the fluid lines are

$$\begin{aligned}
 Q_i &= K_i \sqrt{P_h - P_{hm}} \\
 Q_{ip} &= K_{ip} \sqrt{P_{lm} - P_{hsp}} \\
 Q_{op} &= K_{op} \sqrt{P_{lsp} - P_{hc}} \\
 Q_o &= K_o \sqrt{P_{lc} - P_{low}} \\
 Q_i &= Q_{ip} + Q_{iy} \\
 Q_o &= Q_{op} + Q_{oy} \\
 P_{hc} &= P_{lc}
 \end{aligned} \tag{3.1}$$

This set of equations assumes zero pressure drop across the checkout valve.

The analog computer diagram for Equation Set 3.1 and the filter manifold is given in Fig. 3.4. The simulation is time-scaled such that 100 seconds of computer time is equivalent to 1 second of real time.

SIMULATION OF ACTUATOR

A pictorial diagram of the actuator assembly is given in Fig. 3.5. The equations describing the pressure-flow rate relations of the main metering valve are

Table 3.3 Definition of Symbols Used in Simulation

A_d	Area of "slew" piston	in. ²
A_o	Area of "slew" orifice	in. ²
A_p	Area of actuator piston	in. ²
A_1, A_2	Areas of pressure summing piston	in. ²
B	Buels Modulus	lb-sec/in. ²
D_L	Structural Damping	lb-sec/in.
F_L	External loading force on engine	lb
F_G	Gimbal Friction	lb
K_d	Spring Constant of "slew" piston	lb/in.
K_i	Flow coefficient, input line to manifold	in. ⁴ / lb-sec
K_{ip}	Flow coefficient, input line to actuator, pitch channel	
K_L	Structural Spring Constant	lb/in.
K_o	Flow coefficient, "slew" orifice	in. ³ / lb-sec
K'_o	Flow coefficient, output line from checkout valve	in. ³ / lb-sec
K_{op}	Flow coefficient, output line from actuator pitch channel	in. ³ / lb-sec
K_S	Spring Constant of pressure summing piston	lb/in.
K_{2q}	Flow coefficient, valve spool	in. ³ / lb-sec
M_L	Engine Mass	lb-sec ² /in.
M_p	Actuator Piston Mass	lb-sec ² /in.
P_h	Pump Pressure	psi
P_{hc}	Pressure at checkout valve inlet	psi
P_{hm}	Pressure at filter inlet	psi
P_{hsp}	Pressure at pitch actuator inlet	psi
P_{hsy}	Pressure at yaw actuator inlet	psi
P_{lc}	Pressure at checkout valve outlet	psi
P_{lm}	Pressure at filter outlet	psi
P_{law}	Pressure at sump	psi
P_{lsp}	Pressure at pitch actuator outlet	psi
P_{lsy}	Pressure at yaw actuator outlet	psi
P_1, P_2	Pressure at either side of actuator piston	psi
P'_1, P'_2	Pressure at either side of "slew" piston	psi

Q_1	Total Flow into filter	in. ³ /sec
Q_{ip}	Flow into pitch actuator	in. ³ /sec
Q_{iy}	Flow into yaw actuator	in. ³ /sec
Q_o	Total Flow out of checkout valve	in. ³ /sec
Q_{op}	Flow out of pitch actuator	in. ³ /sec
Q_{oy}	Flow out of yaw actuator	in. ³ /sec
Q_{1c}, Q_{2c}	Compressibility flow in either half of actuator	in. ³ /sec
Q_{1i}, Q_{2i}	Flow into either half of actuator chamber	in. ³ /sec
Q_{1o}, Q_{2o}	Flow out of either half of actuator chamber	in. ³ /sec
Q_{11}, Q_{21}	Flow through "slew" orifice	in. ³ /sec
Q_{12}, Q_{22}	Flow to either half of pressure summing piston	in. ³ /sec
Y_D	Position of "slew" piston	in.
Y_s	Position of pressure summing piston	in.
V_o	Initial volume either side of actuator	in. ³
V_1, V_2	Volume either side of actuator	in. ³
β_c	Engine Command Signal	in.
β_L	Engine Position	in.
β_p	Actuator piston position	in.
σ	Ratio of computer time to system time	
μ_i, μ_o	Effective lapping of inlet and return	in.

Note: A variable with a subscript M indicates the maximum value attained by the variable. This quality is used in scaling of the equation for the analog computer simulation.

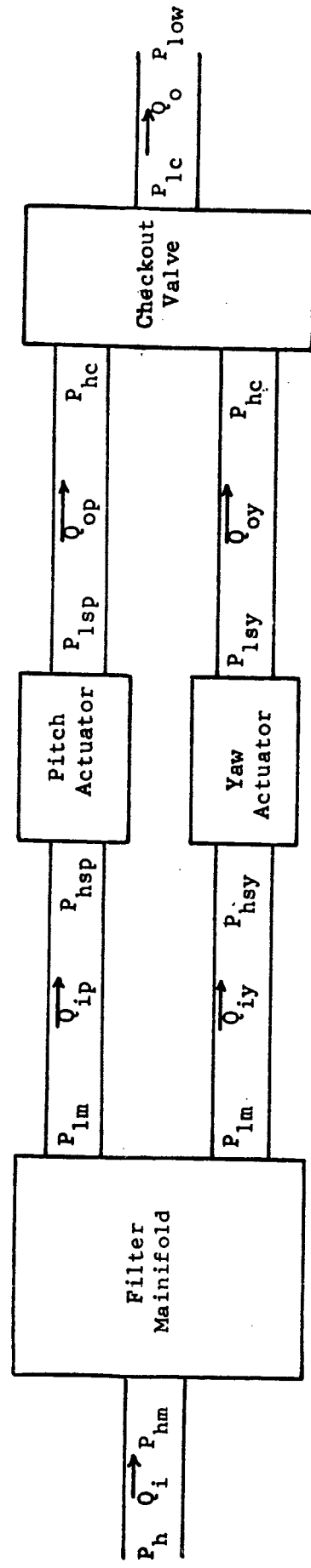


Fig. 3.3. Block Diagram of System

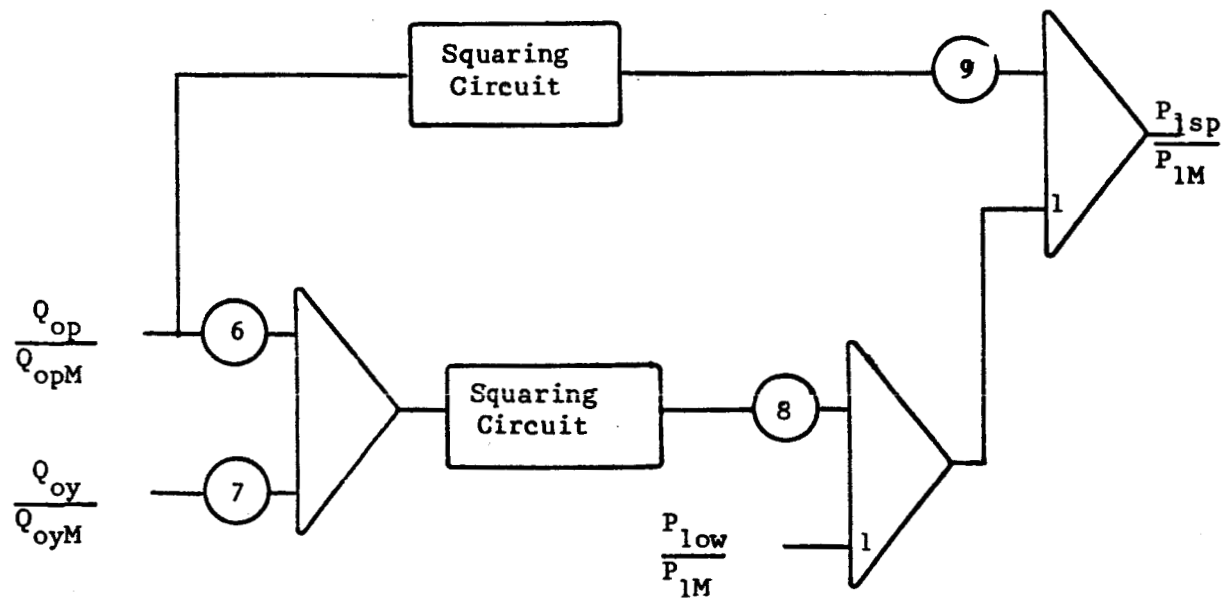
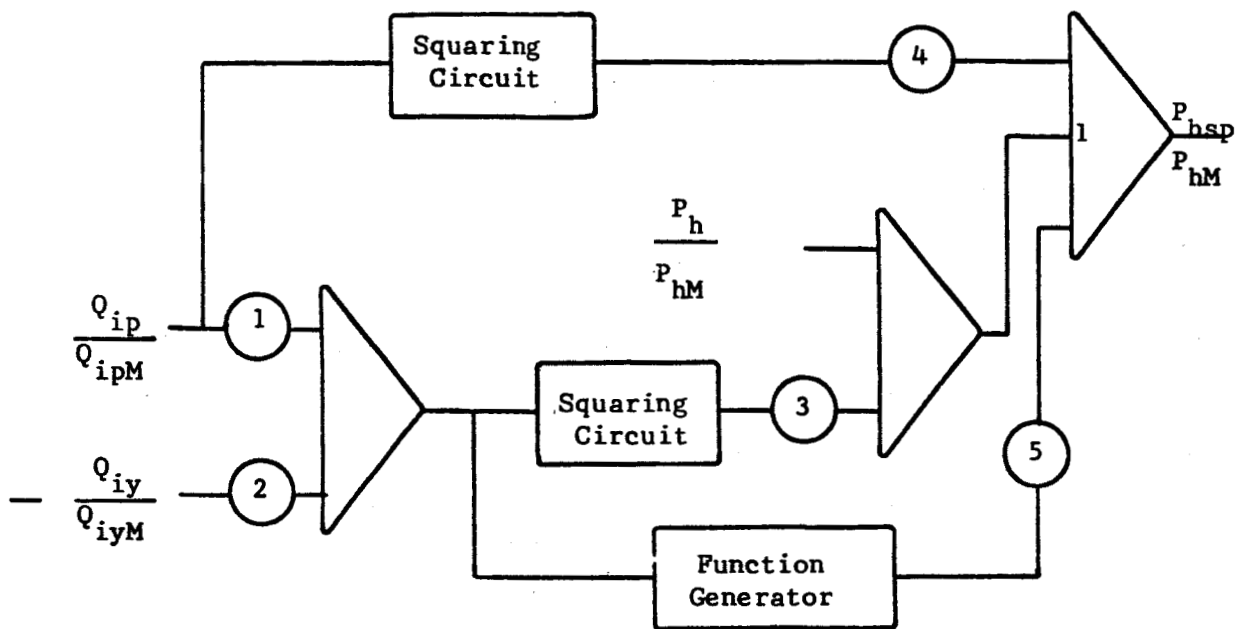


Fig. 3.4. Simulation of Lines and Filter Manifold

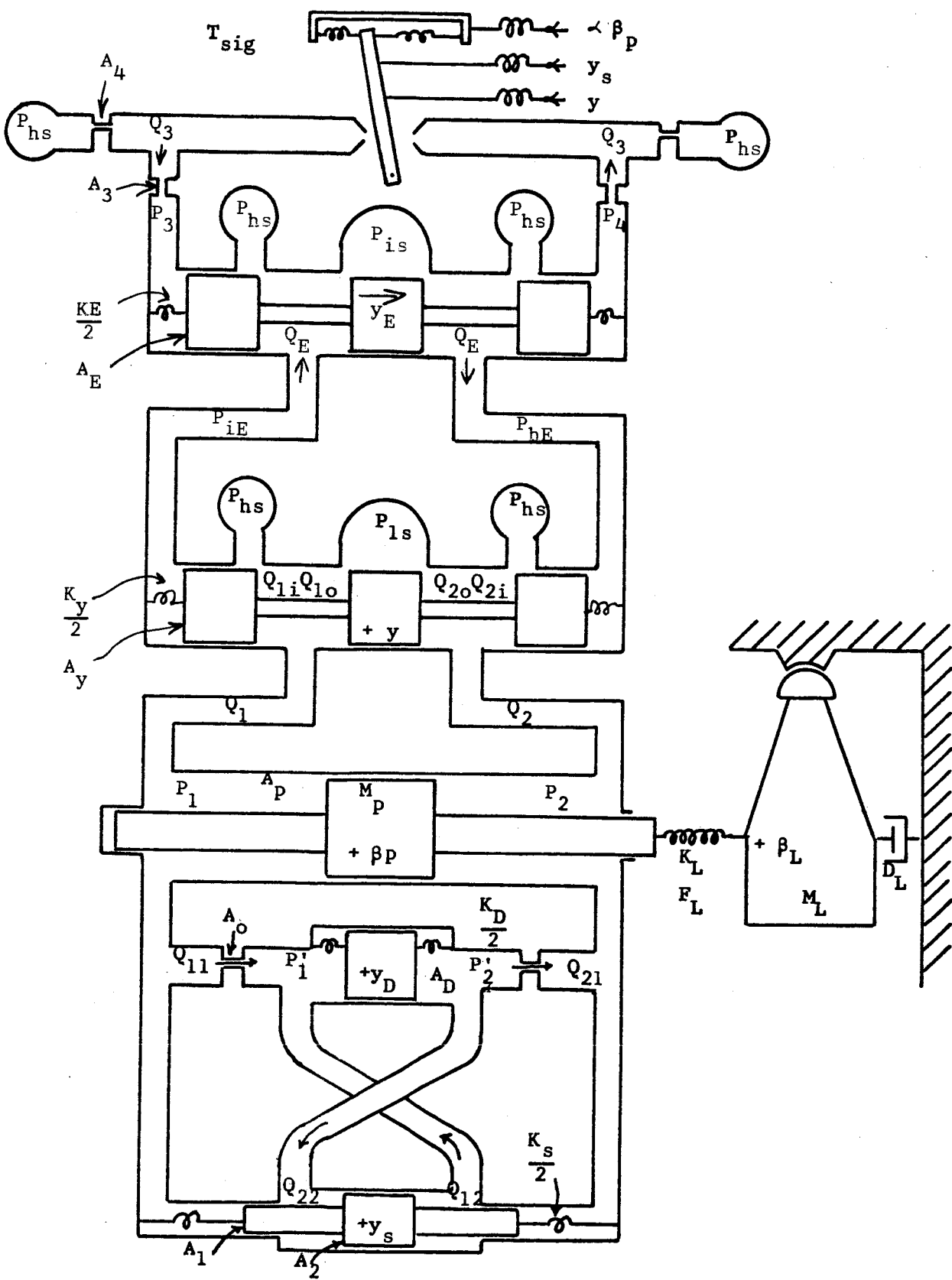


Fig. 3.5 Actuator Assembly

$$Q_1 = Q_{1i} - Q_{10}$$

$$Q_2 = Q_{2i} - Q_{20}$$

$$Q_{1i} = \begin{cases} K_2 q (\mu_i + y) \sqrt{P_{hs} - P_1} & \text{for } \mu_i + y > 0 \\ 0 & \text{for } \mu_i + y < 0 \end{cases}$$

$$Q_{2i} = \begin{cases} K_2 q (\mu_i - y) \sqrt{P_{hs} - P_2} & \text{for } \mu_i - y > 0 \\ 0 & \text{for } \mu_i - y < 0 \end{cases} \quad (3.2)$$

$$Q_{10} = \begin{cases} K_2 Q (\mu_0 - y) \sqrt{P_1 - P_{ls}} & \text{for } \mu_0 - y > 0 \\ 0 & \text{for } \mu_0 - y < 0 \end{cases}$$

$$Q_{20} = \begin{cases} K_2 Q (\mu_0 + y) \sqrt{P_2 - P_{ls}} & \text{for } \mu_0 + y > 0 \\ 0 & \text{for } \mu_0 + y < 0 \end{cases}$$

The analog computer diagram for Equation Set 3.2 is given in Fig.

3.6. It was found desirable to use a single servo multiplier incorporating four potentiometers to provide the function of all the multipliers shown in Fig. 3.6 to reduce the error when the metering spool was in the null position ($y=0$).

The equations for the fluid relationships for the actuator piston are

$$Q_{1c} = Q_1 - A_p \dot{p}_p$$

$$Q_{2c} = Q_2 + A_p \dot{p}_p$$

$$\dot{p}_1 = \frac{B}{V_1} Q_{1c}$$

$$\dot{p}_2 = \frac{B}{V_2} Q_{2c} \quad (3.3)$$

$$V_1 = V_o + A_p \dot{p}_p$$

$$V_2 = V_o - A_p \dot{p}_p$$

The analog simulation for Equation Set 3.3 is given in Fig. 3.7.

The equations which describe the motion of the actuator piston

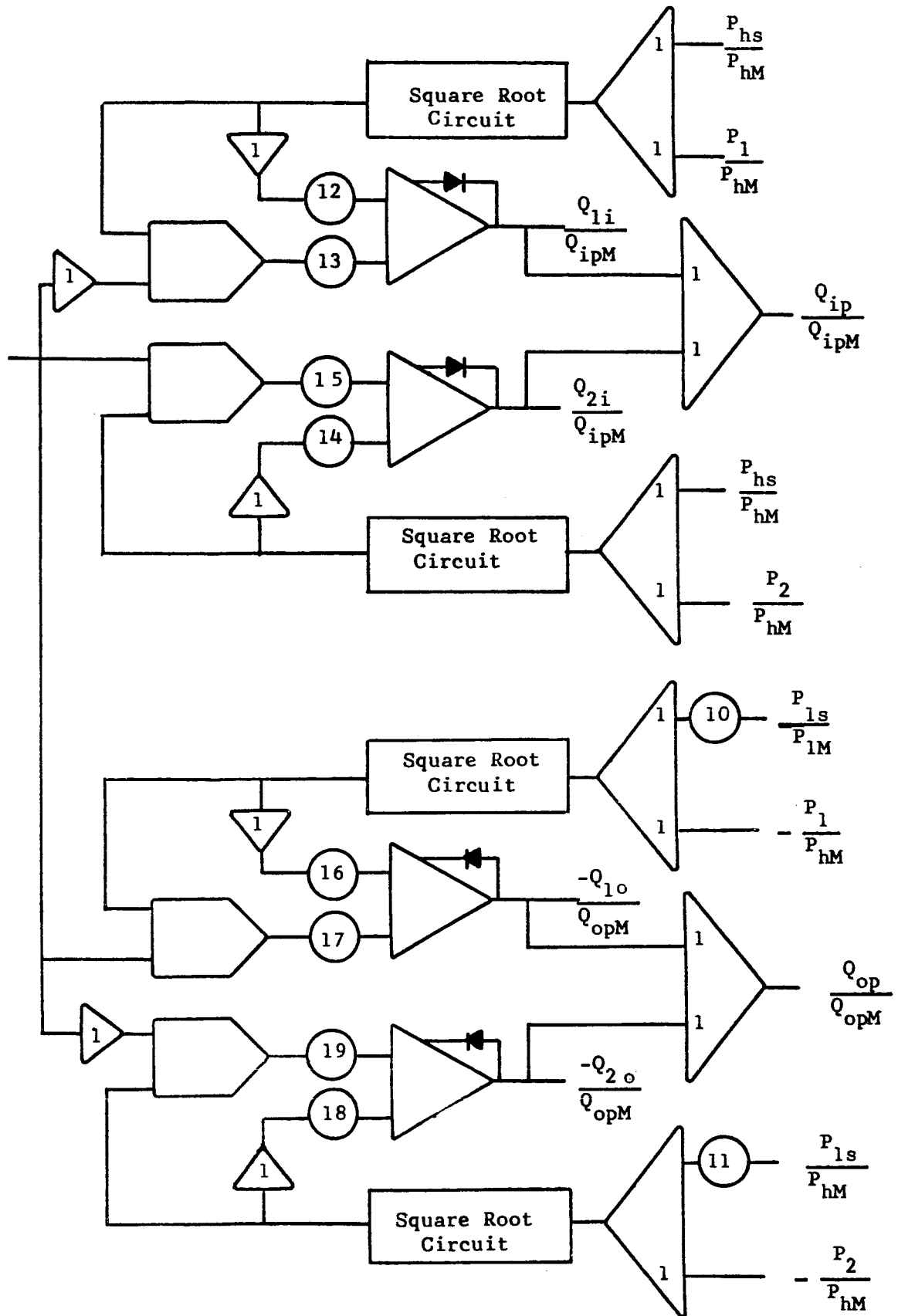


Fig. 3.6. Simulation of Fluid Flow in Main Metering Valve

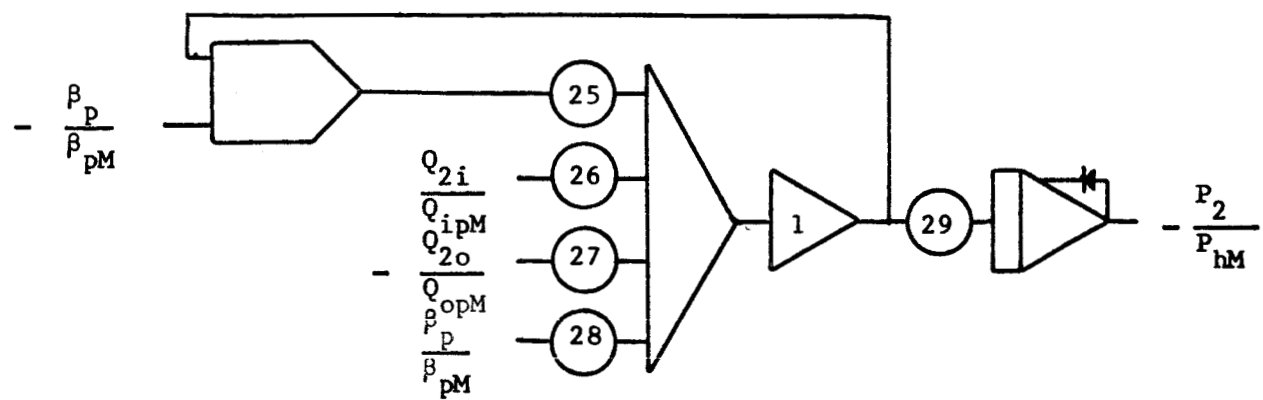
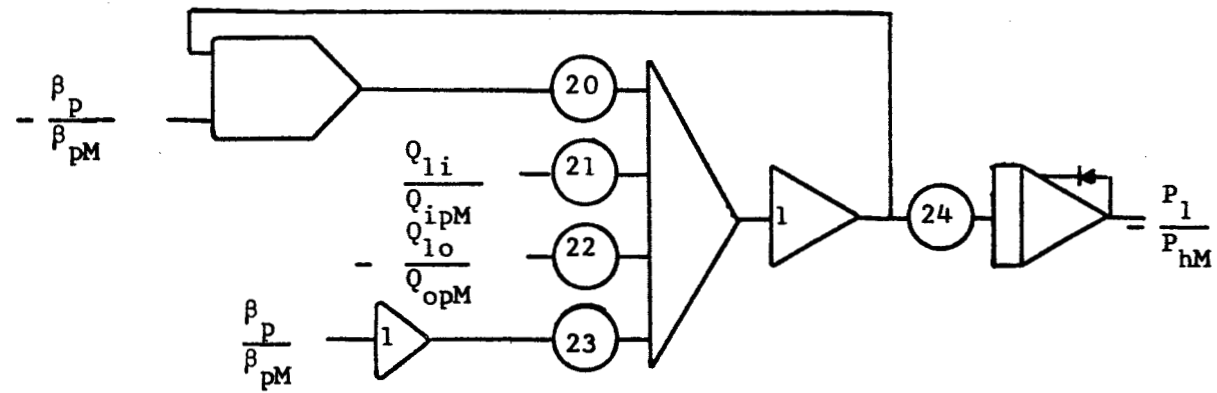


Fig. 3.7. Simulation of Actuator Fluid Equations

and the engine are

$$\begin{aligned} A_p (P_1 - P_2) &= M_p \dot{\beta}_p + K_L (\beta_p - \beta_L) \\ K_L (\beta_p - \beta_L) &= M_L \dot{\beta}_L + D_L \beta_L + F_L + F_G \end{aligned} \quad (3.4)$$

where

$$F_G > 0 \text{ for } \beta_L > 0$$

$$F_G < 0 \text{ for } \beta_L < 0$$

The analog simulation for Equation Set 3.4 is given in Fig. 3.8.

As discussed in Quarterly Report No. 5, the theoretical representation of gimbal friction shown in Fig. 3.9 (a) could not be used since it caused oscillations in the engine position in the absence of a command signal. The modified representation of gimbal friction shown in Fig. 3.9 (b) was used in the final simulation shown in Fig. 3.8.

The following equations describe the pressure feed back network ("slew") are:

$$\begin{aligned} Q_{11} &= Q_{21} = K_o A_o \sqrt{P_1 - P_1'} = K_o A_o \sqrt{P_2' - P_2} \\ (P_1 - P_2) A_1 &= (P_1' - P_2') A_2 - K_s y_s = 0 \\ (P_1' - P_2') A_D &- K_D y_D = 0 \\ Q_{11} + Q_{12} - A_D \dot{y}_D &= 0 \\ Q_{22} + Q_{21} - A_D \dot{y}_D &= 0 \\ Q_{22} &= A_2 y_s = Q_{12} \end{aligned} \quad (3.5)$$

The analog computer diagram for the Equation Set 3.5 is given in Fig. 3.10.

Specific information concerning the orifices and other parameters in the flapper stage and metering spool controlled by the flapper was not available. Consequently, it was necessary to adapt a simulation from

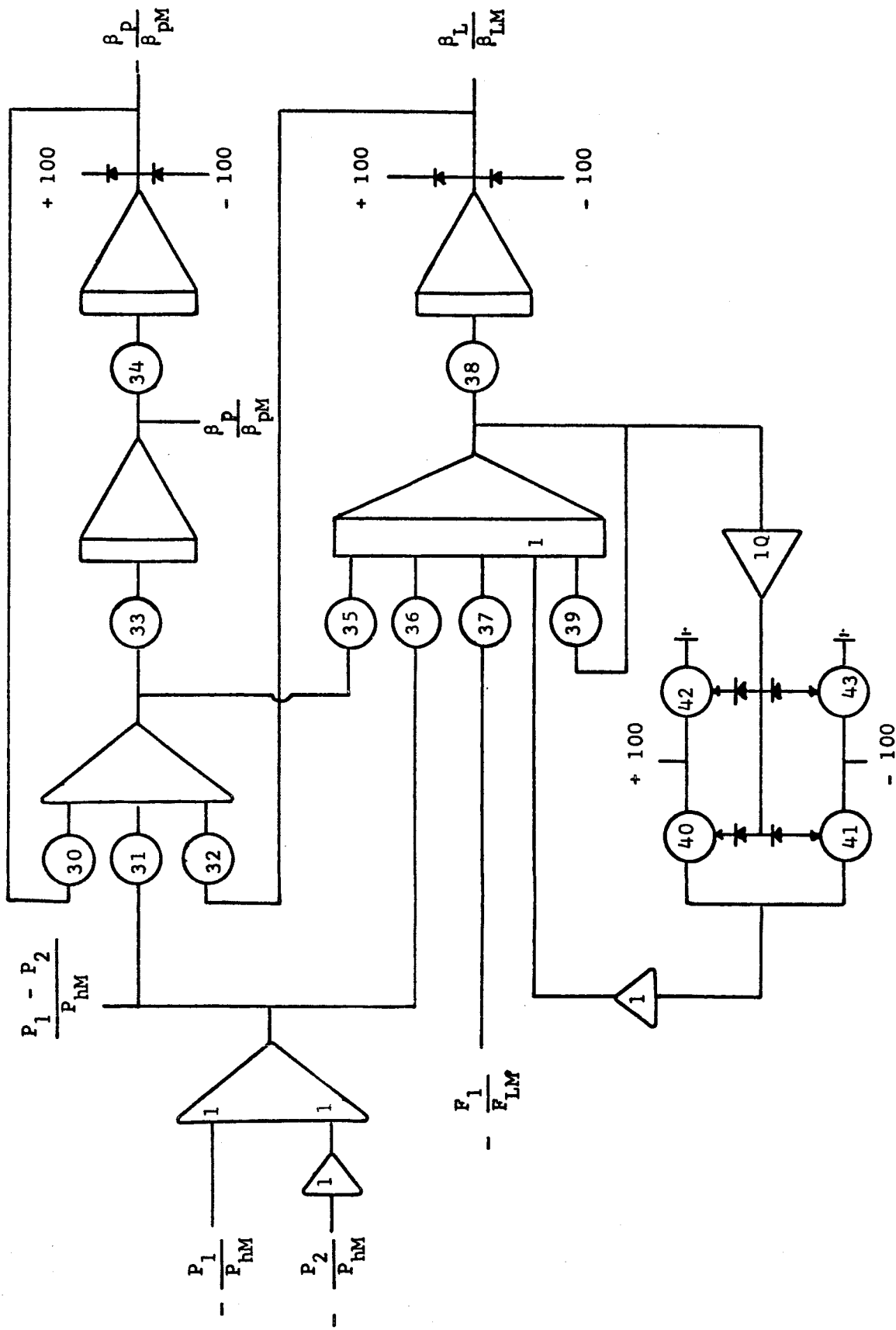
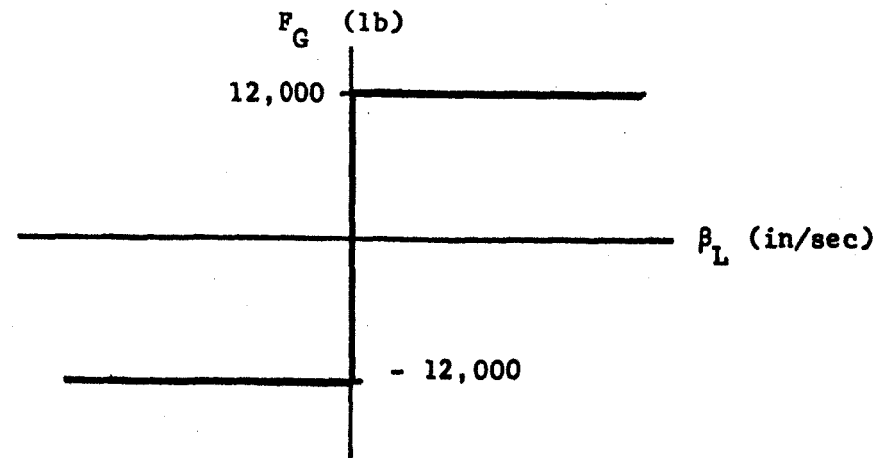
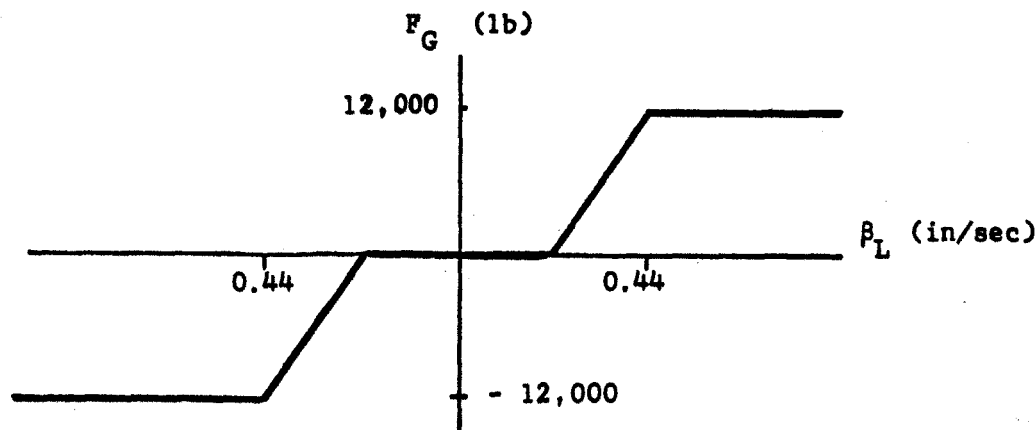


Fig. 3.8. Simulation of Actuator and Engine Position



(a) Theoretical Representation



(b) Representation Used in Simulation

Fig. 3.9. Representation of Gimbal Friction

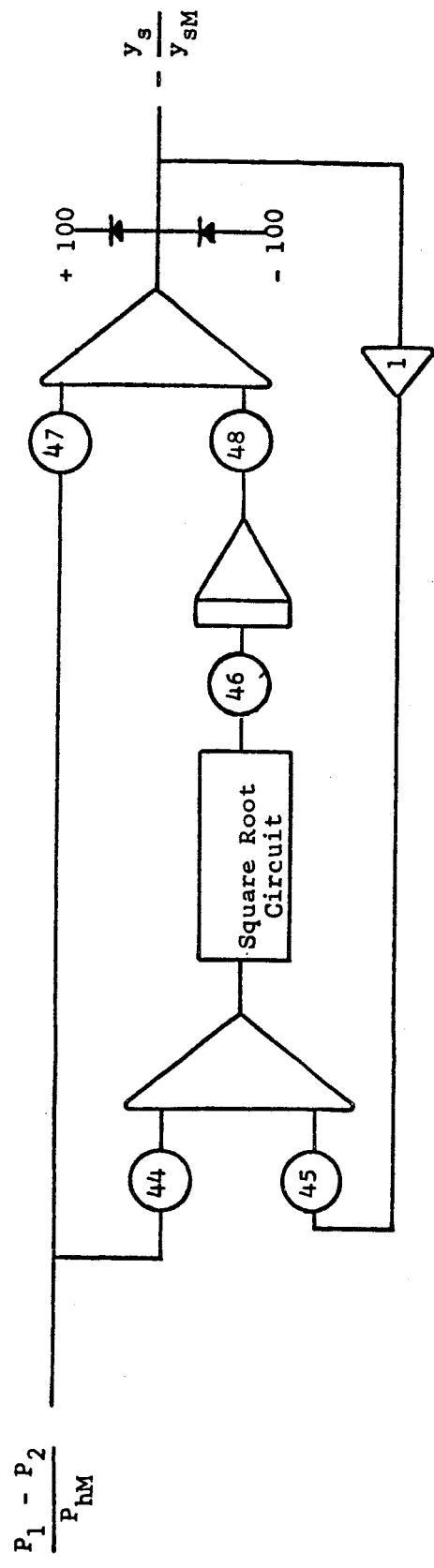


Fig. 3.10 Simulation of Pressure Feedback Network

a report¹² furnished by NASA. This simulation which is shown in Fig. 3.11 is based on a constant pressure differential across the valve and a linearization of most of the pressure drop-flow relations. The adaptation consisted primarily of changing the scaling to conform to that used elsewhere in the problem and the addition of a limit on the spool position simulation. A more exact representation which includes the nonlinearities present in the flapper stage is derived in Appendix A.

The simulation shown in Figs. 3.6 through 3.11 is for the pitch actuator only. An identical simulation is required for the yaw actuator.

ANALOG COMPUTER STUDY OF THE SC-I OPEN-LOOP PROPELLANT-HYDRAULIC SYSTEM

The analog computer model derived in the previous section of this report was utilized to study the system stability and performance. The nonlinearities of the system required such a large amount of computer equipment that only one channel of the control system could be simulated at a time. Since the systems are essentially identical, it was felt that a successful study could be made by using the analog model for one channel with simulated inputs representing the other channel being furnished at the appropriate input points. Such phenomena as the variations in supply and sump pressures were also simulated and furnished as inputs during some of the runs. Biasing was used without change in the shape of the flow characteristic curve in order to simulate a clogged or dirty filter.

The response of the system to various step input commands can be interpreted in terms of the indices of measure used for linear systems, namely, the delay time, the rise time, the settling time, and the percent over shoot. These quantities are as depicted in Figure 4.1. The results

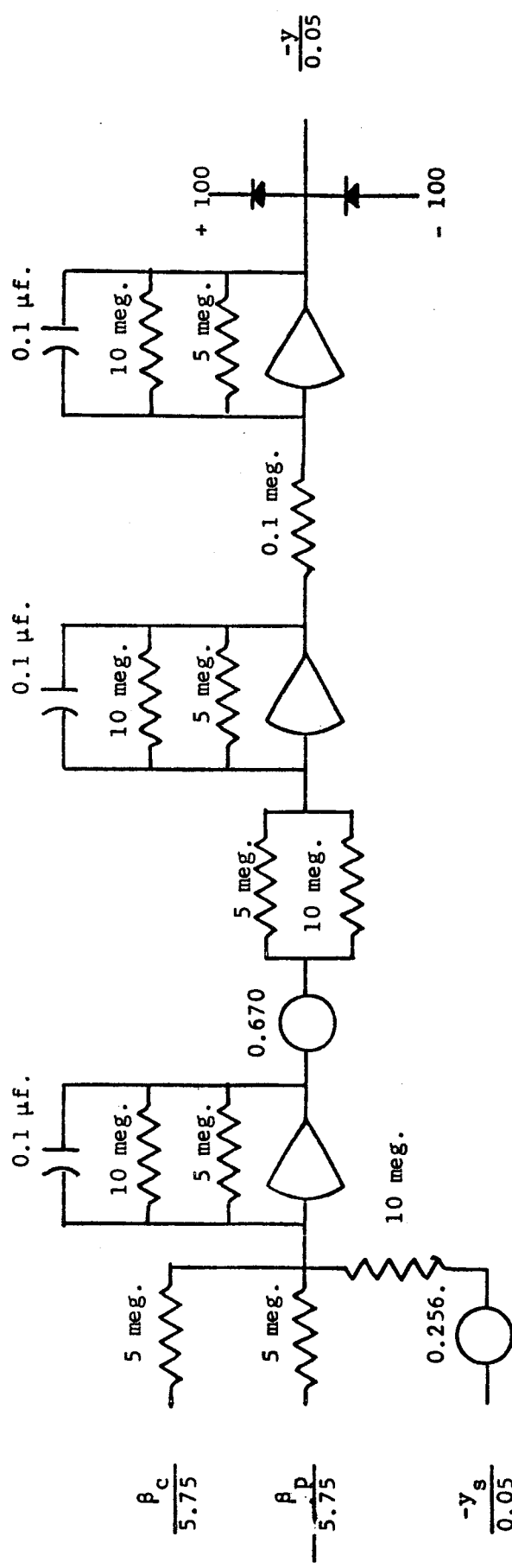


Fig. 3.11. Simulation of Actuator Metering Spool Position Time Scaled 100 to 1

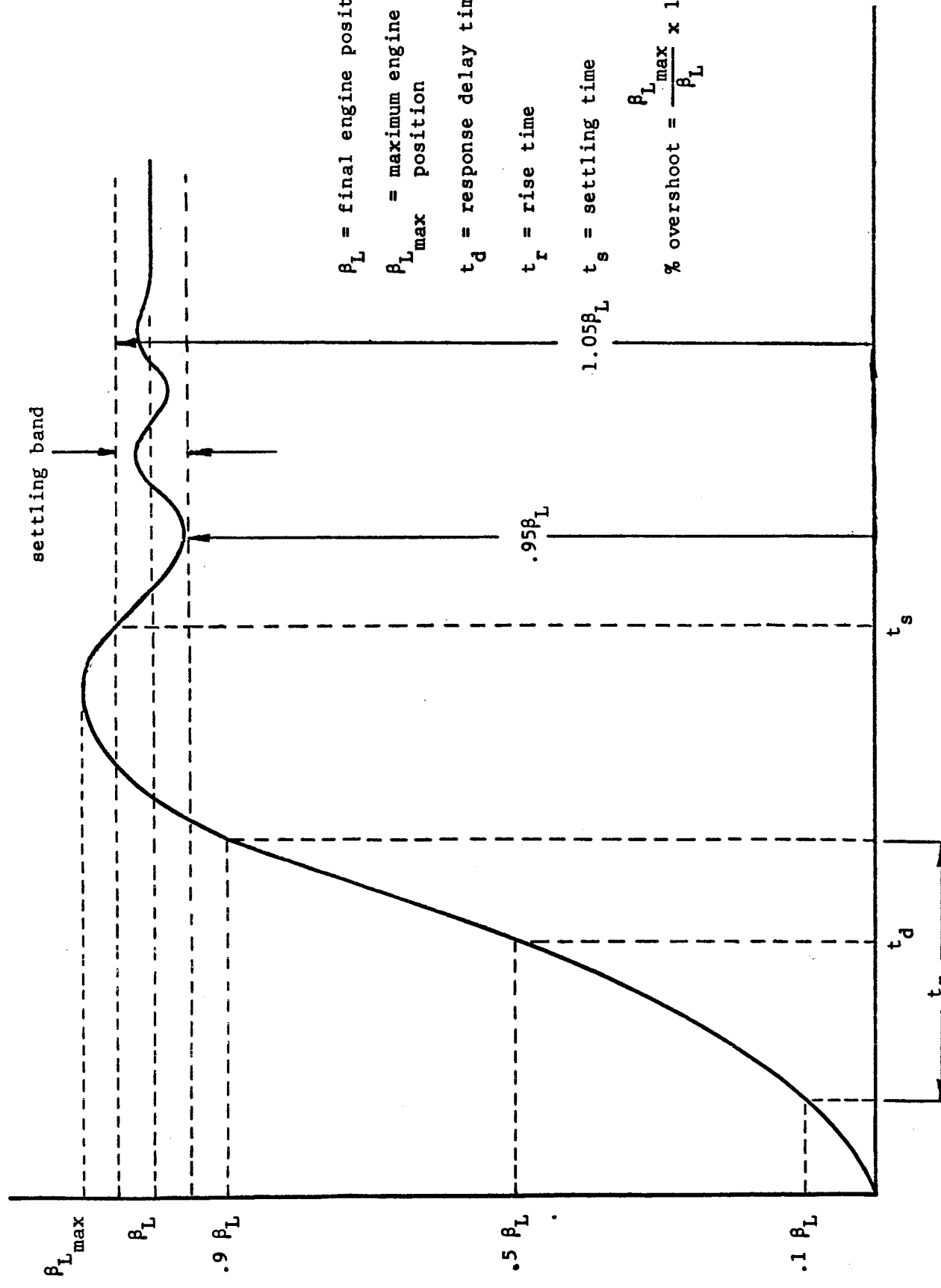


Fig. 4.1. System Indices for Step Function Input Command Signal.

of such an analysis is shown in Table 4.1. The response of the system to the step inputs are shown in Figures 4.2 through 4.12. A significant change in the dynamic behavior was noted to occur between input commands of 1.00 and 1.25 degrees. In order to get a better picture of what was occurring, test were run with metering spool motion and "slew" piston motion being observed as well as the actuator motion, pressure differential across the actuator piston was also recorded. Since the indices given in Figure 4.1, while sufficient for a linear system, must be used with caution when applied to a nonlinear system; it was felt quite important to examine the transient behavior with time. The dynamic behavior of the system as mentioned above is given in Figures 4.13 and 4.14. It is quite evident that the system behavior is markedly different for the two different input commands even though the magnitude change in comparison to the total range covered in the tests. In view of this strange phenomenon, it seemed desirable to obtain a record of the dynamic behavior of the system variables over the entire operating range to ascertain whether this phenomenon was occurring at a singular point or could be observed at other points and simply was not reflected in the linear system indices and therefore overlooked. These data are presented in Figures 4.15 through 4.22 and show that a second type of behavior manifests itself above this point. Attempts were made to determine if the changing of any single variable was precipitating this action. Changing the various feedback loop gains caused the phenomenon to shift with respect to the magnitude of the command signal that was necessary to initiate the actions.¹³ With a decrease sufficient in gain in any one feedback loop, the abrupt change in behavior would diminish. This did not pinpoint any one cause since the same reduction was observed

Table 4.1. System Response To Step Inputs

Step Input (degrees)	Delay Time (seconds)	Rise Time (seconds)	Settling Time (seconds)	Percent Overshoot (%)
0.50	0.06	0.06	0.21	5.6
0.75	0.063	0.06	0.75	13.2
1.00	0.07	0.06	0.64	15.4
1.25	0.075	0.07	0.28	43.6
1.50	0.082	0.085	0.29	45.3
1.75	0.085	0.10	0.31	39.6
2.00	0.092	0.127	0.325	33
2.25	0.105	0.14	0.34	27
2.50	0.115	0.16	0.363	26
2.75	0.135	0.18	0.41	29.4
3.00	0.15	0.20	0.43	28

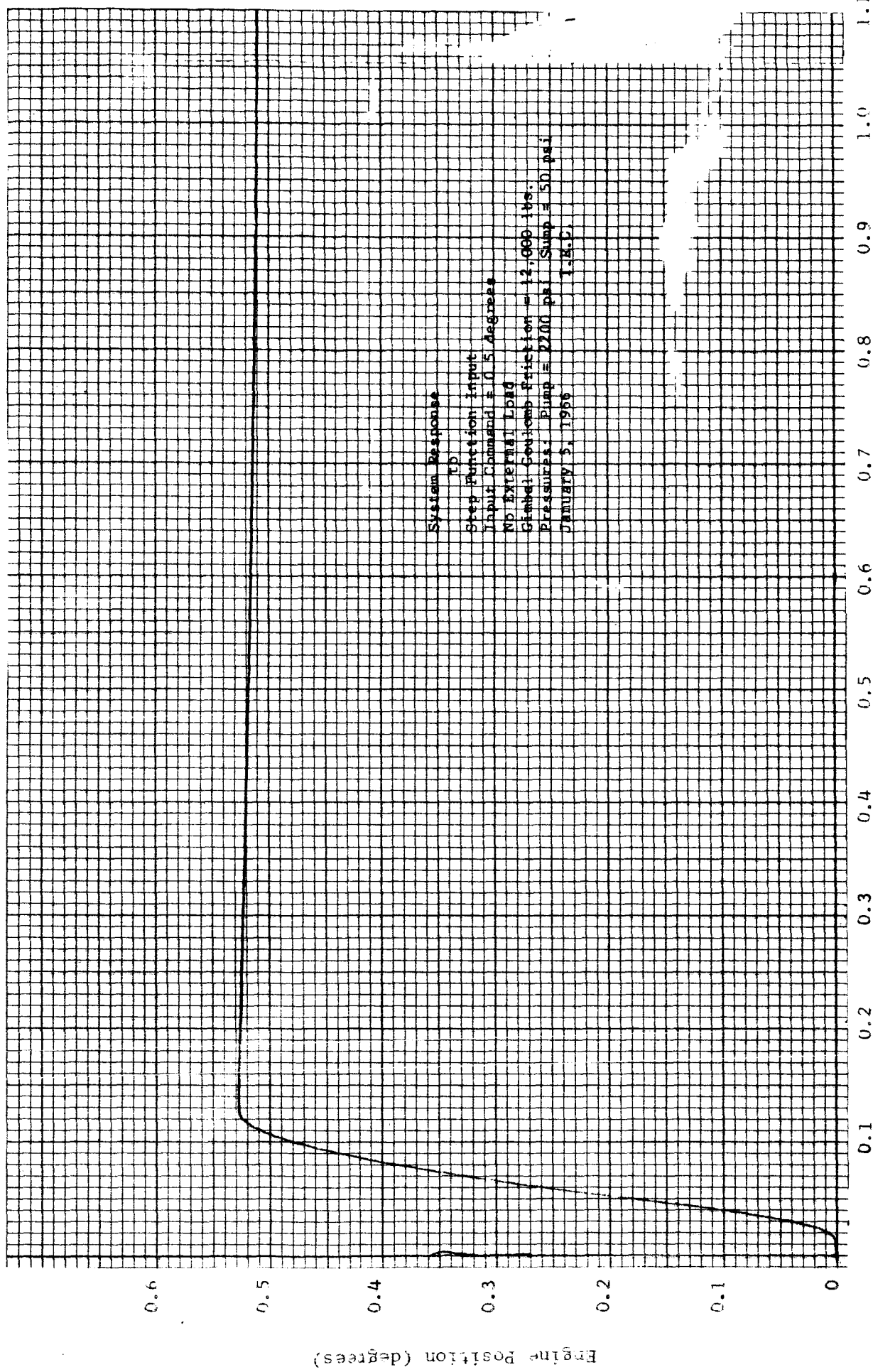


Fig. 4.2. System Response to Step Command of 0.5 Degree.

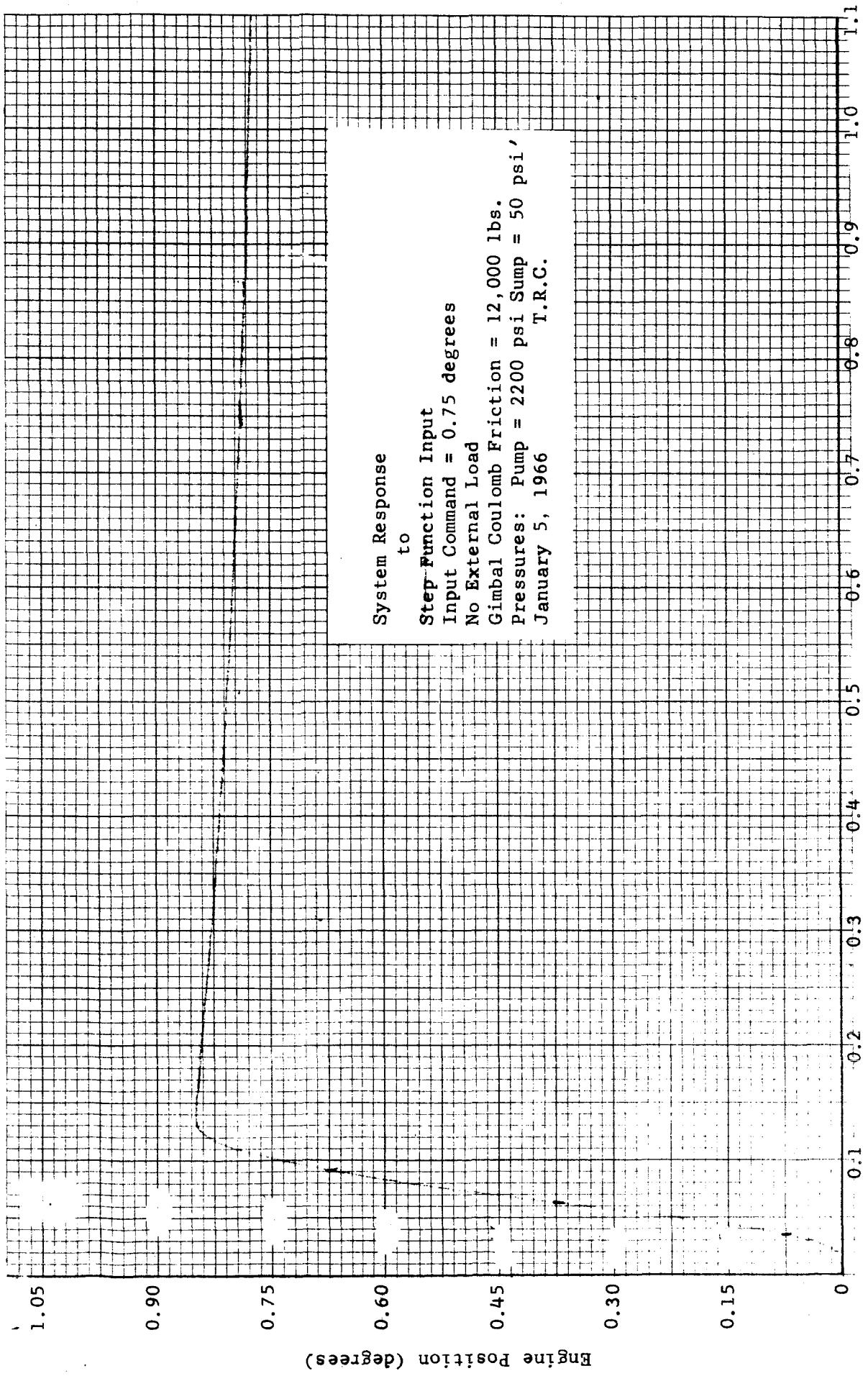


Fig. 4.3. System Response to Step Command of 0.75 Degree.

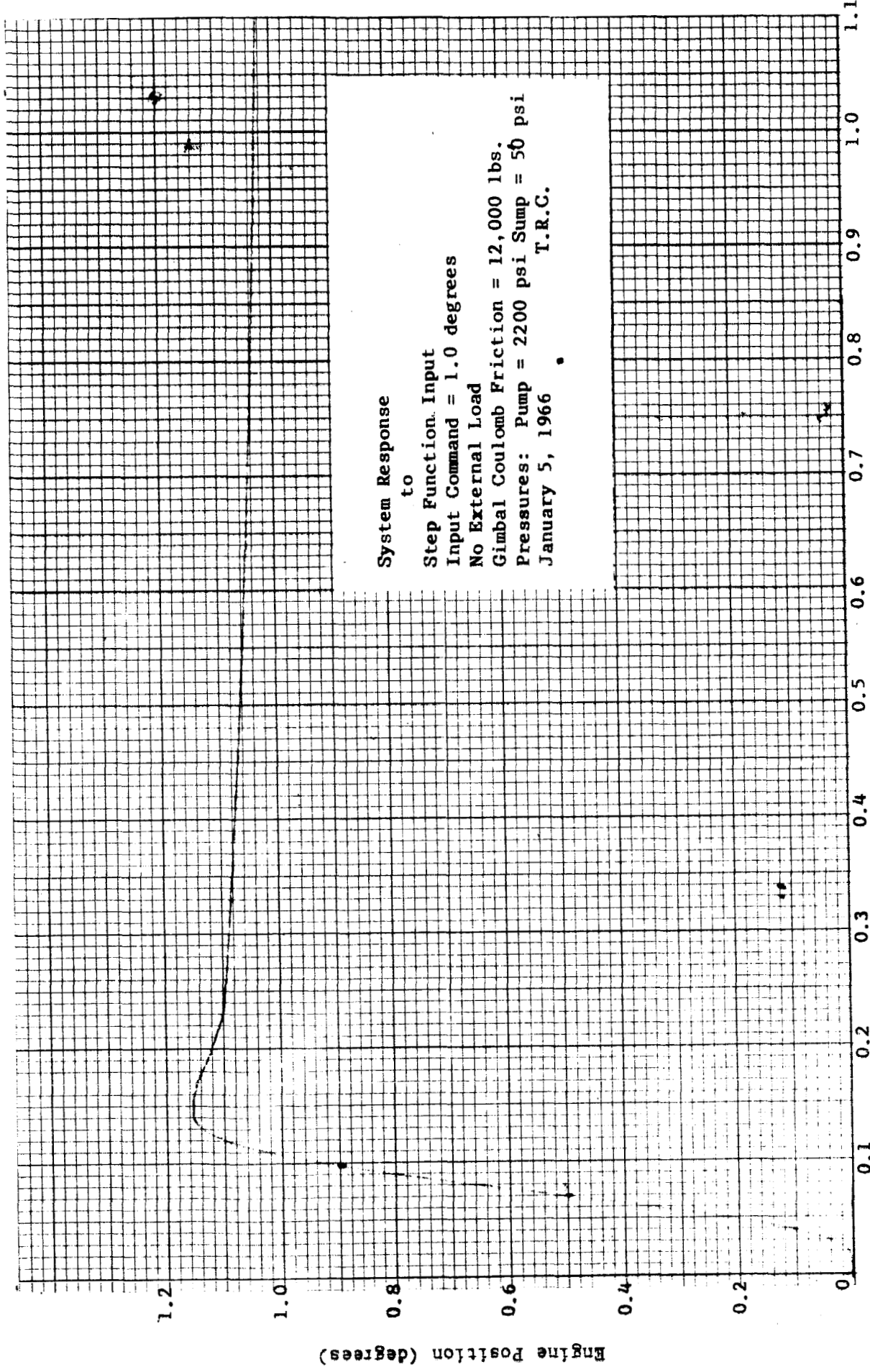


Fig. 4.4. System Response to Step Command of 1.0 Degree.

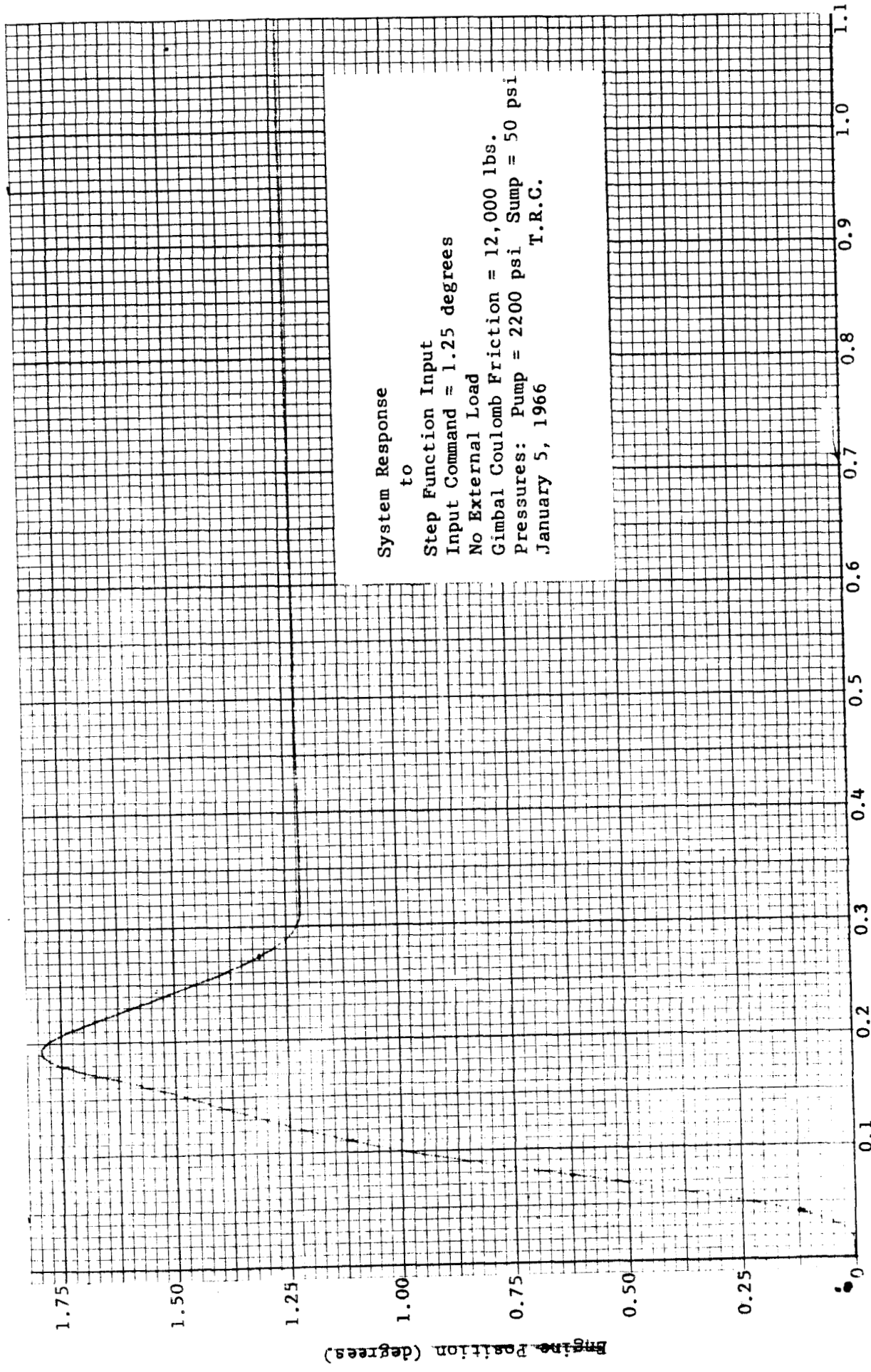


Fig. 4.5. System Response to Step Command of 1.25 Degrees.

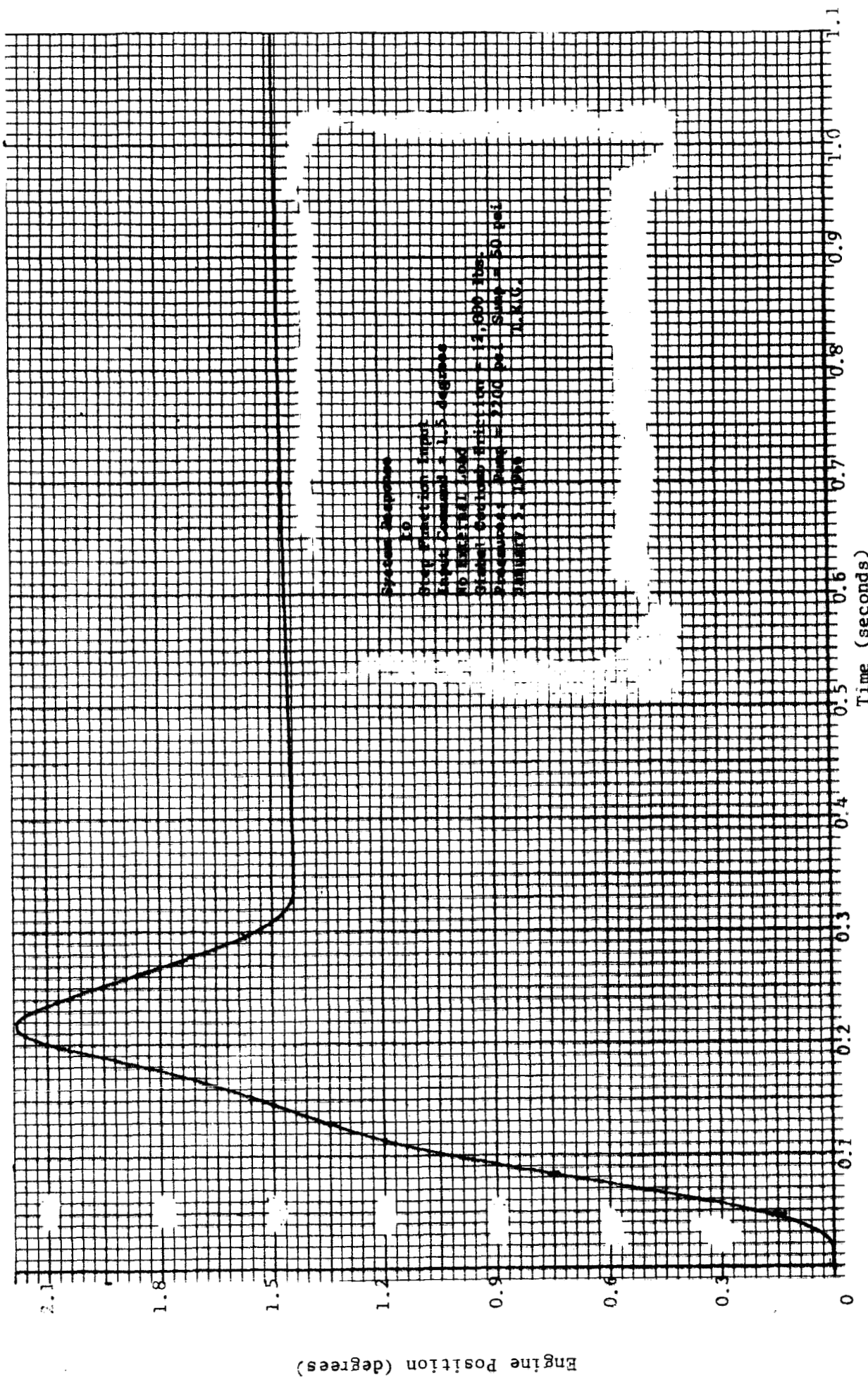


Fig. 4.6. System Response to Step Command of 1.5 Degrees.

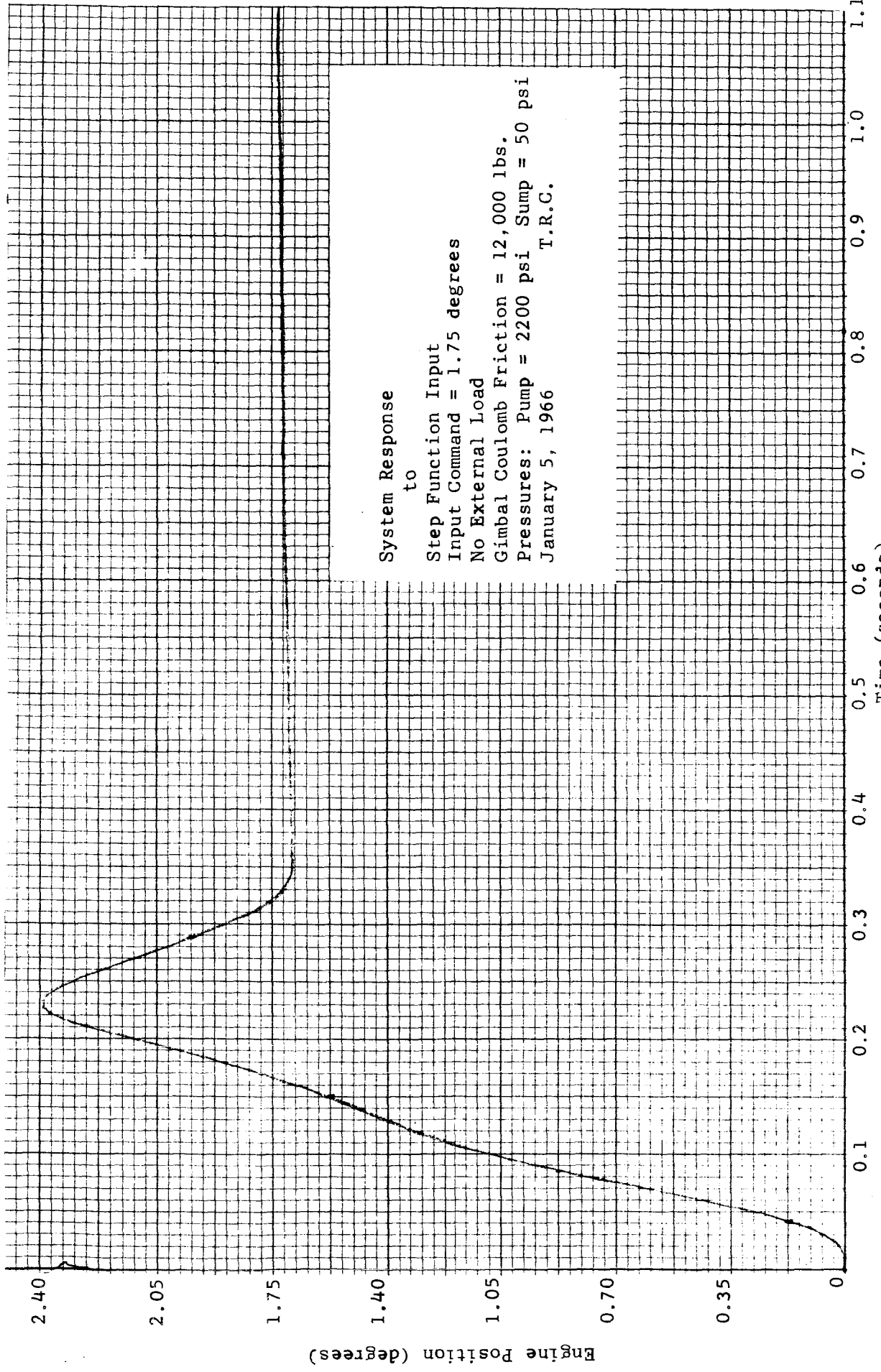


Fig. 4.7. System Response to Step Command of 1.75 Degrees.

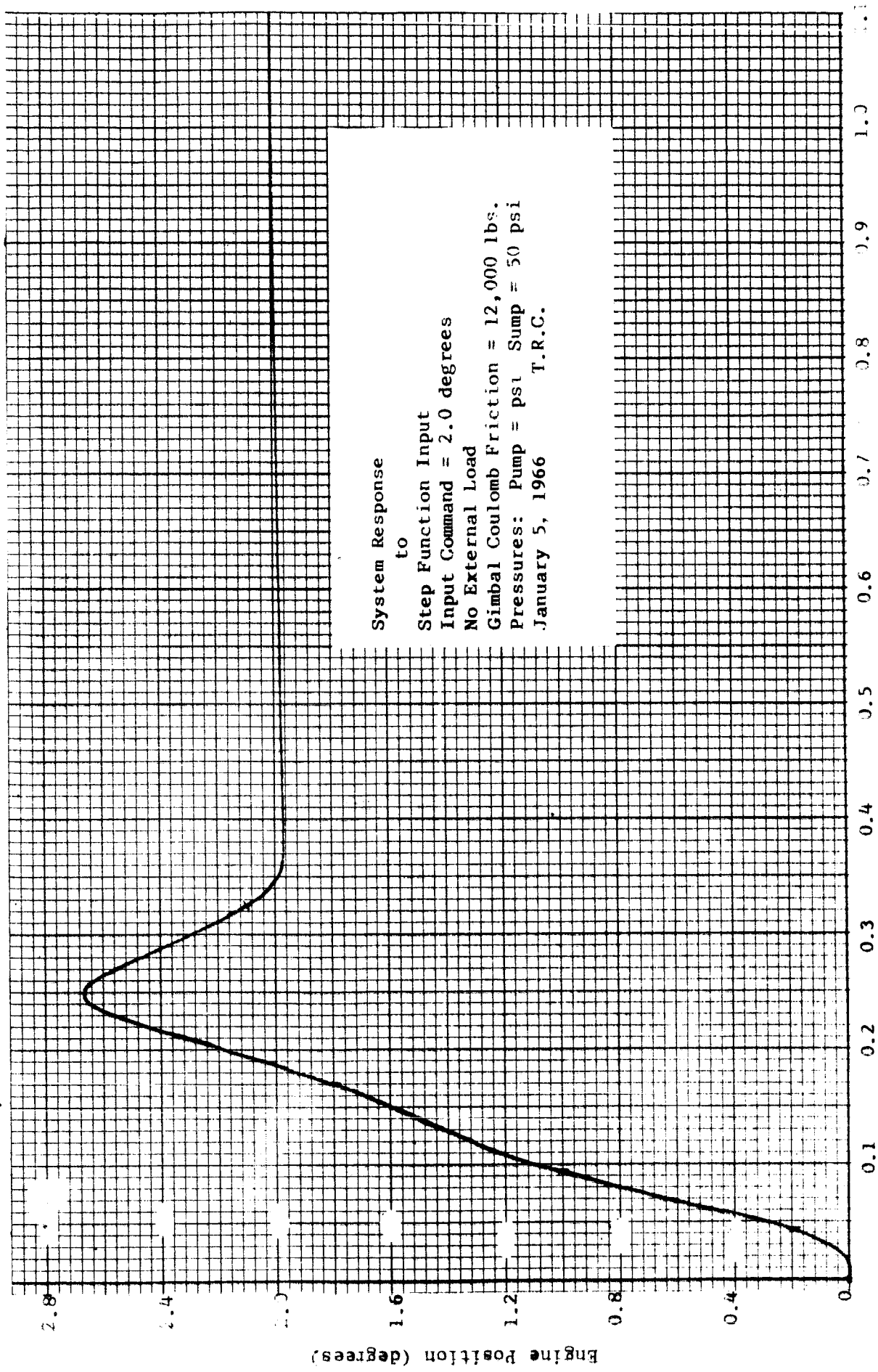


Fig. 4.8. System Response to Step Command of 2.0 Degrees.

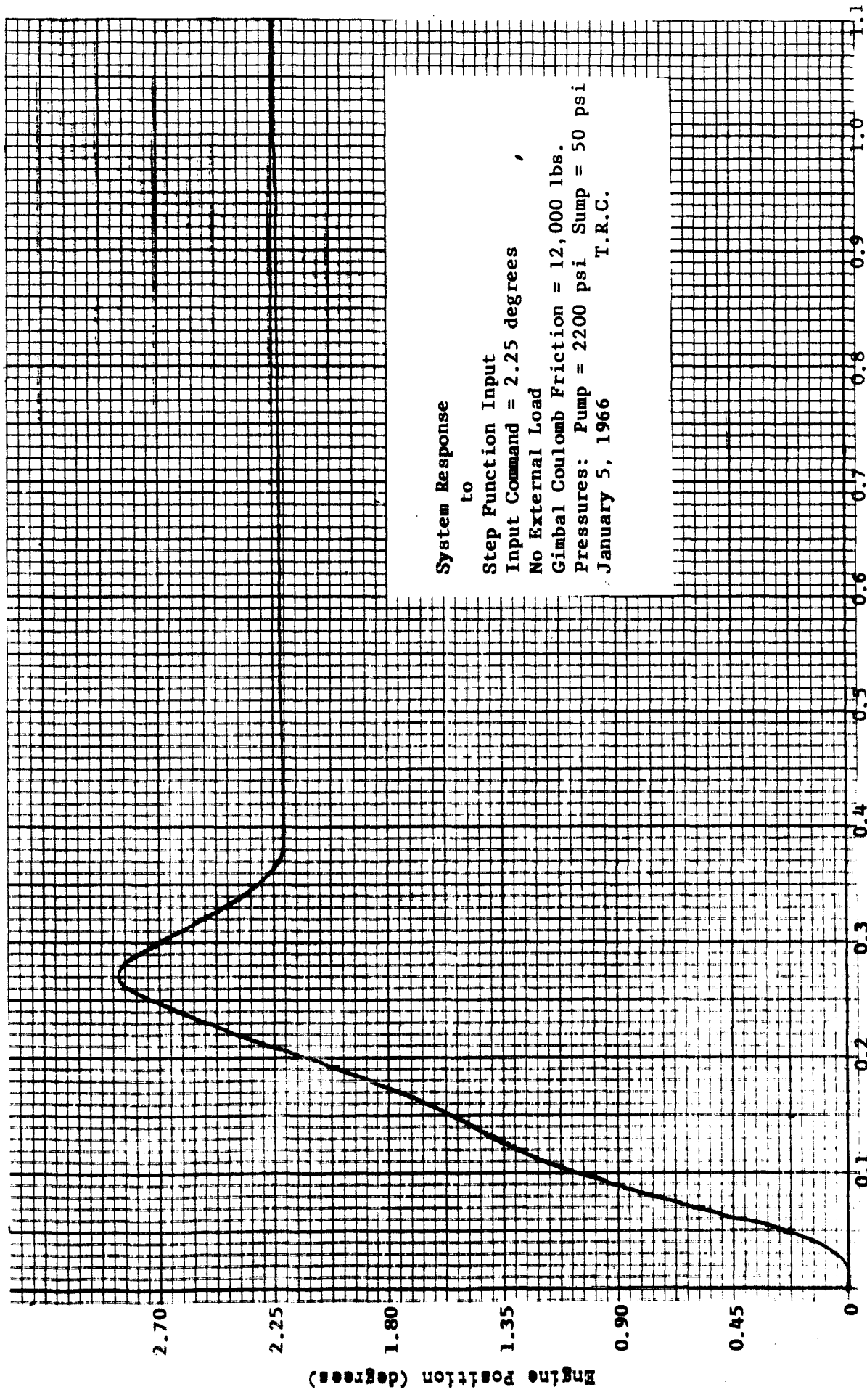


Fig. 4.9. System Response to Step Command of 2.25 Degrees.

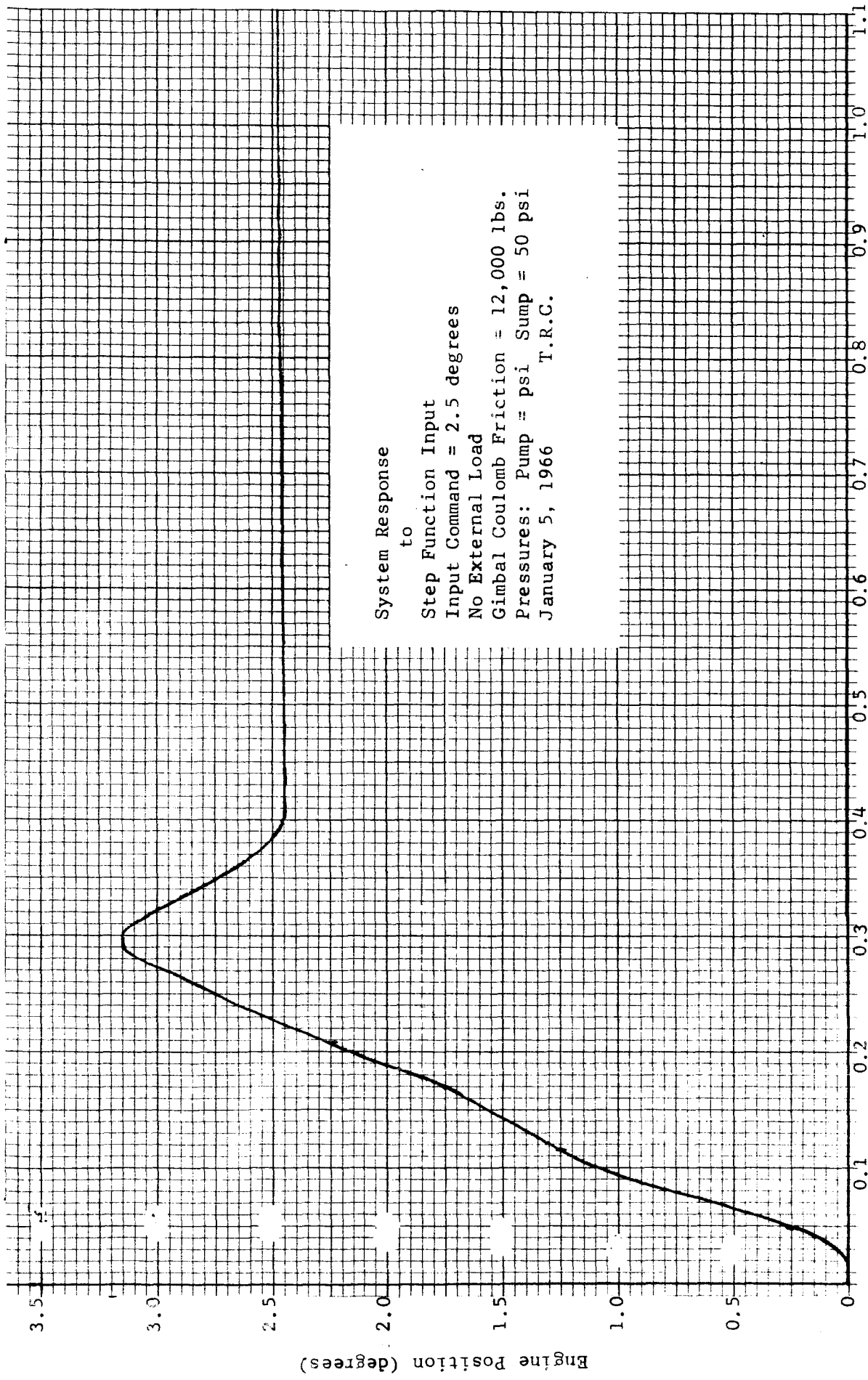


Fig. 4.10. System Response to Step Command of 2.5 Degrees.

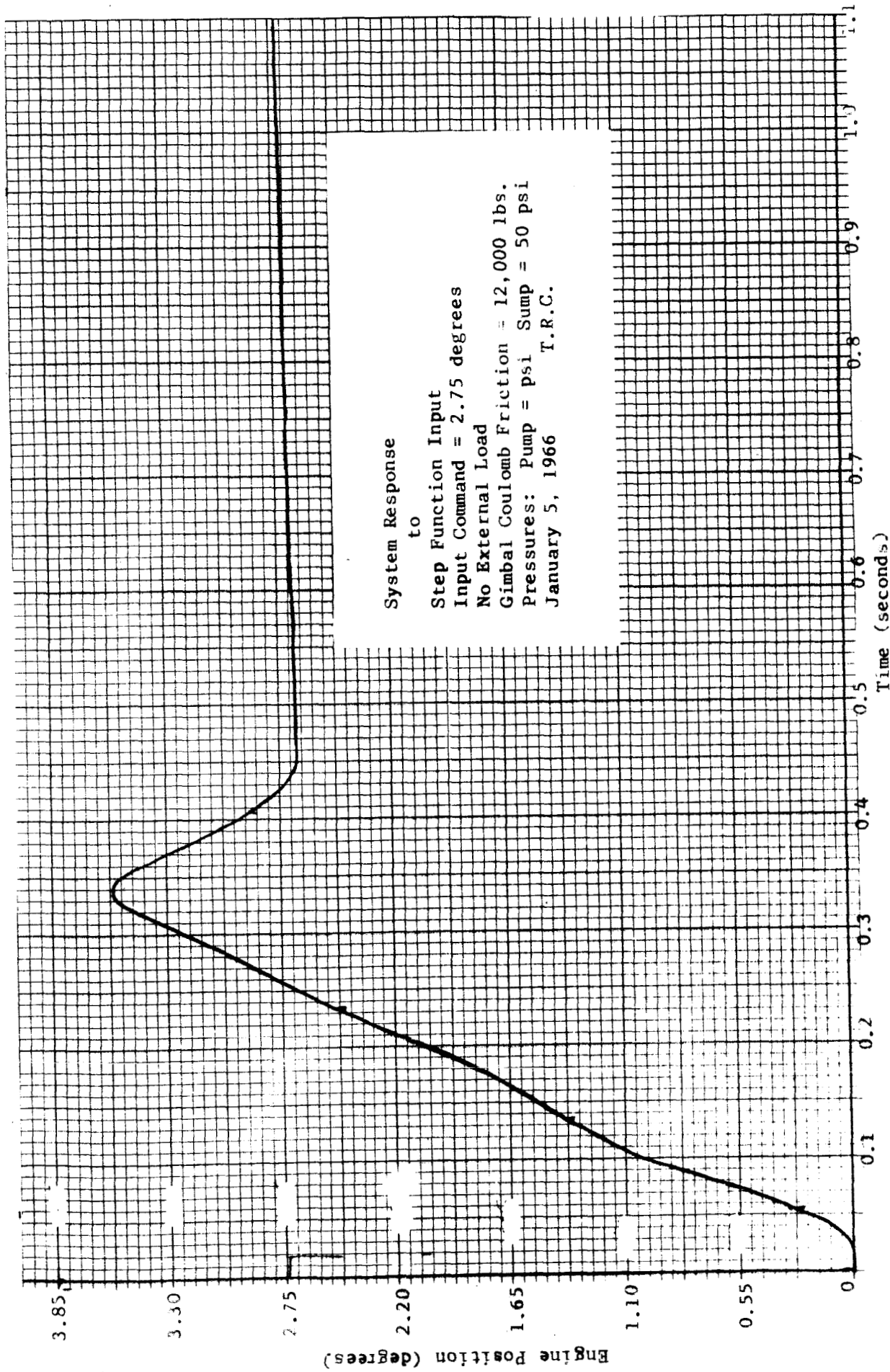


Fig. 4.11. System Response to Step Command of 2.75 Degrees.

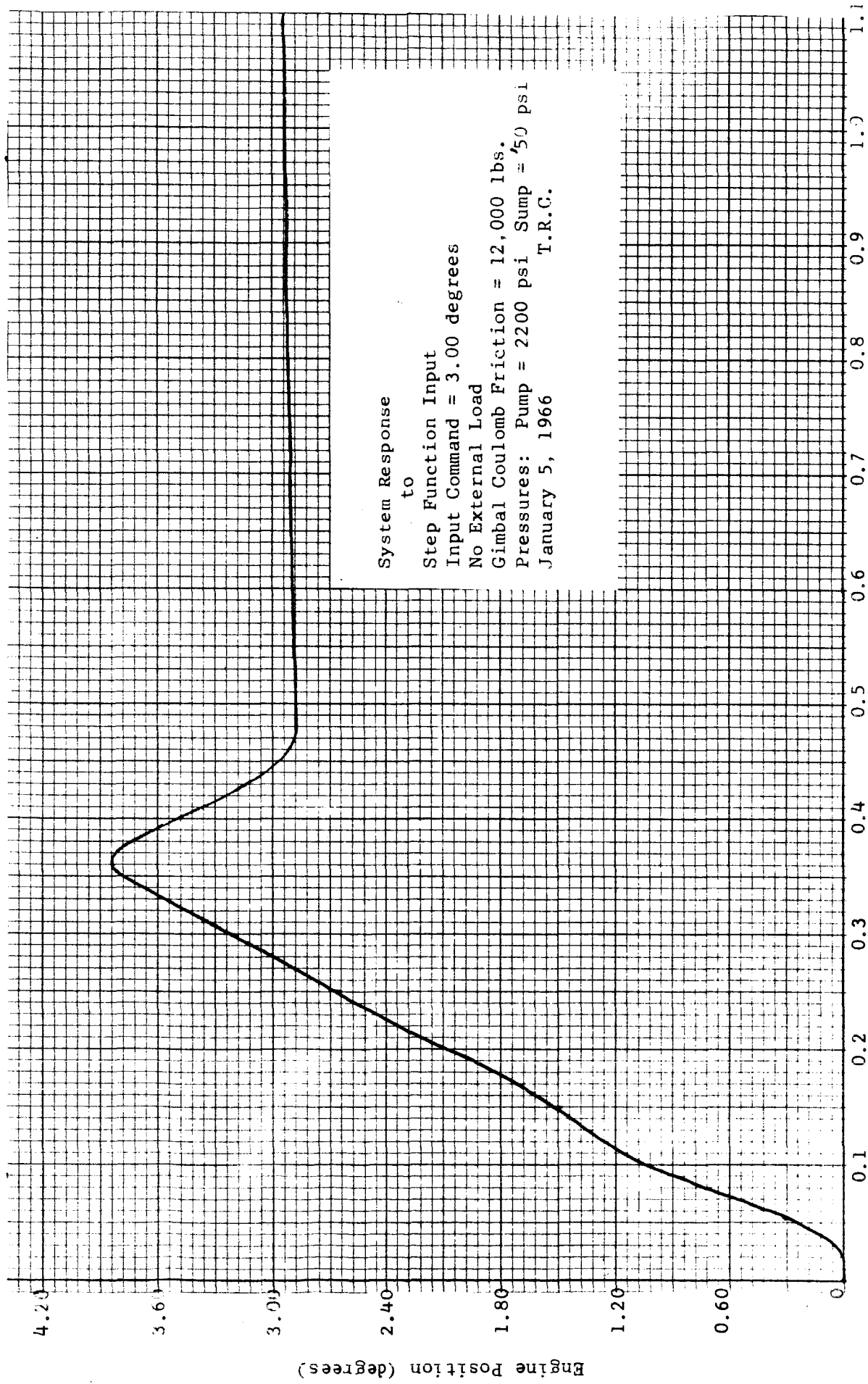


Fig. 4.12. System Response to Step Command of 3.00 Degrees.

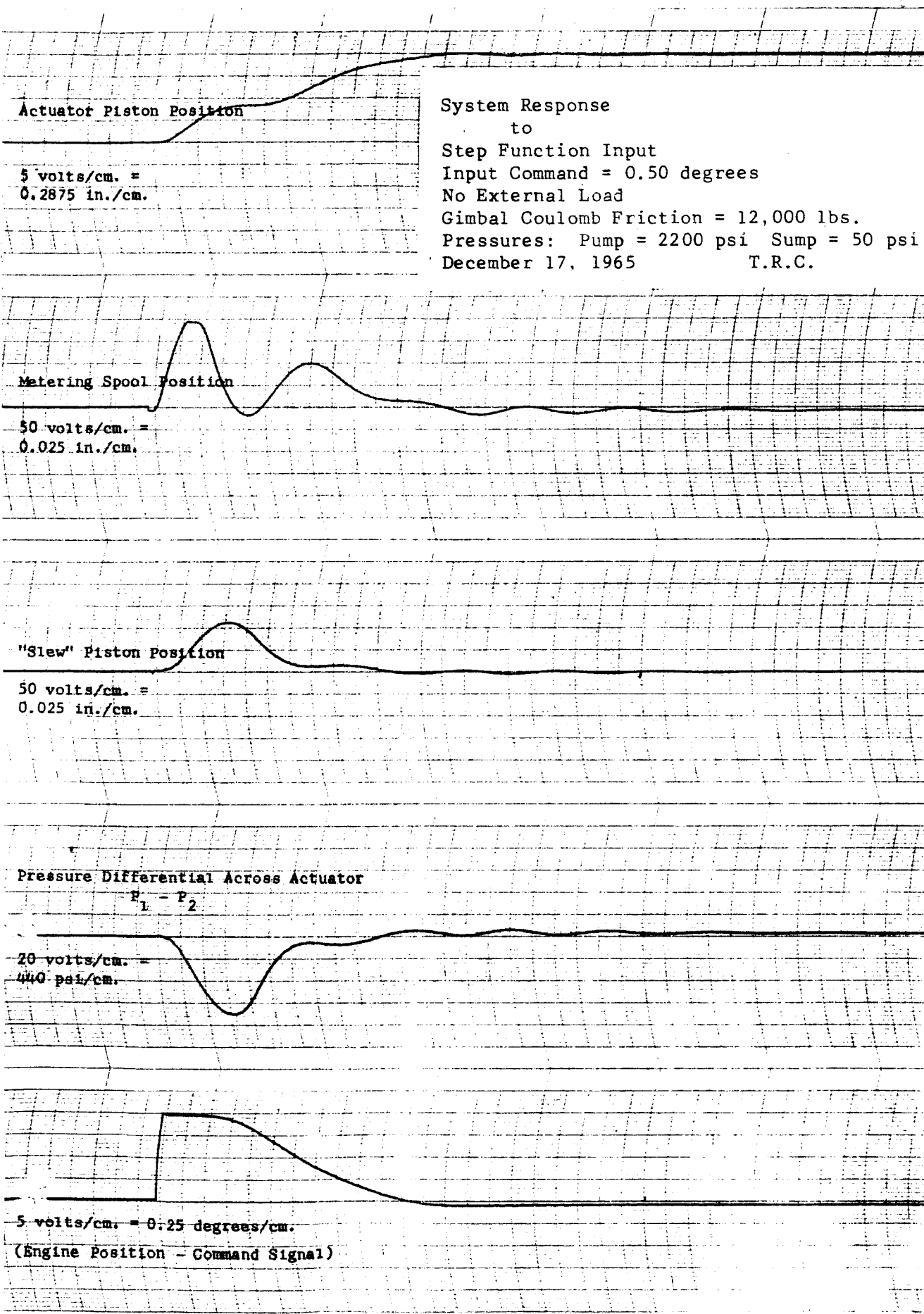


Fig. 4.13. System Dynamic Behavior to Step Command of 0.50 Degree.

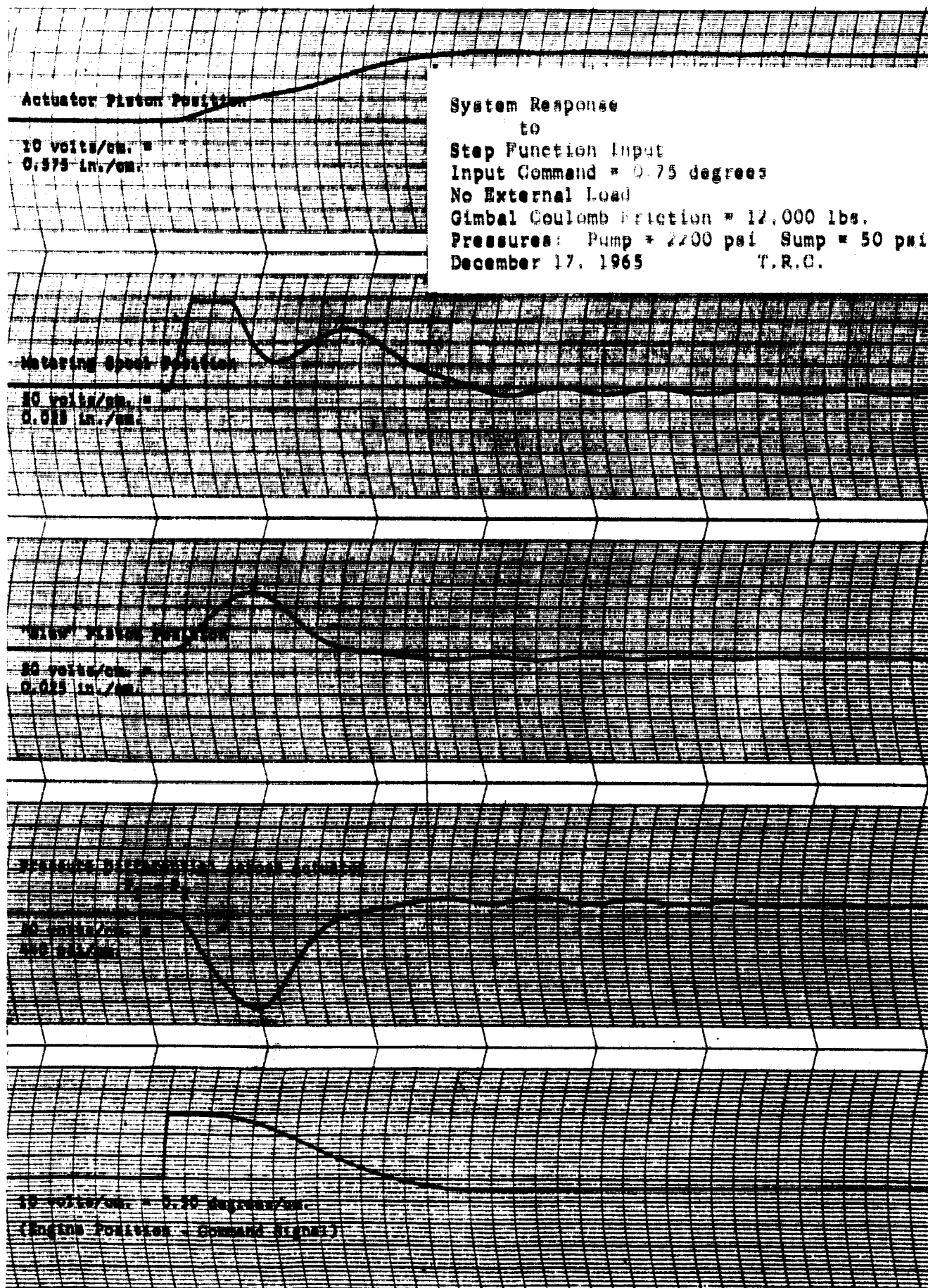


Fig. 4.14. System Dynamic Behavior to Step Command of 0.75 Degree.

Actuator Piston Position

10 volts/cm =

0.575 in./cm

System Response

1.0

Step Function Response

Input Command = 1.0 Volts

No External Load

Gimbal Gearbox Friction = 1.0 lb-in.

Pressures: Pump = 2200 psi, Stand = 50 psi

January 5, 1966

T.R.G.

Metering Spool Position

50 volts/cm =

0.025 in./cm

"Slew" Piston Position

50 volts/cm =

0.025 in./cm

Pressure Differential Across Actuator $P_1 - P_2$

20 volts/cm =

440 psi/cm

10 volts/cm = 0.5 degrees/cm

(Engine Position - Command Signal)

Fig. 4.15. System Dynamic Behavior to Step Command of 1.0 Degree.

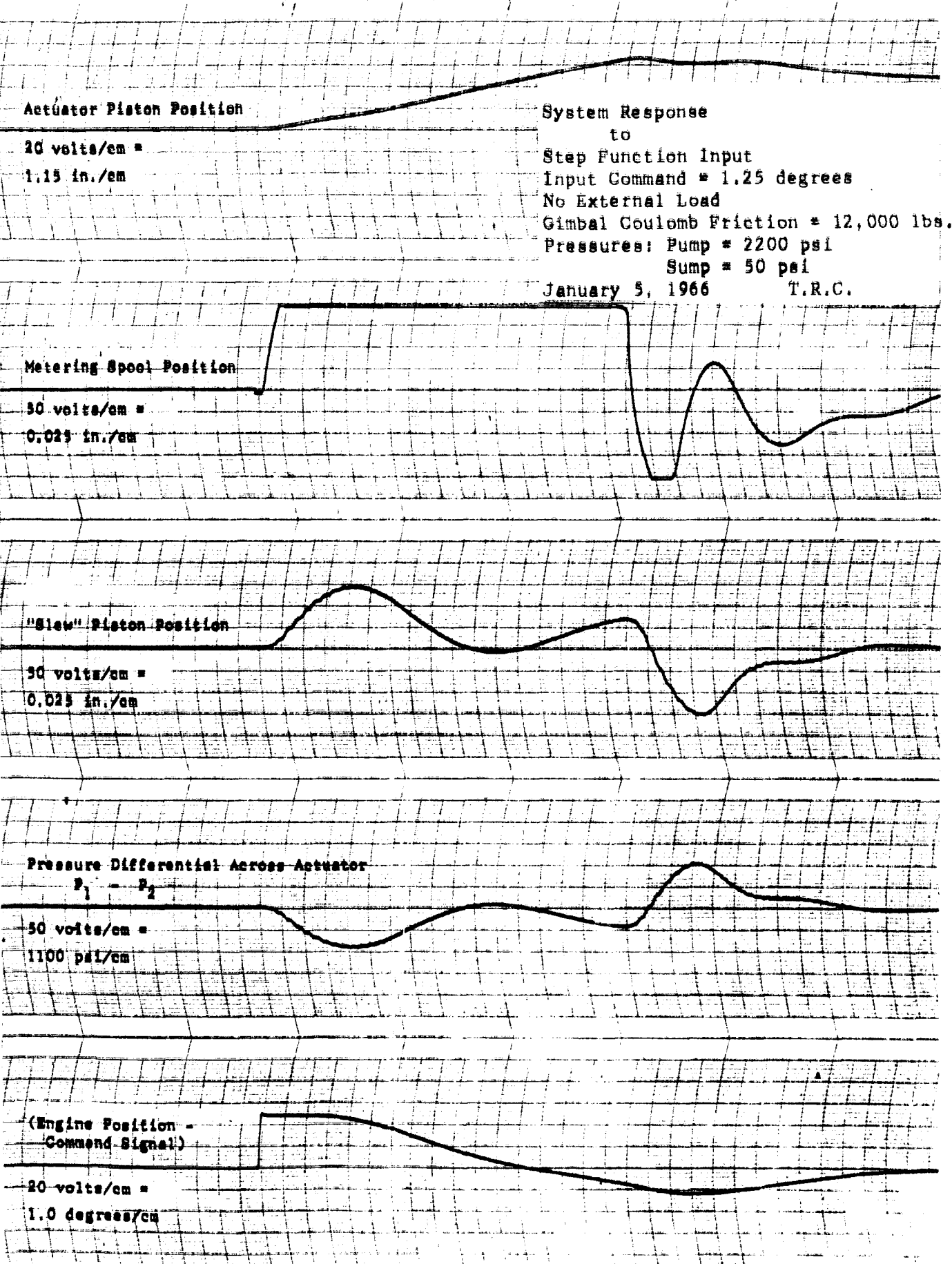


Fig. 4.16. System Dynamic Behavior to Step Command of 1.25 Degrees.

Actuator Piston Position:

20 volts/cm. =
1.15 in./cm.

System Response

to

Step Function Input

Input Command = 1.5 degrees

No External Load

Gimbal Coulomb Friction = 12,000 lbs.

Pressures: Pump = 2200 psi Sump = 50 psi

December 16, 1965

T.R.C.

Metering Spool Position:

50 volts/cm. =
0.025 in./cm.

"Slew" Piston Position:

50 volts/cm. =
0.025 in./cm.

Pressure Differential Across Actuator

$P_1 - P_2$
20 volts/cm. =
440 psi/cm.

20 volts/cm. = 1.0 degrees/cm.
(Engine Position + Command Signal)

Fig. 4.17. System Dynamic Behavior to Step Command of 1.5 Degrees.

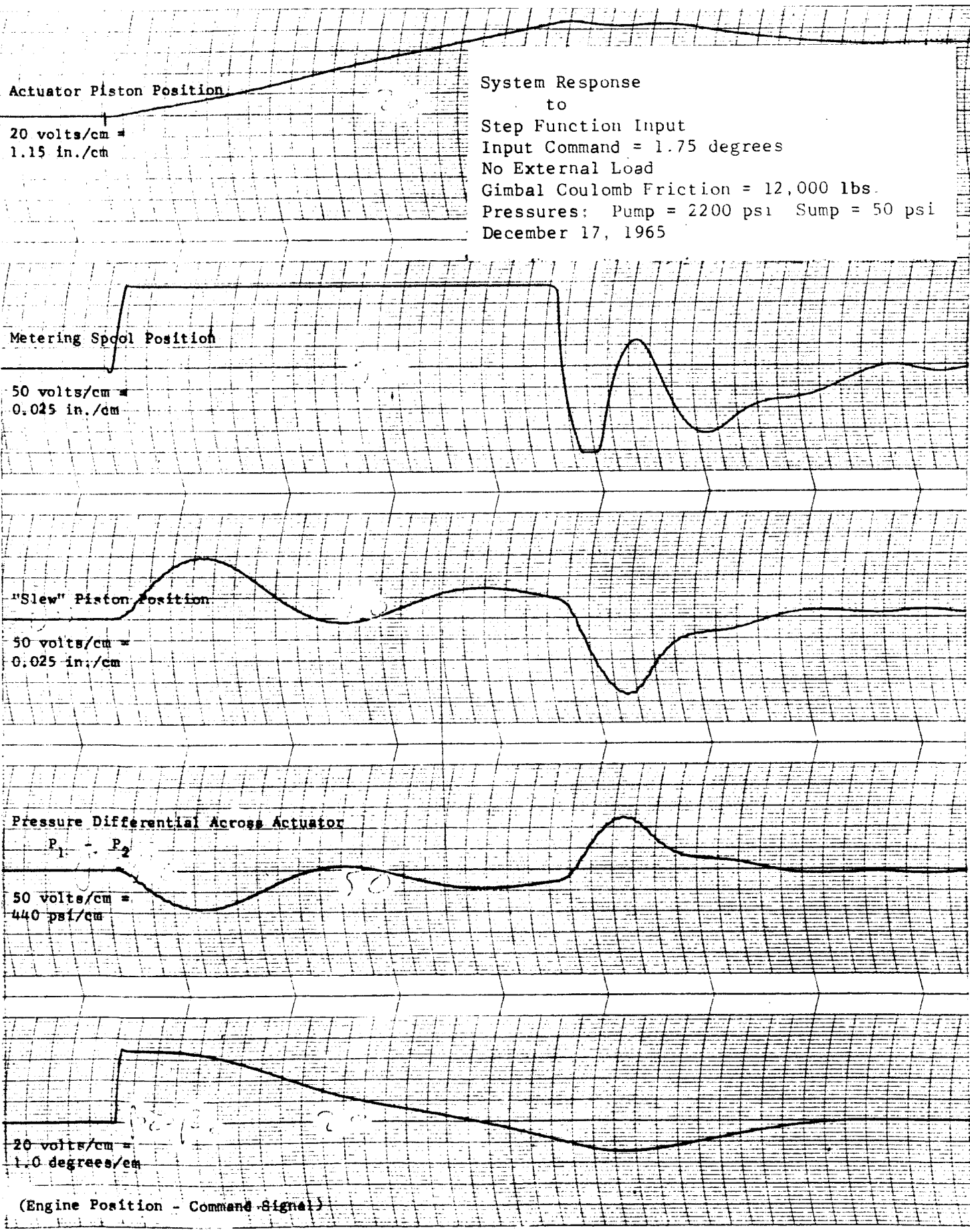


Fig. 4.18. System Dynamic Behavior to Step Command of 1.75 Degrees

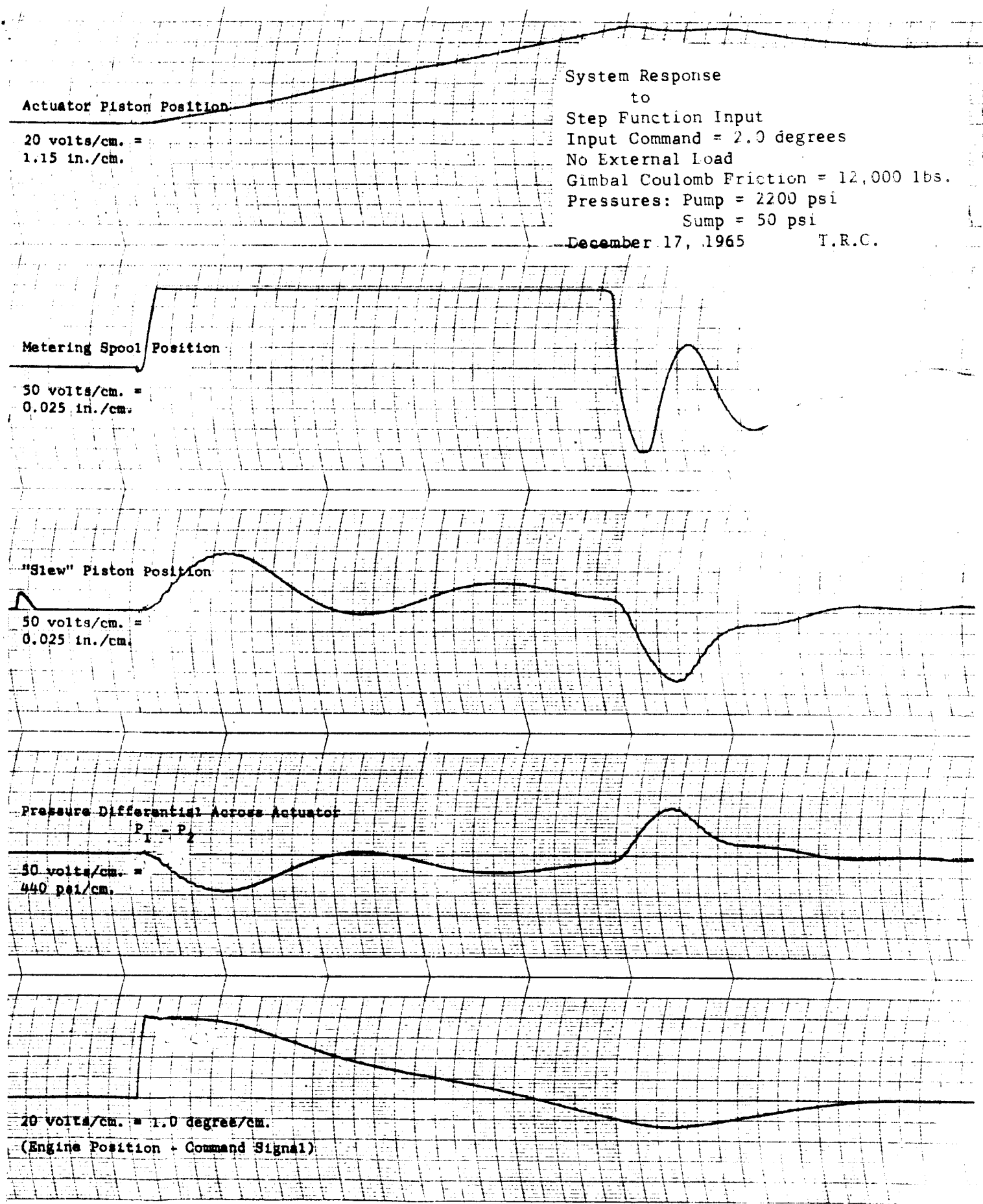


Fig. 4.19. System Dynamic Behavior to Step Command of 2.0 Degrees.

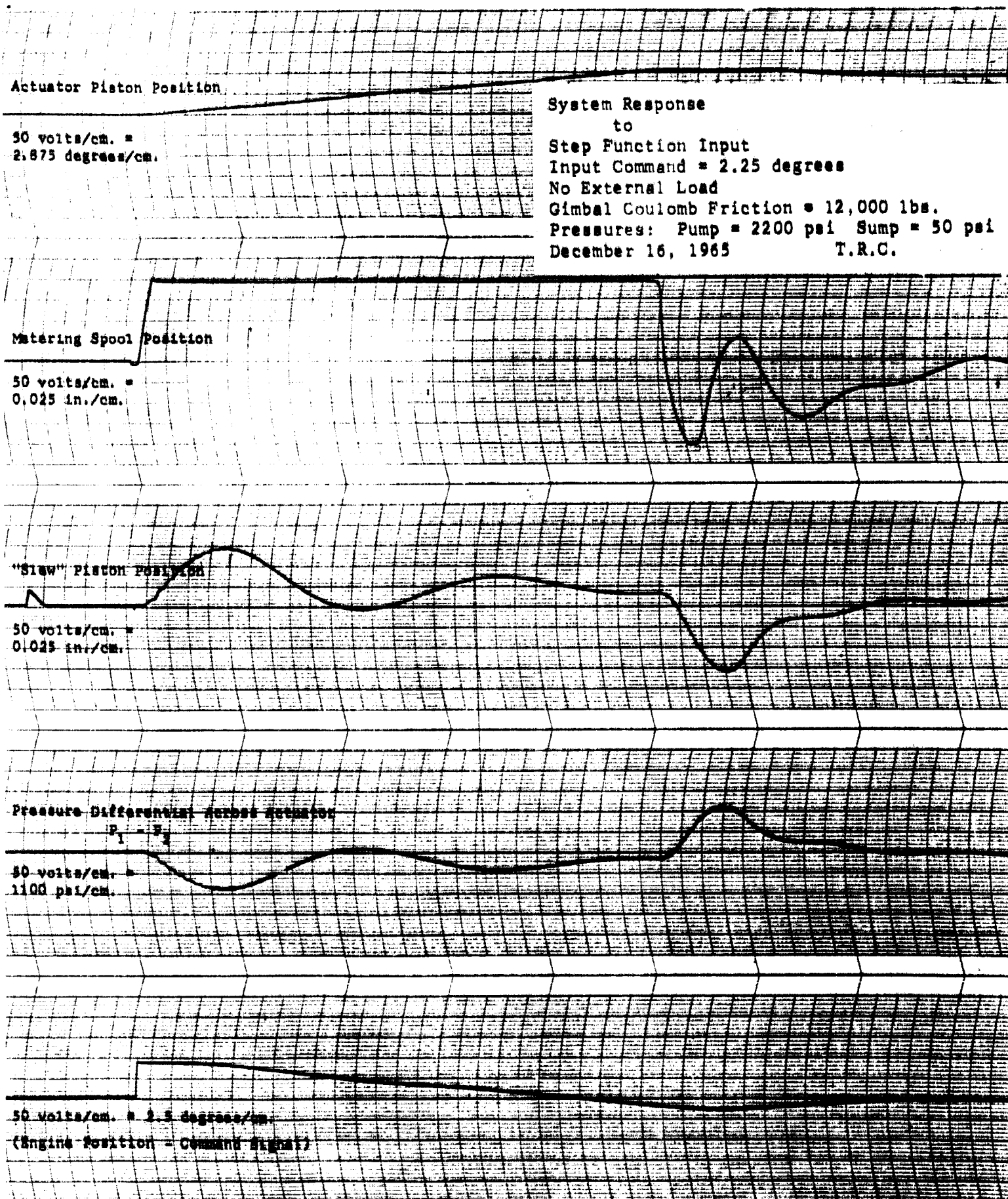


Fig. 4.20. System Dynamic Behavior to Step Command of 2.25 Degrees.

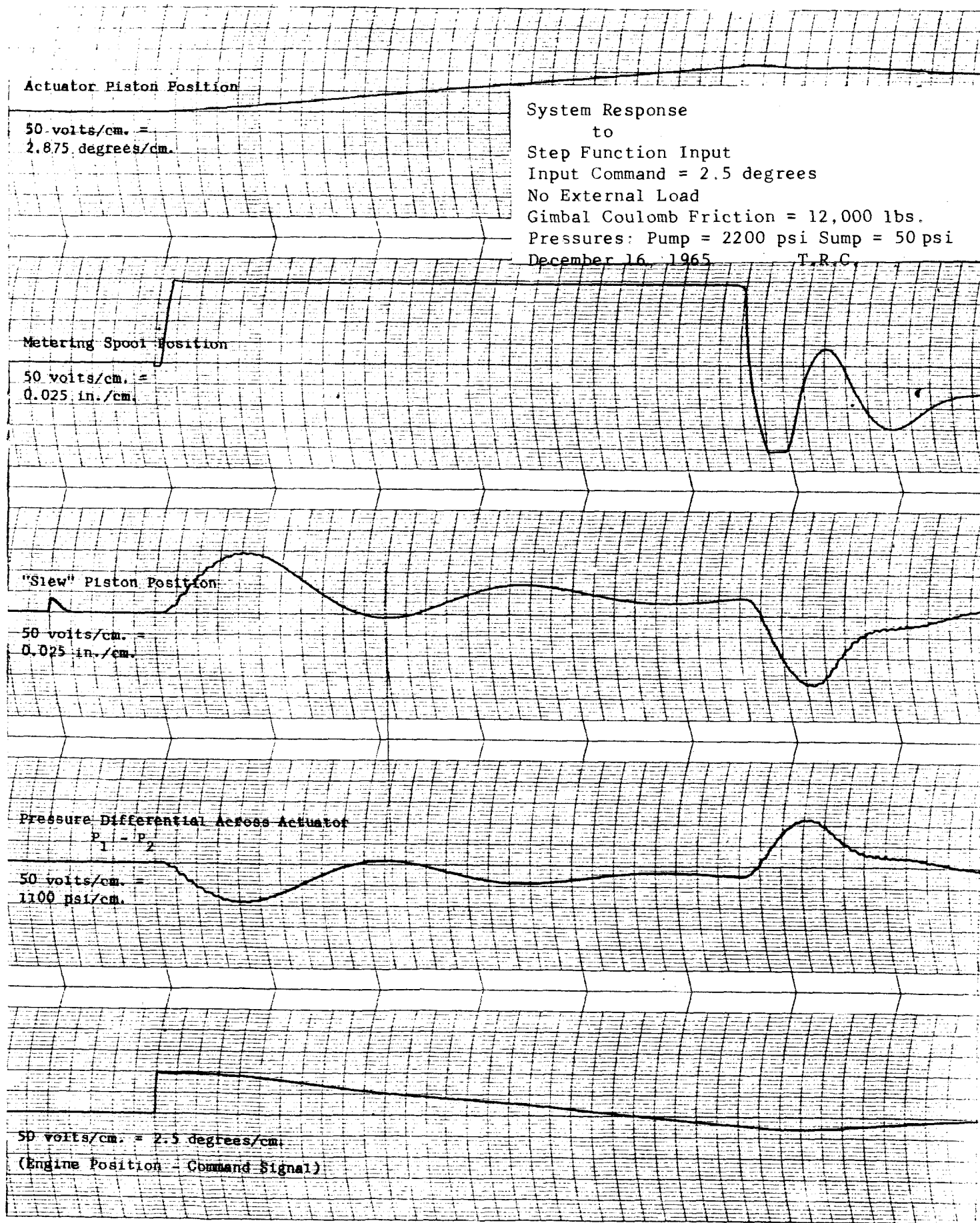


Fig. 4.21. System Dynamic Behavior to Step Command of 2.5 Degrees.

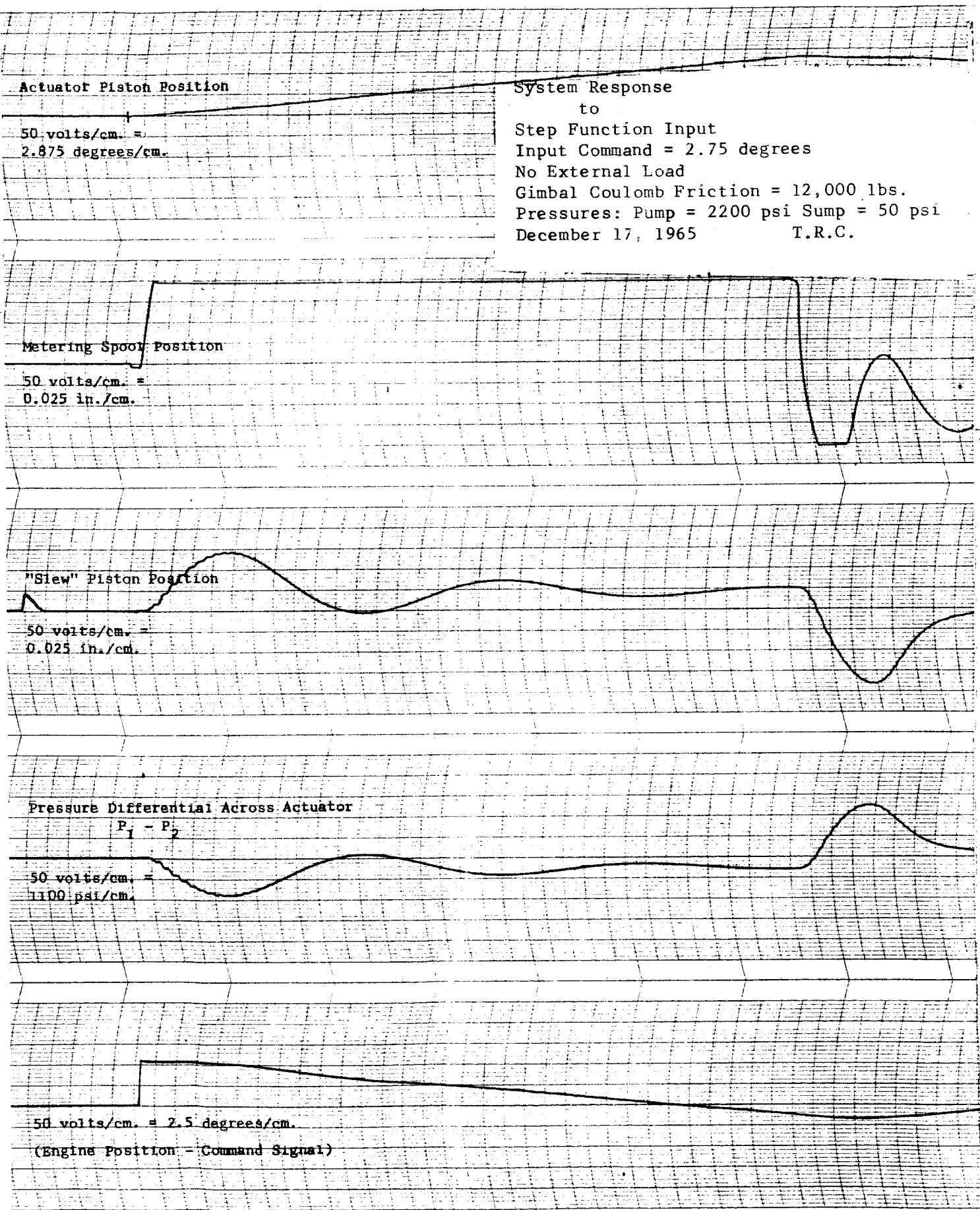


Fig. 4.22. System Dynamic Behavior to Step Command of 2.75 Degrees.

independent of which feedback-loop gain was adjusted. The conclusion reached was that a combination of the feedback signals coupled with the nonlinearities give rise to a threshold effect not uncommon to nonlinear systems. If one considers a boundary to exist between the two modes of operation, a change in any one variable or combination of variables may move the system performance across the boundary without any one variable being the sole controlling factor.

In light of the change of the system behavior detailed above, another look at the sinusoidal response was deemed desirable even though no unusual phenomena were evident in previous test.¹¹ It was further thought desirable to obtain strip chart recordings for visual analysis rather than the simpler technique (applicable at the low frequencies under consideration) of using meter values to determine system gains. The strip chart recordings would also make possible phase measurements with relative ease. The recordings shown in Figure 4.23 are typical of those obtained in these tests. Indicated on the recordings are the calculations that had to be made for each datum point as well as the procedure for obtaining the desired values of the input and output variables. This same technique of obtaining the gain and phase was used for all waveforms even in the case of those transients where the output, although periodic, was distorted due to system nonlinearities. No attempt was made to extract harmonic information.

The gain and phase information for sinusoidal input signals covering the range of 0.5 degree peak to peak to 1.0 degree peak-to-peak are presented in Figure 4.24 through 4.34. Note that a resonance condition exists in the neighborhood of three to four cycles per second. At a command of 0.8 degree peak-to-peak, the gain associated with this

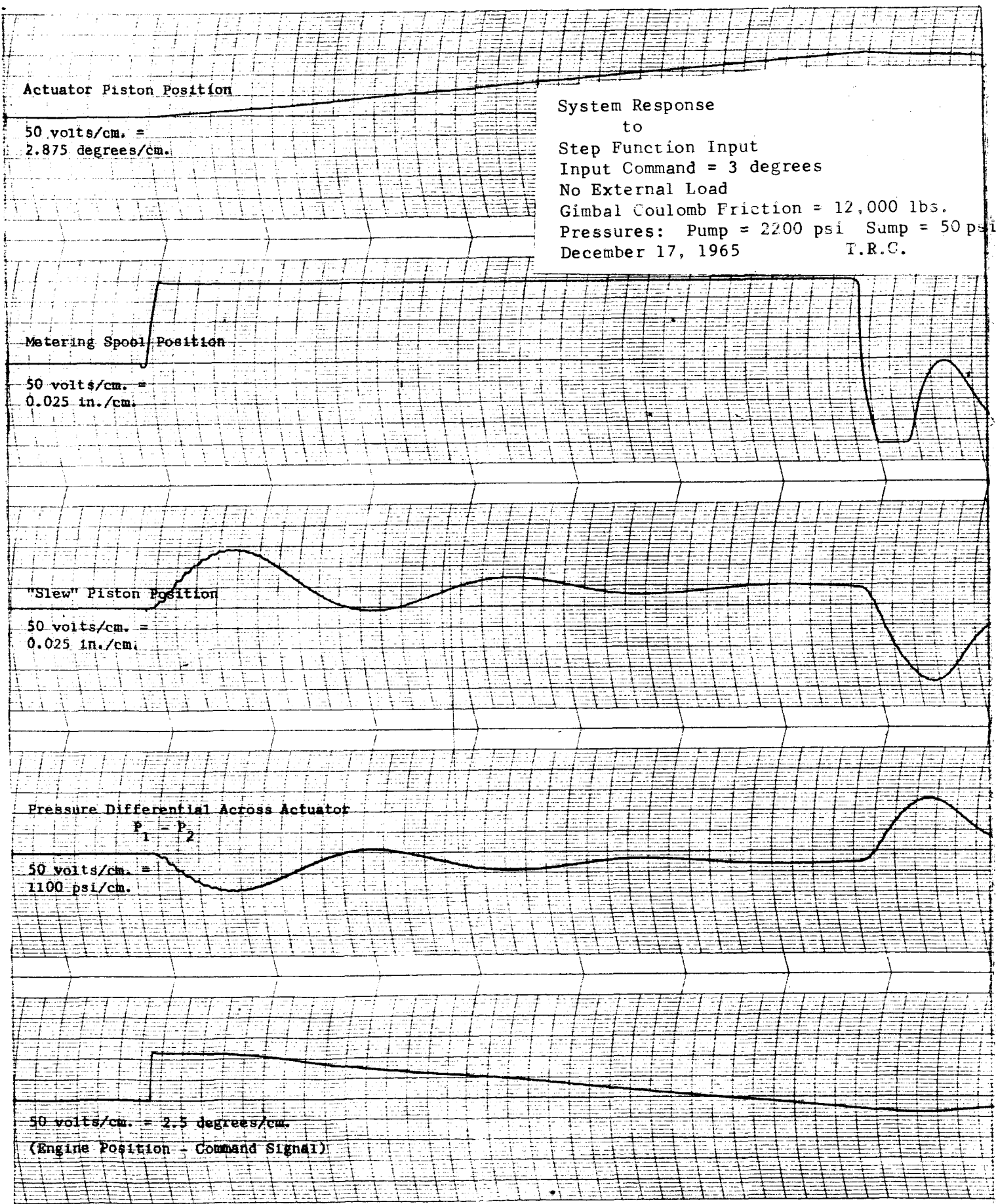


Fig. 4.23. System Dynamic Behavior to Step Command of 3 Degrees.

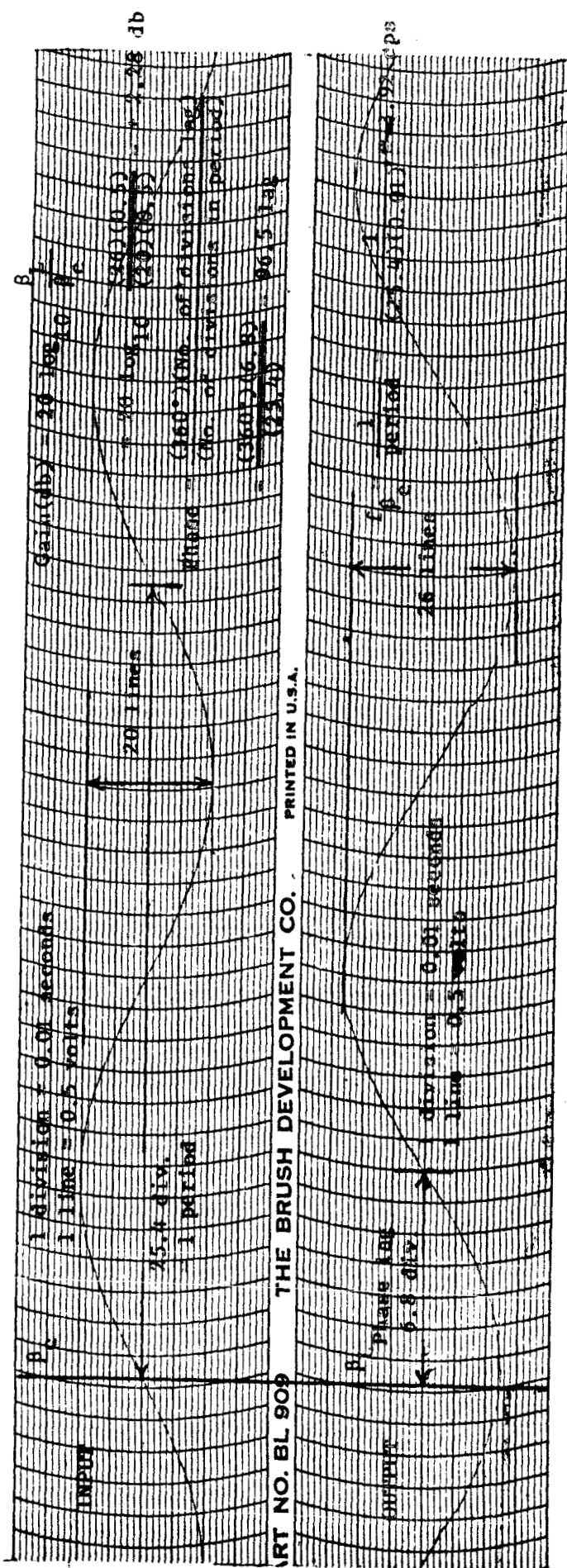
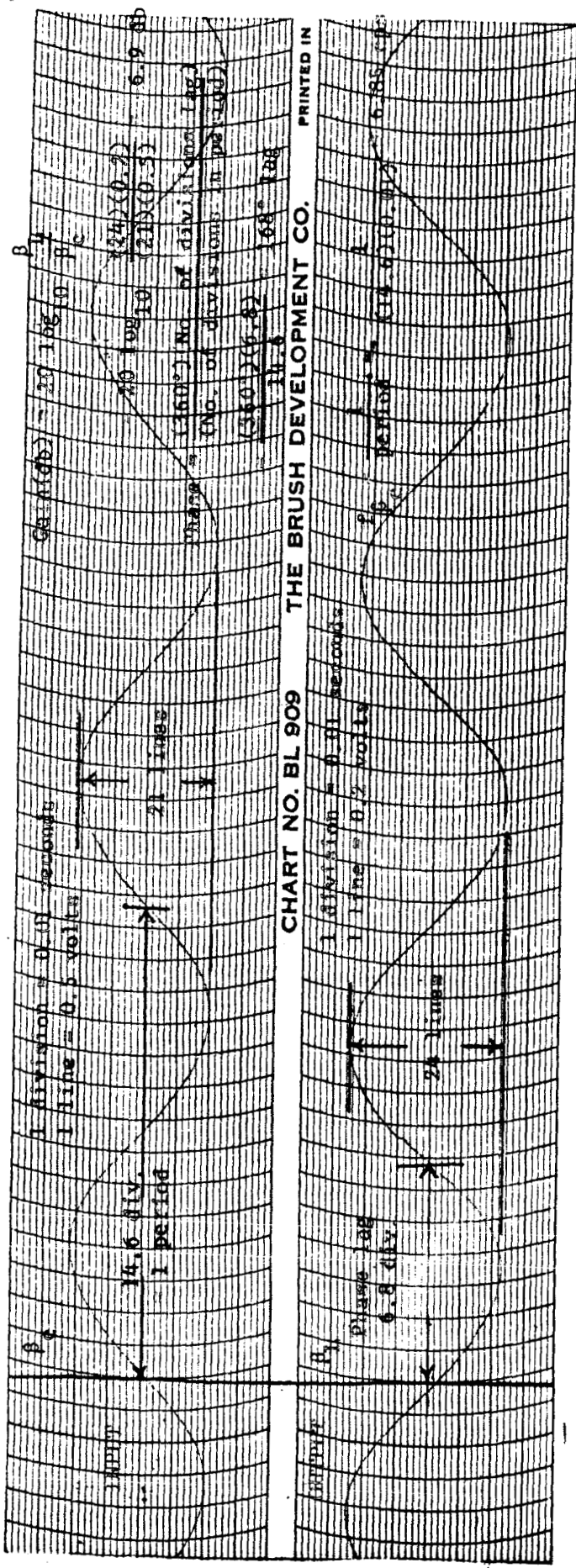
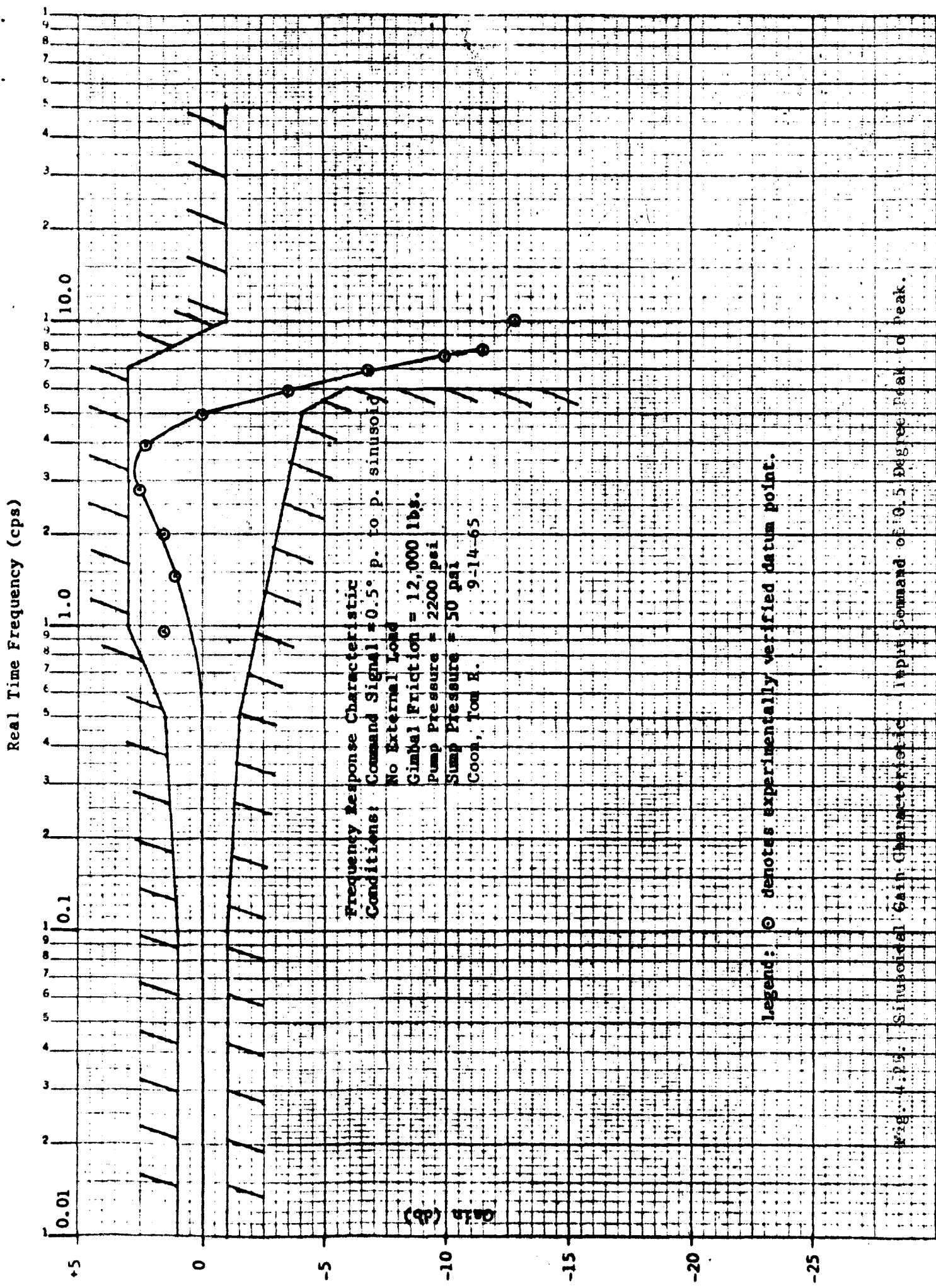
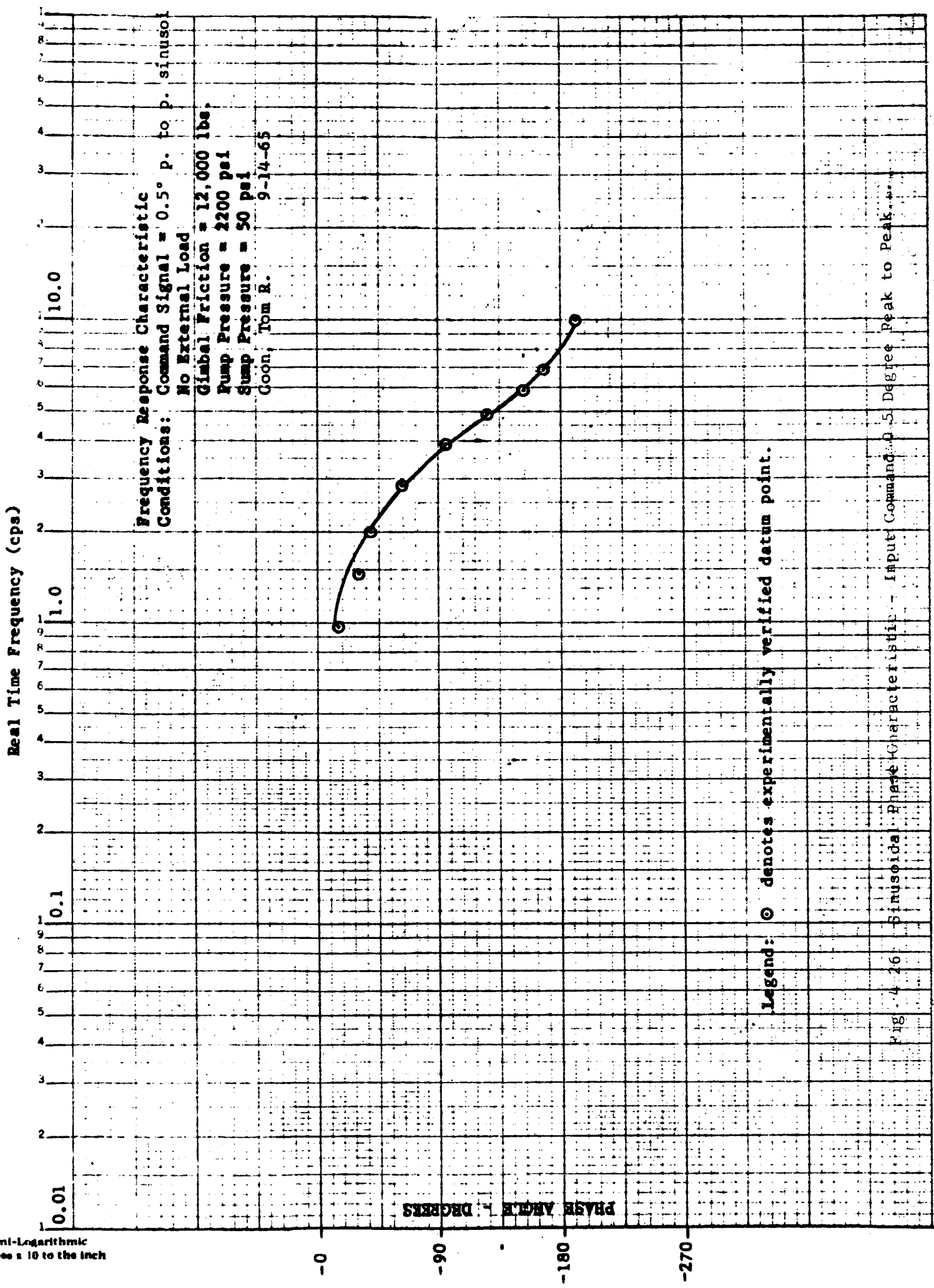
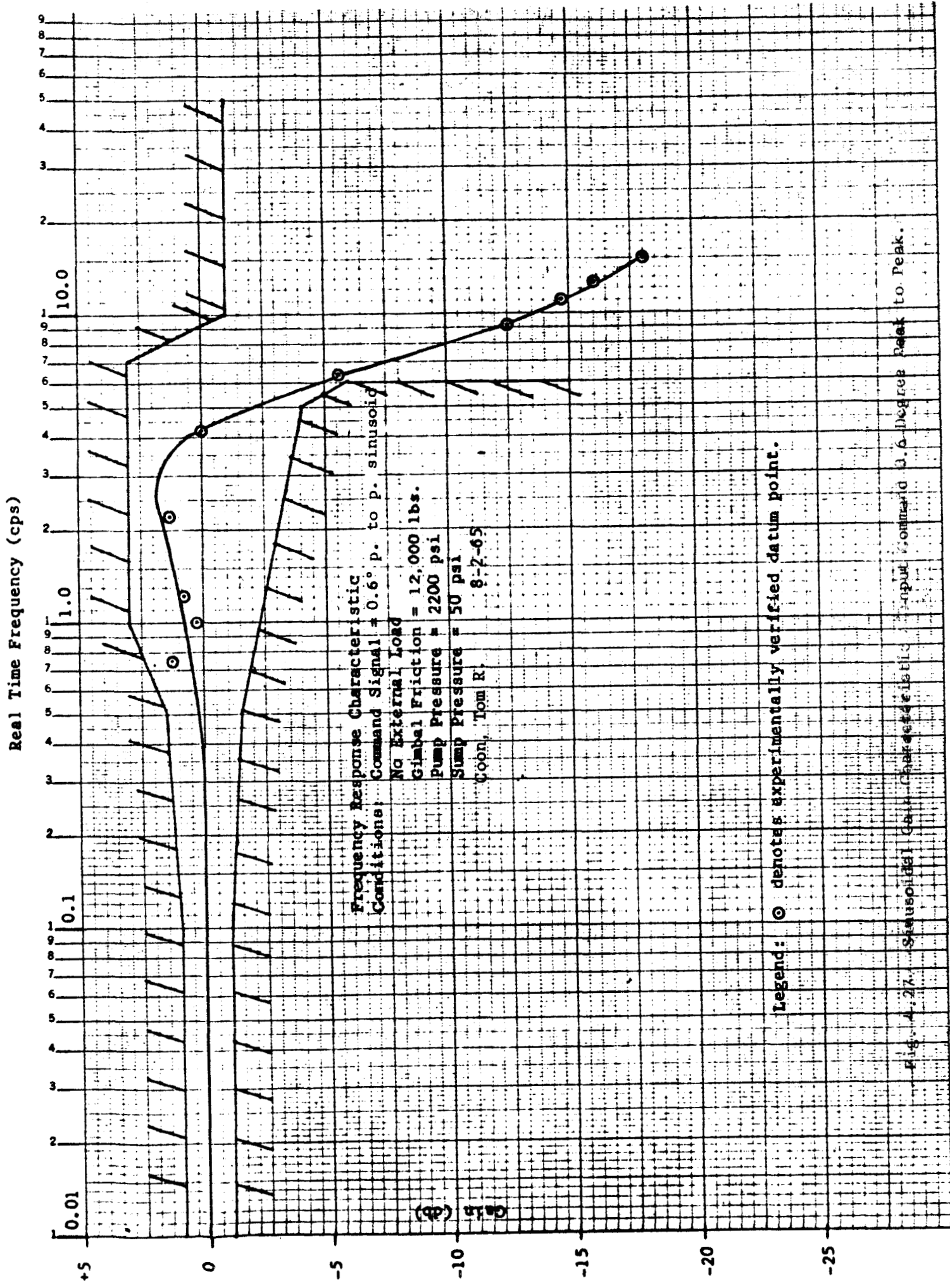


Fig. 4.24. Strip Chart Recordings for Sinusoidal Input Command Signals.







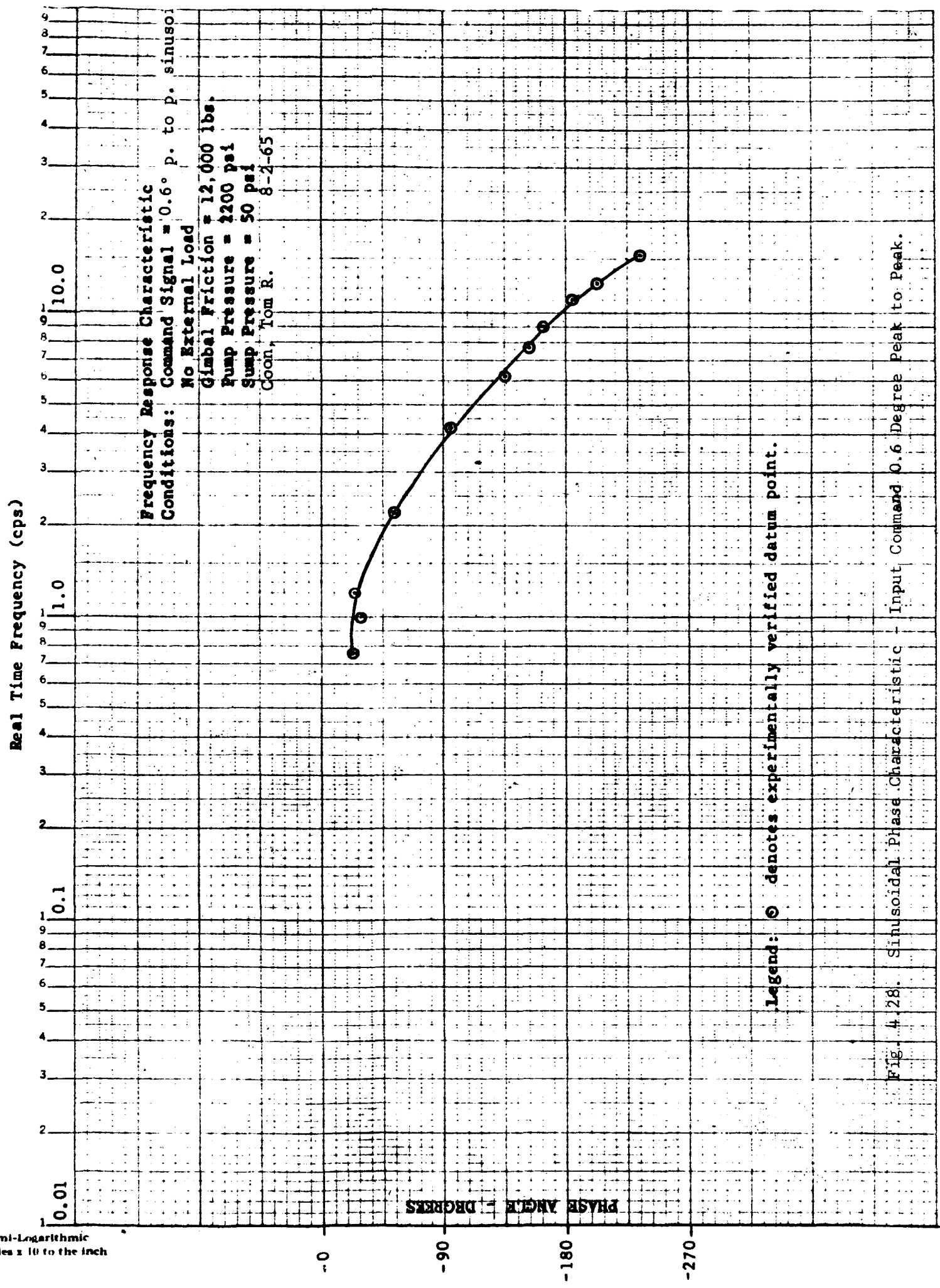
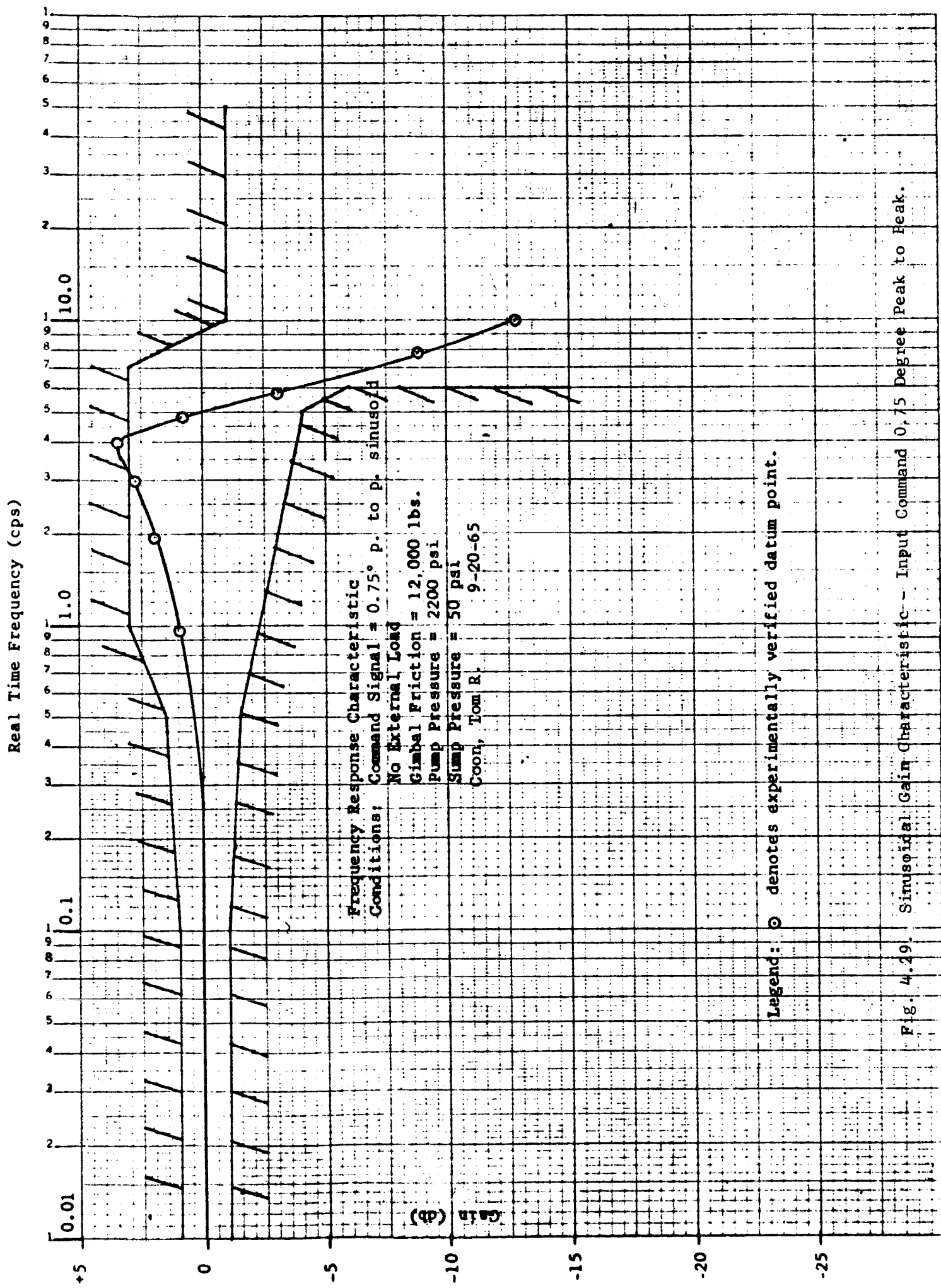
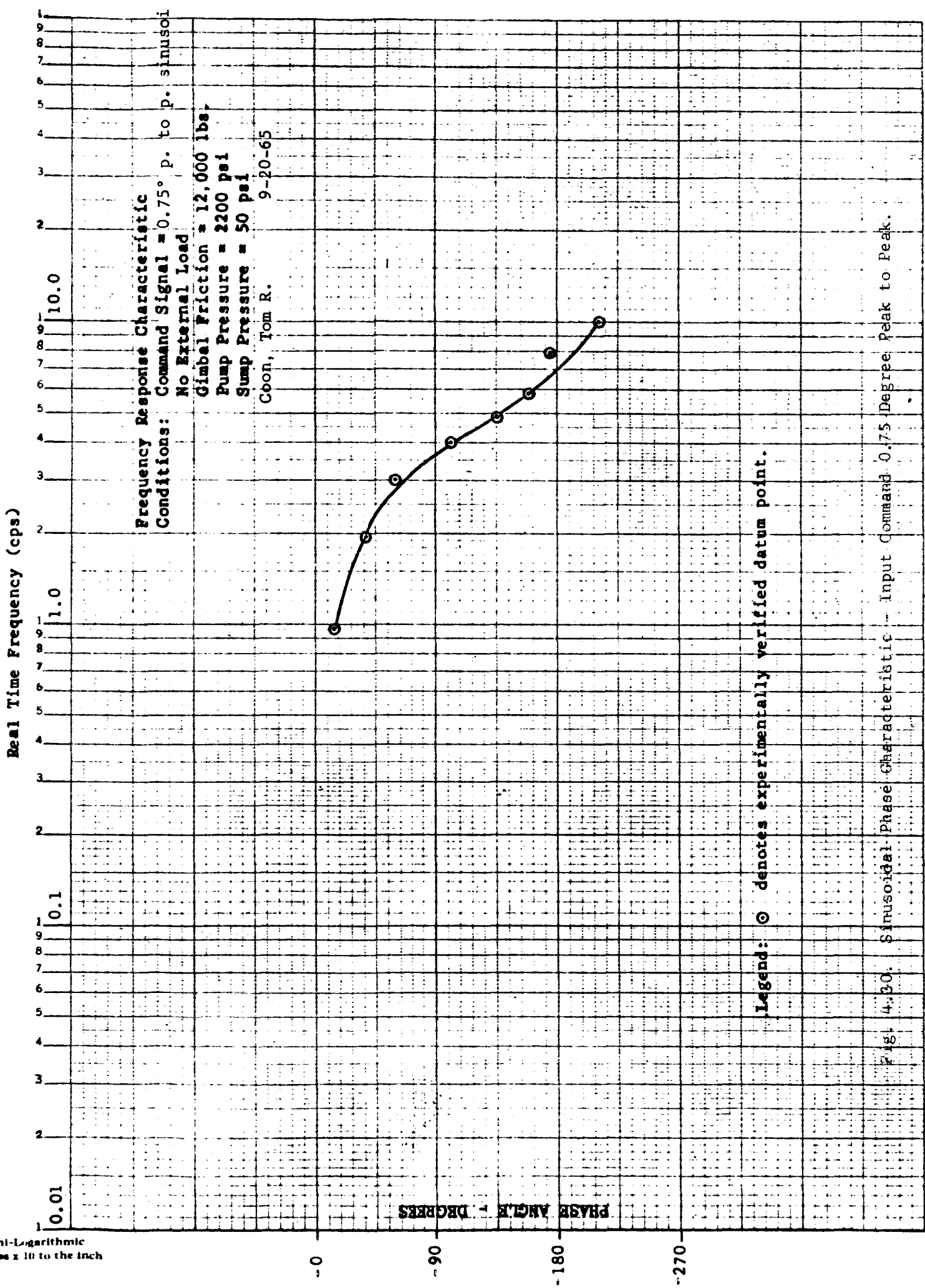
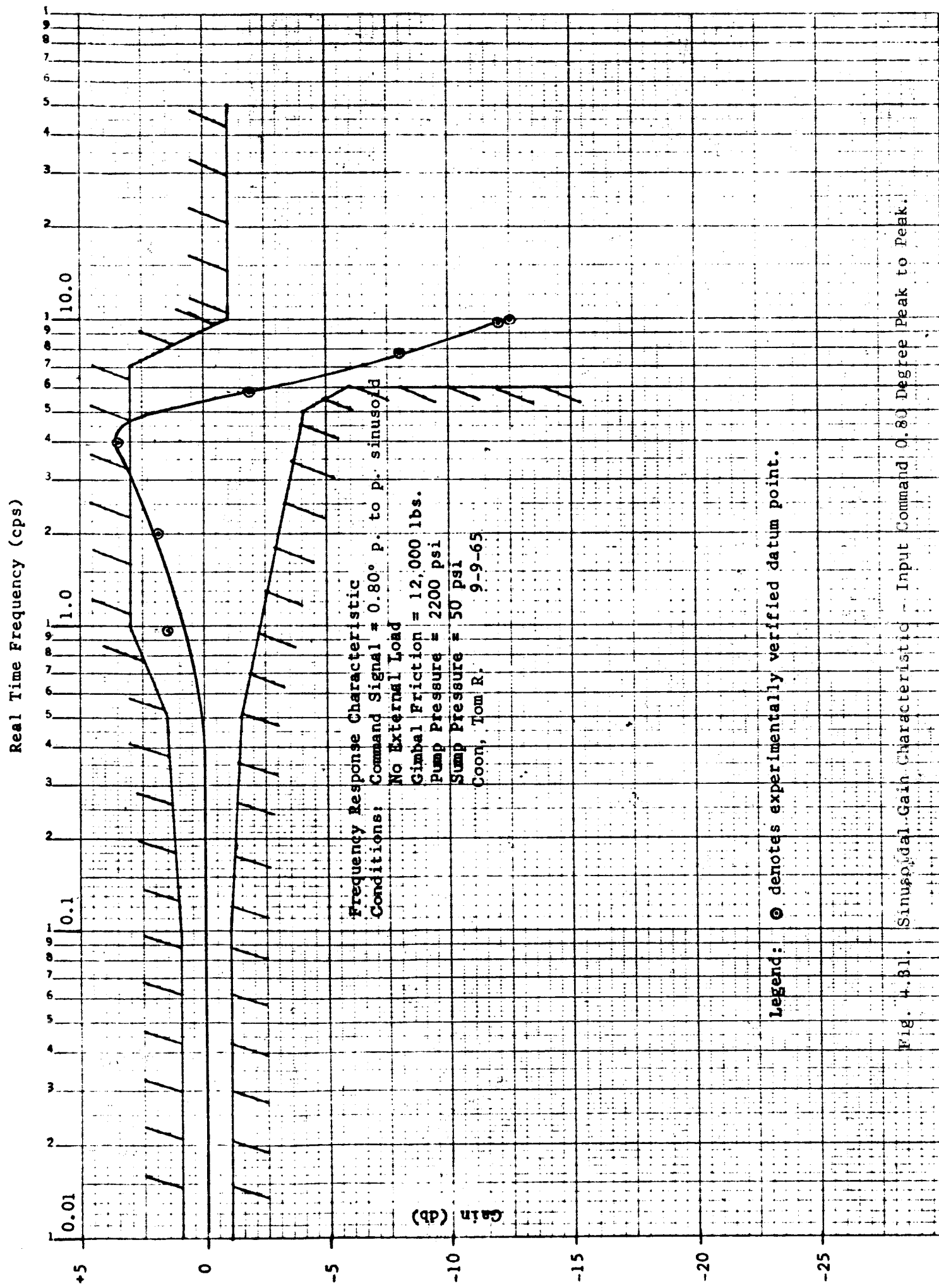
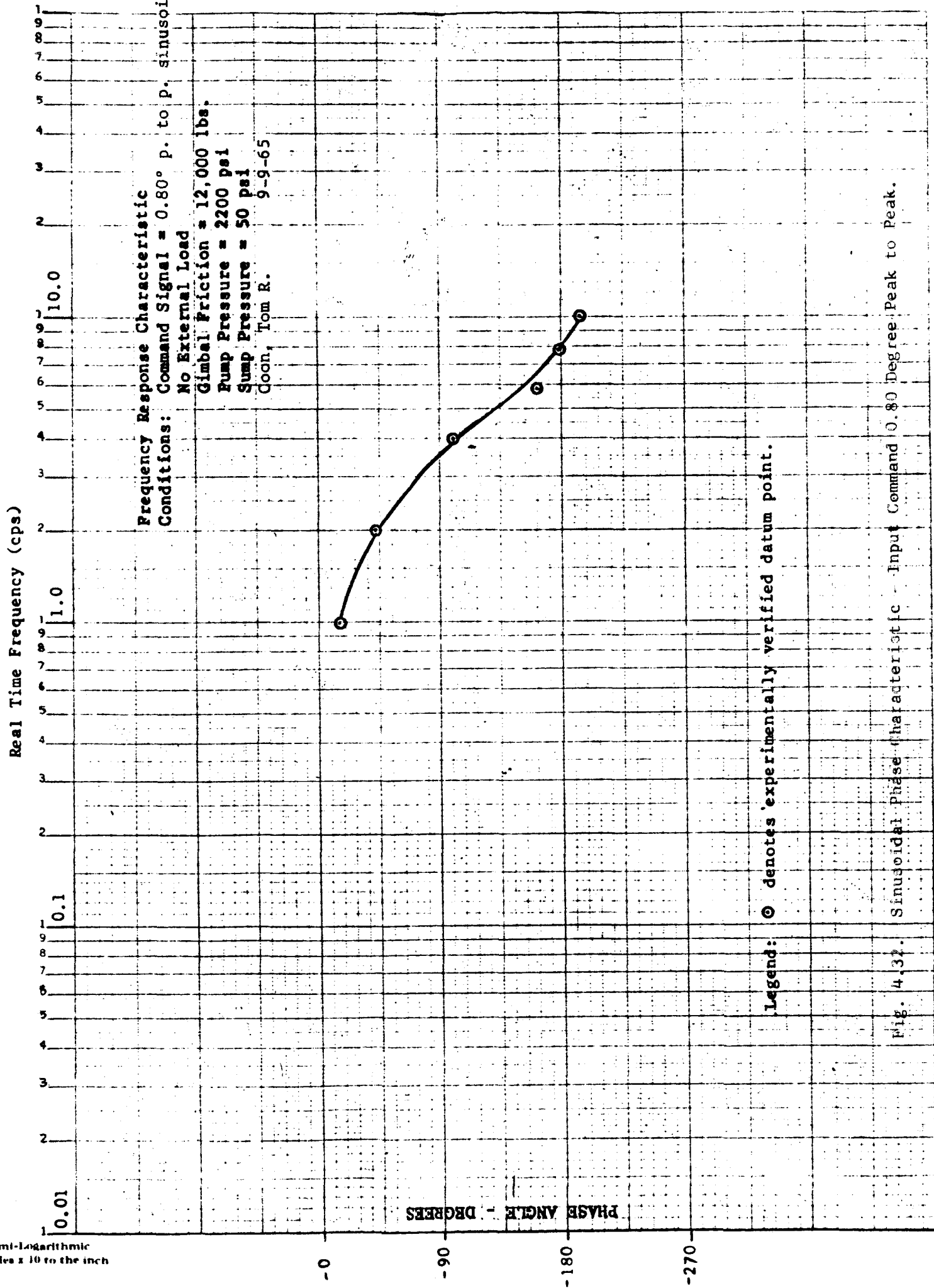


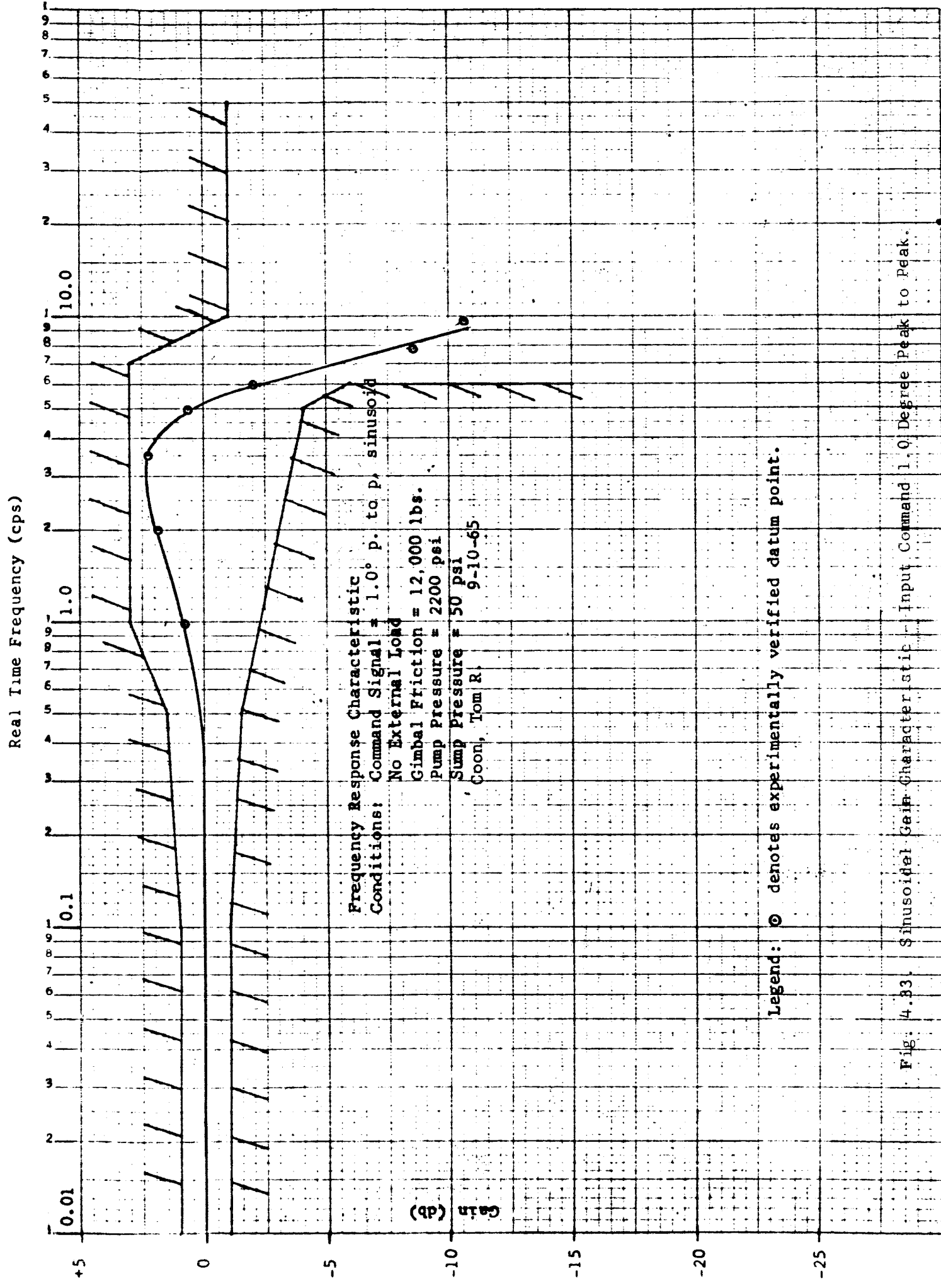
Fig. 4-28. Sinusoidal Phase Characteristic - Input Command 0.6 Degree Peak to Peak.











Real Time Frequency (cps)

10
9
8
7
6
5
4
3
2
1
0.1
0.01

Frequency Response Characteristic

Conditions: Command Signal = 1.0° P. to P. sinusoidal
No External Load
Gimbal Friction = 12,000 lbs.
Pump Pressure = 2200 psi
Susp Pressure = 50 psi
Coon, Tom R.
9-10-65

PHASE ANGLE - DEGREES

0

-90

-180

-270

Legend: ○ denotes experimentally verified datum point.

Sinusoidal Phase characteristic - Input Command 1.0 Degree Peak to Peak.

resonance condition is sufficient to cause the response to fall outside the specified limits. The phase characteristics do not show any marked change in the neighborhood of four cycles per second.

In view of the unusual behavior of the system, it was felt highly unfeasible to increase the sophistication of the model without any collaboration from experimental data as to the sufficiency and accuracy of the model used. Since no such experimental data was ever made available to the investigators, no additional studys using the analog model were attempted.

HIGH PRESSURE SURGE GENERATION

This phase of the study was made in order to try to determine if significant forces could be generated by the movement of one of the servo-actuators, transmitted through the mechanical linkages to the other servo-actuator and thereby create a pressure surge of sufficient magnitude to cause structural failure of hydraulic components.

In this analysis, certain simplifying assumptions were made. These assumptions were always made such that the effect would be worst-case conditions. A point mass was assumed for the engine system and the equation of motion for this mass was derived. The exact expression for the vector distance from the gimbal point of the engine to the point mass of the engine was derived and reported in Quarterly report No. 7 NAS8-11341.¹⁴ A solution for the derived equation of motion of the equivalent point mass of the engine as a function of time was attempted. The complexity of the equation obtained by using this approach became unwieldy for hand computation and another approach was sought.

Since the length from the point mass to the gimbal point is assumed to remain fixed, motion of the point mass about the gimbal point describes a sphere. In like manner the motion of the point mass about the fixed

length servoactuator vehicle tie-point also describes a sphere. The intersection of these two spheres result in a circle which is the trajectory of the motion of the point mass. The engineering data used to establish coordinate systems were obtained from Figure 2-15A in Section II of report R-3896-1¹⁵ and from the drawing of the F-1 Engine Simulation Stand prepared by Brown Engineering Company and dated 6-27-65.¹⁶

The first coordinate transformation was made to orient the coordinate system such that the plane containing the circular trajectory is parallel to one of the planes formed by two of the coordinate axis. The second coordinate transformation was made to translate the origin of the coordinate system to the neutral position of the point mass. The different coordinate systems and identification of nomenclature are given in Figure 5-1.

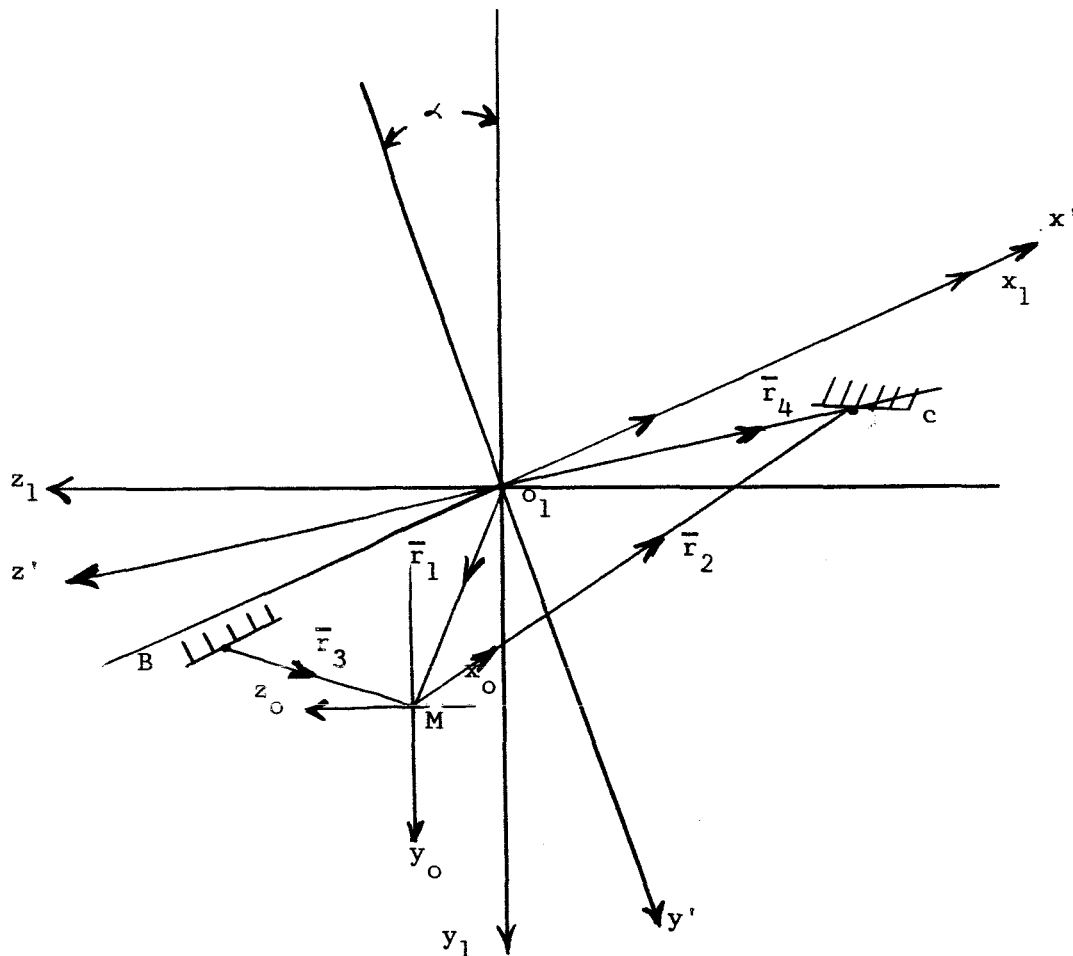


Figure 5-1 - Location of Equivalent Point Mass of the Engine with Respect to Three Cartesian Coordinate Systems.

Where:

- (1) O_1 - the gimbal point of the engine.
- (2) M - the equivalent point mass of the engine.
- (3) C - the fixed point in the y_1 , z_1 plane to which actuator No. 2 is attached.
- (4) B - the fixed point in the x_1 , y_1 plane to which actuator No. 1 is attached.
- (5) the x_1 , y_1 , z_1 coordinate system corresponds to the x' , y , z'_g coordinate system in Figure 2-15A from R-3896-1 Report, Section II.
- (6) \bar{r}_1 - the magnitude $|\bar{r}_1|$ is the length of the vector from the gimbal point of the engine to the point mass of the engine.
- (7) \bar{r}_2 - the magnitude $|\bar{r}_2|$ is the fixed length from the No. 2 servoactuator vehicle tie-point to the point mass of the engine.
- (8) \bar{r}_3 - the magnitude $|\bar{r}_3|$ is the variable length from the No. 1 servoactuator vehicle tie-point to the point mass of the engine.
- (9) \bar{r}_4 - the magnitude $|\bar{r}_4|$ is the length of the vector from the gimbal point to the vehicle tie-point of servoactuator No. 2.
- (10) α - angle through which x_1 , y_1 , z_1 coordinate system is rotated about the x_1 axis to establish the x' , y , z' coordinate system. ($\alpha = \text{constant} = 8^\circ$)

The first coordinate transformation which is from the x_1 , y_1 , z_1 system to the x' , y , z' system is accomplished by rotating the x_1 , y_1 , z_1 system about the x axis until the z' axis (corresponds to the z_1 axis before rotation) passes through the vehicle tie-point of servoactuator No. 2. This will give the geometric relationships shown in Figure 5-2. The transformation is accomplished as follows:

$$\begin{bmatrix} x' \\ y' \\ z' \end{bmatrix} = \begin{bmatrix} 1 & 0 & 0 \\ 0 & \cos \alpha & -\sin \alpha \\ 0 & \sin \alpha & \cos \alpha \end{bmatrix} \begin{bmatrix} x_1 \\ y_1 \\ z_1 \end{bmatrix} \quad \text{or} \quad \begin{bmatrix} x_1 \\ y_1 \\ z_1 \end{bmatrix} = \begin{bmatrix} 1 & 0 & 0 \\ 0 & \cos \alpha & \sin \alpha \\ 0 & -\sin \alpha & \cos \alpha \end{bmatrix} \begin{bmatrix} x' \\ y' \\ z' \end{bmatrix}$$

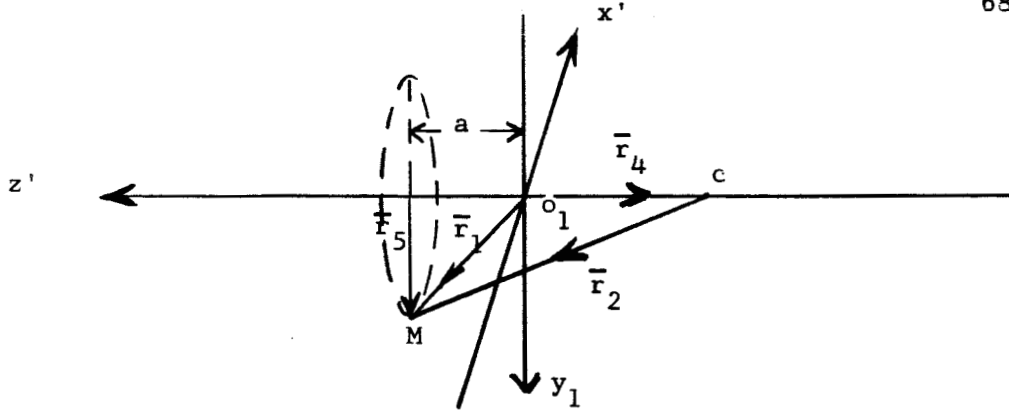


Figure 5-2 - Path Described by Equivalent Point Mass of Engine in x' , y' , z' Coordinate System.

The second transformation, between x_1 , y_1 , z_1 system to the x_o , y_o , z_o system, is one of linear displacement. The coordinate relationships are

$$x_1 = x_o \cdot k_1$$

$$k_1 = 12.8$$

$$y_1 = y_o + k_2$$

$$\text{and} \quad k_2 = 52.8$$

$$z_1 = z_o + k_3$$

$$k_3 = 12.7$$

With respect to the x' , y' , z' coordinate system the path described by the point mass (M) of the engine, with the constraints that \bar{r}_1 and \bar{r}_2 , = constant, is a circle parallel to the x' , y' plane. The center of the circle is displaced a constant distance, "a" on the z' axis.

At $z' = a$ the equation of the circle is:

$$x'^2 + y'^2 = |\bar{r}_5|^2$$

Redrawing Figure 5-2 in a manner more conducive to analysis by angular coordinates results in Figure 5-3.

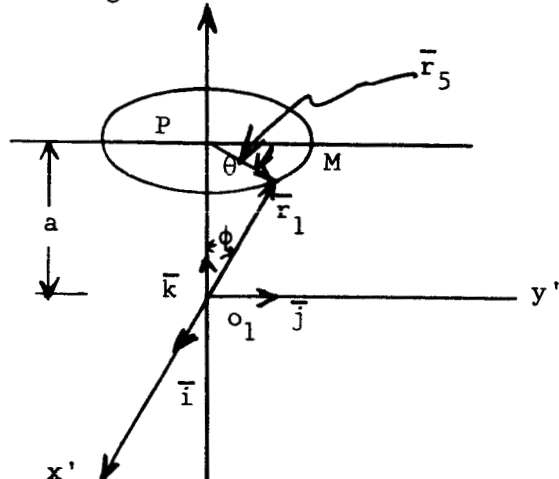


Figure 5-3: - Path Described by Equivalent Point Mass in x' , y' , z' Coordinate System.

A given extension in actuator No. 1 will cause a displacement of the point mass in the +θ direction as shown in Figure 5-4.

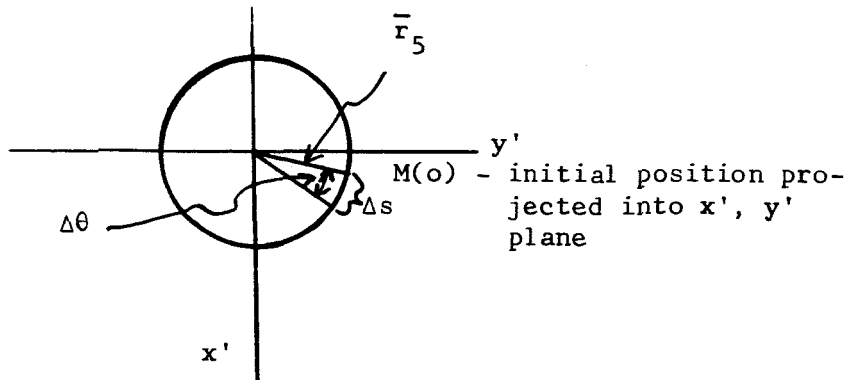


Figure 5-4 - Projected Path in x' , y' Plane.

From Figure 5-4:

$$\Delta s = \left| \bar{r}_5 \right| \Delta\theta = \left(\left| \bar{r}_1 \right| \sin \phi \right) \Delta\theta \quad (5-1)$$

The tangential speed of point M is:

$$v = \frac{ds}{dt} = \left| \bar{r}_1 \right| \theta \sin \phi \quad (5-2)$$

Where θ = angular speed of the point M

Using vector notation¹⁷, the angular velocity is given by

$$\bar{\omega} = -\dot{\theta} \bar{k}, \quad (5-3)$$

and the velocity of the point M is

$$\bar{v} = \frac{d\bar{r}_1}{dt} = \bar{\omega} \times \bar{r}_1 \quad (5-4)$$

The acceleration of point M is

$$\bar{a} = \frac{d\bar{v}}{dt} = \frac{d}{dt} (\bar{\omega} \times \bar{r}_1) = \frac{d\bar{\omega}}{dt} \times \bar{r}_1 + \bar{\omega} \times \frac{d\bar{r}_1}{dt} \quad . \quad (5-5)$$

Rewriting Equation (5-5):

$$\bar{a} = \bar{\omega} \times \bar{r}_1 + \bar{\omega} \times (\bar{\omega} \times \bar{r}_1) \quad (5-6)$$

Where $\ddot{\alpha} = -\omega \ddot{k} = -\dot{\theta} \ddot{k} = \ddot{\theta} \ddot{k}$ = angular acceleration. Solving Equation (5-6) using the vector $\ddot{r}_1 = (x') \ddot{u}_x + \left[\sqrt{\ddot{r}_5^2 - (x')^2} \right] \ddot{u}_y + (a) \ddot{u}_z$, (See Reference 15) gives

$$\ddot{a} = I (\ddot{\theta} \sqrt{\ddot{r}_5^2 - x'^2} - \dot{\theta}^2 x') + j (\dot{\theta} x' + \ddot{\theta}^2 \sqrt{\ddot{r}_5^2 - x'^2}) \quad (5-7)$$

To determine $\dot{\theta}$, $\ddot{\theta}$ use equation (5-1).

$$\frac{d\theta}{dt} = \dot{\theta} = \frac{1}{|\ddot{r}_5|} \frac{ds}{dt} \quad (5-8)$$

$$\frac{d^2\theta}{dt^2} = \ddot{\theta} = \frac{1}{|\ddot{r}_5|} \frac{d^2s}{dt^2}$$

One can determine from Figure 5-3 that:

$$x' = |\ddot{r}_5| \sin \theta \quad (5-9)$$

For small angular displacements x' will be approximately:

$$x' \approx |\ddot{r}_5| \theta \quad (5-10)$$

The chord displacement (Δs) will be proportional to the displacement of actuator No. 1 ($\Delta \ell$) for small displacements, i.e.,

$$\Delta s \approx k \Delta \ell \quad (5-11)$$

The value of the constant of proportionality, k , can be determined to be approximately 1.54 as shown in Figure 5-5^{15,16} when the point mass is in the neutral position.

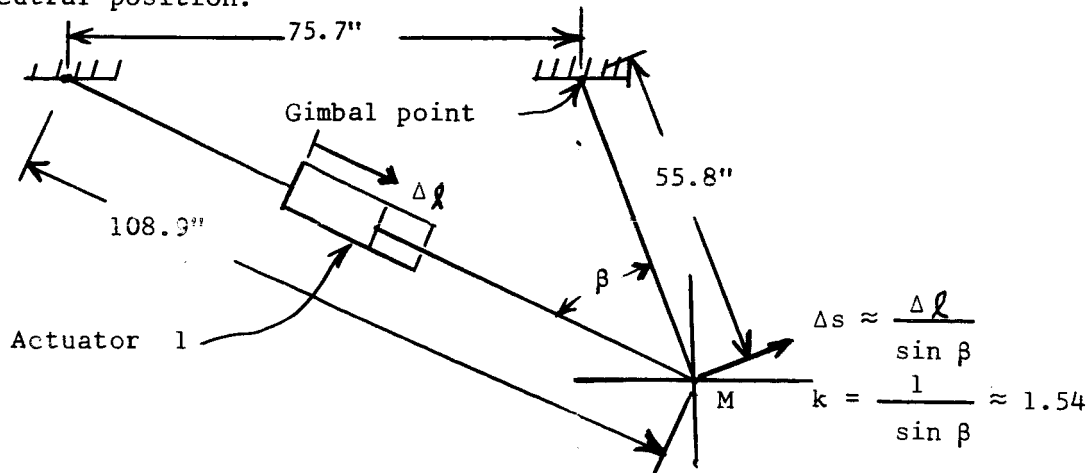


Figure 5-5 - Figure Used to Determine the Constant of Proportional k .

Substituting Equation (5-11) into Equation (5-8) yields:

$$\dot{\theta} = \frac{k}{|\bar{r}_5|} \frac{d\ell}{dt} \quad (5-12)$$

$$\ddot{\theta} = \frac{k}{|\bar{r}_5|} \frac{d^2\ell}{dt^2}$$

Where $\frac{d\ell}{dt}$ = linear velocity of the actuator and $\frac{d^2\ell}{dt^2}$ is the linear acceleration of the actuator. Using Equations (5-10) and (5-12), the acceleration vector (Equation 5-7) can now be written as

$$\bar{a} = \bar{i} \left(\frac{k}{|\bar{r}_5|} \frac{d^2\ell}{dt^2} |\bar{r}_5| \sqrt{1 - \theta^2} - (\dot{\theta})^2 |\bar{r}_5| \theta \right) - \bar{j} \left(\frac{k}{|\bar{r}_5|} \frac{d^2\ell}{dt^2} |\bar{r}_5| \theta + (\dot{\theta})^2 |\bar{r}_5| \sqrt{1 - \theta^2} \right)$$

and for the small angular displacements

$$\bar{a} \approx \bar{i} \left(k \frac{d^2\ell}{dt^2} - (\dot{\theta})^2 |\bar{r}_5| \theta \right) - \bar{j} \left(k \frac{d^2\ell}{dt^2} \theta + (\dot{\theta})^2 |\bar{r}_5| \right). \quad (5-13)$$

From Newton's Law as applied to the kinetics of particles:

$$\text{resultant force} = (\text{mass}) (\text{acceleration}) \quad (5-14)$$

It seems reasonable to assume that the maximum acceleration, therefore maximum force, occurs at the instant the actuating signal is applied and before the mass has been displaced any appreciable distance. Therefore θ and $\dot{\theta}$ are very small quantities. With this approximation, equation (5-14) can be written as:

$$\bar{F} \approx M \left[\bar{i} \left(k \frac{d^2\ell}{dt^2} \right) - \bar{j} \left(k \frac{d^2\ell}{dt^2} \theta \right) \right] \quad (5-15)$$

It now remains to find the component of force that is transmitted along the axis of the piston of servoactuator No. 2. Recalling that \bar{r}_2 is a vector directed from the vehicle tie-point of servoactuator No. 2 to the point mass, it would be more appropriate to use the line of action of a vector drawn from the vehicle tie-point of servoactuator No. 2 to the engine tie-point of servoactuator No. 2 as this gives the true axis of the

piston. Since the initial displacements are assumed to be small, the coordinates of this vector with the engine in the neutral position should suffice. Label this vector \bar{r}_6 . In the x_1, y_1, z_1 coordinate system it is given by^{15,16}

$$\bar{r}_6 = 54.4 \bar{\mu}_{y_1} + 25 \bar{\mu}_{z_1} \quad (5-16)$$

and by using the transformations

$$\bar{r}_6 = 50.3 \bar{j} + 32.3 \bar{k} \quad (5-17)$$

in the x', y', z' coordinate system.

The component of force given by Equation (5-15) that is transmitted along the axis of the piston of servoactuator No. 2 is

$$|F_2| = \frac{\bar{F} \cdot \bar{r}_6}{|\bar{r}_6|}. \quad (5-18)$$

Now

$$|\bar{r}_6| = 59.8"$$

therefore

$$|F_2| = \frac{M}{59.8} \left[k \theta \frac{d^2\theta}{dt^2} \right]. \quad (5-19)$$

The pressure surge developed by this force is $\Delta p = \frac{|F_2|}{A_p}$ where A_p is the piston area of the servoactuator which is 57 in^2 . For a maximum linear acceleration of 12 g's^4 and an engine mass of $\frac{21 \times 10^3}{g} \frac{1 \text{ lb}}{\text{in/sec}^2}$,

Equation (5-19) results in $|F_2| = 6500.0 \text{ lbs}$ and

$$\Delta p = \frac{6500 \cdot \theta}{57 \text{ in}^2} = 114 \cdot \theta \text{ lb/in}^2. \quad (5-20)$$

Since θ is less than .1 radians ($< 5^\circ$) which is the maximum angular displacement about the gimbal point from the neutral position, there does not appear to be any danger of a high pressure surge being developed through the mechanical link.

APPENDIX A

SIMULATION OF FLAPPER VALVE AND METERING SPOOLS

The flapper valve portion of the actuator assembly shown in Figure 3.4 is shown in Figure 6.1 with appropriate symbols.

The operation of the flapper may be analyzed¹⁸ by considering first the force caused by the flow from the left nozzle. This force is the sum of the pressure force and momentum force and is

$$F_1 = A_\alpha P_\alpha + Q_F \rho V_\alpha \quad (6.1)$$

The flow through the left nozzle is

$$Q_F = A_F V_F = A_\alpha V_\alpha = C_d A_\beta \sqrt{\frac{2}{\rho} (P_F - P_{ls})} \quad (6.2)$$

Energy relations known as Bernoulli's equations are

$$\frac{P_F}{\rho} + \frac{V_F^2}{2} = \frac{P_\alpha}{\rho} + \frac{V_\alpha^2}{2} = \frac{P_{ls}}{\rho} + \frac{V_\beta^2}{2} \quad (6.3)$$

By combining Equations (6.1) through (6.3) an expression for the flow force on the left side of the flapper in terms of pressures is obtained as

$$F_1 = A_\alpha P_F + \frac{C_d^2 A_\beta^2}{A_\alpha} \left(1 + \frac{A_\alpha^2}{A_F^2}\right) (P_F - P_{ls}) \quad (6.4)$$

Since $A_F \gg A_\alpha$ in general, Equation (6.4) may be simplified to

$$F_1 = A_\alpha P_F + \frac{C_d^2 A_\beta^2}{A_\alpha} (P_F - P_{ls}) \quad (6.5)$$

For a nozzle having a circular orifice of radius r , the areas will be (for small displacements of the flapper)

$$A_\alpha = \pi r^2 \quad A_\beta = 2\pi r x = 2\pi r (x_o - \theta_F L_F) \quad (6.6)$$

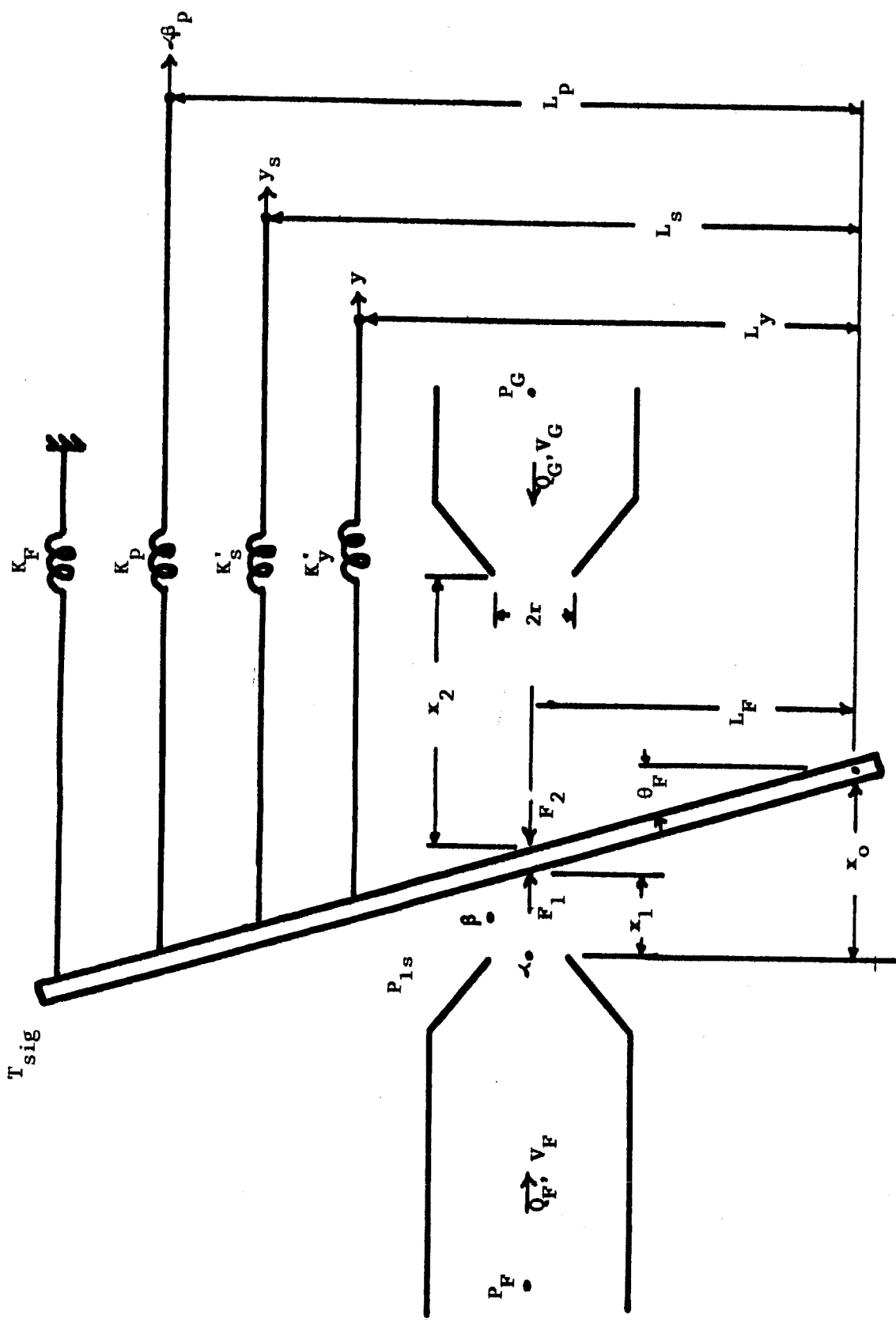


Figure 6.1 - Detail of Flapper Valve

Combining Equation (6.5) and Equation Set (6.6) gives

$$F_1 = \pi r^2 p_F + 4\pi C_d^2 (x_o - \theta_F L_F)^2 (p_F - p_{ls}) \quad (6.7)$$

In a simular manner the flow force on the right side of the flapper valve is

$$F_2 = \pi r^2 p_G + 4\pi C_d^2 (x_o + \theta_F L_F)^2 (p_G - p_{ls}) \quad (6.8)$$

The total flow force on the flapper is

$$\begin{aligned} F_{TF} = F_1 - F_2 &= (\pi r^2 + 4\pi C_d^2 x_o^2 + \theta_F^2 L_F^2) (p_F - p_G) \\ &\quad - 8\pi C_d^2 x_o \theta_F L_F (p_F + p_G) \\ &\quad - 16\pi C_d^2 x_o \theta_F L_F p_{ls} \end{aligned} \quad (6.9)$$

Summation of the torques acting on the flapper is given in Equation (6.10) for small angular displacements of the flapper

$$\begin{aligned} T_{sig} &= F_{TF} L_F + L_p K_p (-\beta_p + \theta_F L_p) + L_s K'_s (y_s + \theta_F L_s) \\ &\quad + L_y K'_y (y + \theta_F L_y) + K_F \theta_F \end{aligned} \quad (6.10)$$

Combining Equations (6.9) and (6.10) and rearranging gives

$$\begin{aligned} -\frac{\theta_F}{B_F} &= \pi L_F (1 + 4C_d^2 x_o^2) (p_F - p_G) - 8\pi L_F^2 C_d^2 x_o \theta_F (p_F + p_G - 2 p_{ls}) \\ &\quad - T_{sig} + L_p K_p \beta_p + L_s K'_s y_s + L_y K'_y y \end{aligned} \quad (6.11)$$

Where

$$B_F = \frac{1}{L_p^2 K_p^2 + L_s^2 K'_s^2 + L_y^2 K'_y^2 + K_F^2}$$

The flow equations for the various orifices supplying the flapper valve and first stage metering spool are

$$Q_3 = K_3 A_3 \sqrt{p_F - p_3} = K_3 A_3 \sqrt{p_4 - p_G} \quad (6.12)$$

$$Q_3 + Q_F = K_4 A_4 \sqrt{p_{hs} - p_F} \quad (6.13)$$

$$Q_G - Q_3 = K_4 A_4 \sqrt{p_{hs} - p_G} \quad (6.14)$$

$$Q_E = K'_E y_E \sqrt{p_{1E} - p_{ls}} = K'_E y_E \sqrt{p_{hs} - p_{hE}} \quad \text{for } y_E > 0 \quad (6.15a)$$

$$Q_E = K'_E y_E \sqrt{P_{hE} - P_{1s}} = K'_E y_E \sqrt{P_{hs} - P_{1E}} \quad \text{for } y_E < 0 \quad (6.15b)$$

The velocities of the metering spools are

$$\dot{y}_E = \frac{Q_3}{A_E} \quad (6.16)$$

$$\dot{y} = \frac{Q_E}{A_y} \quad (6.17)$$

The equation of motion of the first stage metering spool is

$$M_E \ddot{y}_E + R_E \dot{y}_E + K_E y_E = (P_3 - P_4) A_E \quad (6.18)$$

Substitution of Equation (6.16) into Equation (6.12) gives

$$P_3 - P_4 = P_F - P_G - \frac{2}{K_3} \dot{y}_E \quad (6.19)$$

Substitution of Equation (6.19) into Equation (6.18) and solving for

\ddot{y}_E gives

$$\ddot{y}_E = -\frac{R_E}{M_E} \dot{y}_E - \frac{K_E}{M_E} y_E + \left(\frac{P_F - P_G}{M_E}\right) A_E - \frac{2}{M_E} \left(\frac{A_E}{K_3 A_3}\right)^2 (\dot{y}_E)^2 \quad (6.20)$$

Substitution of Equation (6.16) into Equations (6.13) and (6.14)

yields

$$P_F = P_{hs} - \left(\frac{A_E \dot{y}_E + Q_F}{K_4 A_4}\right)^2 \quad (6.21)$$

$$P_G = P_{hs} - \left(\frac{Q_G - A_E \dot{y}_E}{K_4 A_4}\right)^2 \quad (6.22)$$

Substitution of Equation (6.6) into (6.2) yields

$$Q_F = 2\pi r C_D (x_o - \theta_{FF}^L) \sqrt{\frac{2}{\rho}} \sqrt{P_F - P_{1s}} \quad (6.23)$$

In a similar manner the flow through the right nozzle is

$$Q_G = 2\pi r C_d (x_o + \theta_{FF}^L) \sqrt{\frac{2}{\rho}} \sqrt{(P_G - P_{1s})} \quad (6.24)$$

The equation of motion of the second stage metering spool is

$$M_y \ddot{y} + R_y \dot{y} + K_y y = (P_{hE} - P_{1E}) A_y \quad (6.25)$$

Combining Equations (6.15) and (6.17) gives

$$\begin{aligned} P_{hE} - P_{lE} &= P_{hs} - P_{ls} - 2 \left(\frac{A}{K' y_E} \right)^2 \quad \text{for } y_E > 0 \\ P_{hE} - P_{lE} &= -P_{hs} + P_{ls} + 2 \left(\frac{A}{K' y_E} \right)^2 \quad \text{for } y_E < 0 \end{aligned} \quad (6.26)$$

The unscaled simulation corresponding to Equations (6.7), (6.11), (6.20), (6.21), (6.22), (6.23), (6.24), (6.25), and (6.26) is given in Figures 6.2 and 6.3.

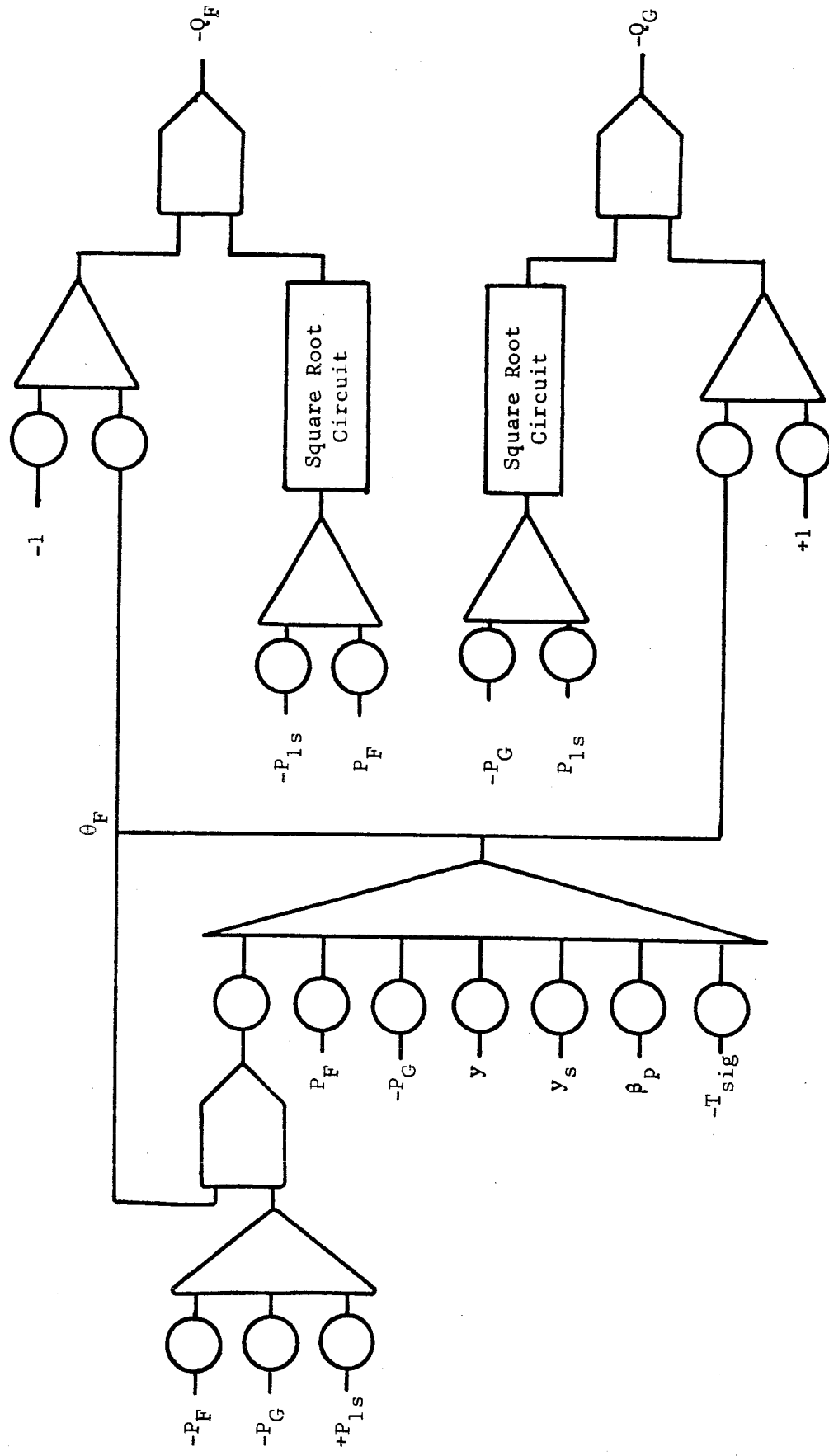


Figure 6.2 - Simulation of Nozzle Flow

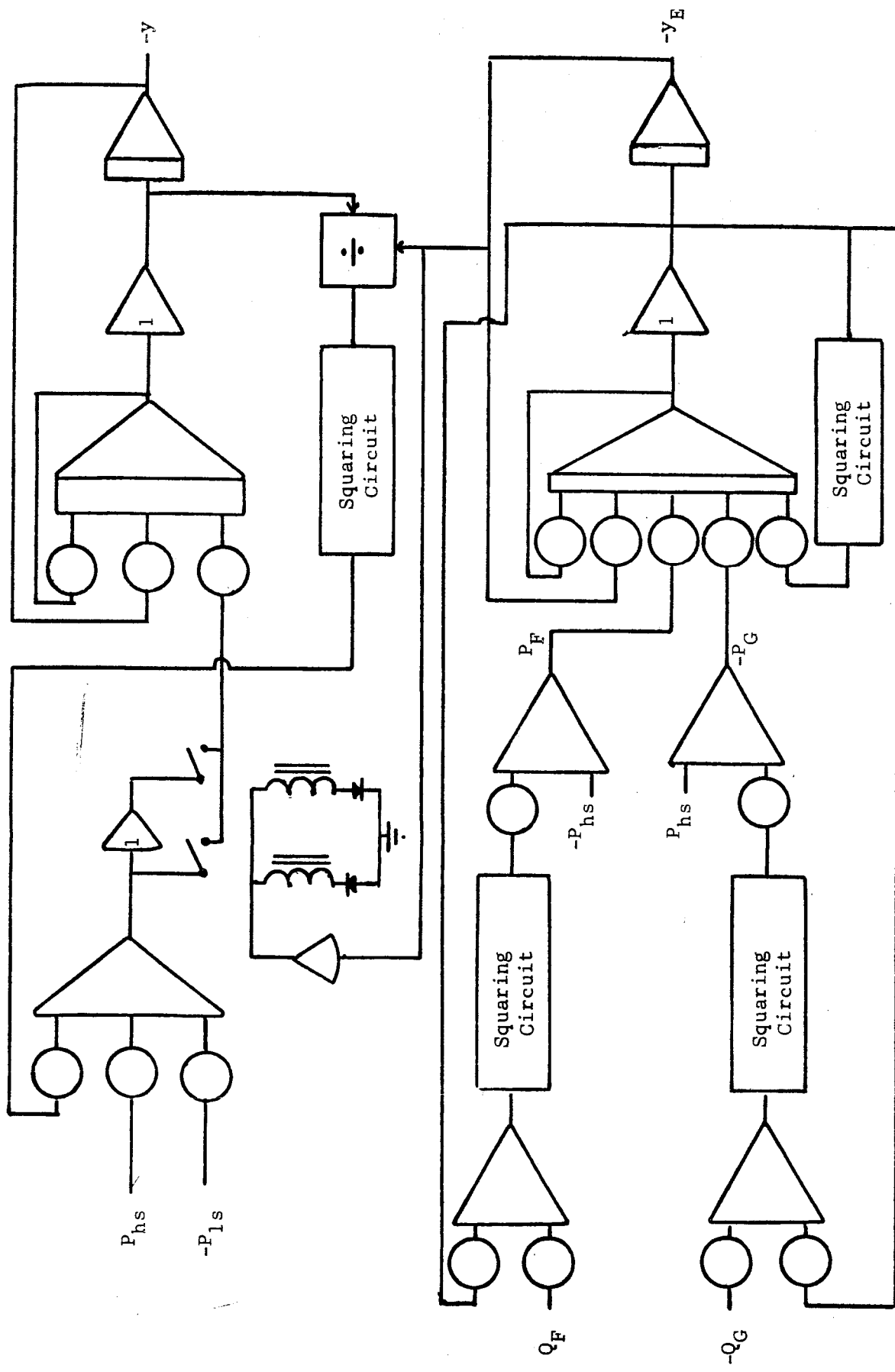


Figure 6.3 - Simulation of Metering Spool Position

REFERENCES

1. Daniels, C. M., "Pressure Losses in Flexible Metal Tubing," Product Engineering, Vol. 27, No. 4, April, 1956, pp. 223-227.
2. Daniels, C. M. and R. E. Fenton, "Determining Pressure Drop in Flexible Metal Hose," Machine Design, October 13, 1960, pp. 195-198.
3. Daniels, C. M., "Designing for Duct Flexibility with Bellows Joints," Machine Design, October 15, 1959, pp. 146-155.
4. Clark, R. A., "On Theory of Thin Elastic Toroidal Shells," Journal of Mathematics and Physics, MIT, Vol. 29, 1950, pp. 146-178.
5. Donnell, L. H., "The Flexibility of Corrugated Pipes Under Longitudinal Forces and Bending," Translation of the ASME, Vol. 54, 1932.
6. Turner, C. E. and H. Ford, "Stresses and Deflection Studies of Pipe-line Expansion Bellows," Institute of Mechanical Engineers Proceedings, (England), 171 No. 15, 1957, pp. 526-552.
7. "Production of High-Strength Bellows," Metal Industry, Vol. 97, No. 21, November 18, 1960, pp. 423-424.
8. Hannah, M. J., "Installing Bellows Expansion Joints? Here Are Important Points to Remember," Heating, Piping, and Air Conditioning, Vol. 34, January, 1962, pp. 186-191.
9. Matheny, James D., "Bellows Spring Rate for Seven Typical Convolution Shapes," Machine Design, Vol. 34, January 4, 1962, pp. 137-139.
10. Osteen, Dennis, Summary Report, Contract NAS8-11341, June, 1965.
11. Osteen, Dennis, Quarterly Report No. 5 - Contract NAS8-11341, October, 1965.
12. Knox, Lewis A., "Analysis of the Non-Linear Hydraulic Servoactuator for Saturn V, Stage S-IC," Memorandum R-ASTR-NFM-162-65, George C. Marshall Space Flight Center, Huntsville, Alabama, May 24, 1965.
13. Osteen, Dennis, Quarterly Report No. 6 - Contract NAS8-11341, October, 1965.
14. Osteen, Dennis, Quarterly Report No. 7 - Contract NAS8-11341, June, 1966.
15. Dimensions used are from Figure 2-15A, Center of Gravity and Inertia Data, Report R-3896-1, June 8, 1964.
16. Dimensions used for the actuator tie-points are from Brown Engineering Drawing of "F-1 Engine Simulator Stand," June 27, 1965.

17. Beer, F. P. and E. R. Johnson, Jr., Vector Mechanics for Engineers: Statics and Dynamics, McGraw-Hill Book Company, 1962.
18. Morse, Allen C., Electro-Hydraulic Servomechanisms, McGraw-Hill, 1963, pp. 25-37.